Microstructural degradation of Ni-YSZ anodes for solid oxide fuel cells

Thydén, Karl Tor Sune

Publication date:
2008

Document Version
Publisher's PDF, also known as Version of record

Risø DTU
National Laboratory
for Sustainable Energy

DTU

Risø-PhD-thesis

Microstructural Degradation of Ni-YSZ Anodes for Solid Oxide Fuel Cells

Karl Thydén

Risø-PhD-32(EN)

Risø National Laboratory for Sustainable Energy
Technical University of Denmark
Roskilde, Denmark
March 2008

DTU

Author: Karl Thydén
Title: Microstructural Degradation of Ni-YSZ Anodes for Solid Oxide Fuel Cells
Department: Fuel Cells and Solid State Chemistry Department

This thesis is submitted in partial fulfilment of the requirements for the Ph.D. degree at University of Copenhagen, H.C. Ørsted Institute

Abstract (max. 2000 char.):
Ni-YSZ cermets have been used as anode materials in SOFCs for more than 20 years. Despite this fact, the major cause of degradation within the Ni-YSZ anode, namely Ni sintering / coarsening, is still not fully understood. Even if microstructural
studies of anodes in tested cells are of technological relevance, it is difficult to identify the effect from isolated parameters such as temperature, fuel gas composition and polarization. Model studies of high temperature aged Ni-YSZ cermets are generally performed in atmospheres containing relatively low concentrations of H2O.
In this work, the microstructural degradation in both electrochemically longterm tested cells and high-temperature aged model materials are studied. Since Ni particle sintering / coarsening is attributed to be the major cause of anode degradation, this subject attains the primary focus. A large part of the work is focused on
improving microstructural techniques and shows that the application of low acceleration voltages (≤ 1 kV) in a FE-SEM makes it possible to obtain two useful types of contrast between the phases in Ni-YSZ composites. By changing between the ordinary lateral SE detector and the inlens detector, using similar microscope settings, two very different sample characteristics are probed:
1) The difference in secondary emission coefficient, δ, between the percolating and non-percolating Ni is maximized in the low-voltage range due to a high δ for the former and the suppression of δ by a
positive charge for the latter. This difference yields a contrast between the two phases which is picked up by an inlens secondary electron detector.
2) The difference in backscatter coefficient, η, between Ni and YSZ is shown to increase with decreasing voltage. The contrast is illustrated in images collected by the normal secondary detector since parts of the secondary signals are generated by backscattered electrons.
High temperature aging experiments of model Ni-YSZ anode cermets show that Ni sintering / coarsening is significantly increased, not only at higher temperatures, but also when the concentration of H2O in the reducing atmosphere is increased. It is proposed that the mobility of Ni is facilitated by the formation of Ni-OH complexes which are capable of segregating on the Ni particles surface, on the YSZ surface and via gas phase. This is a mechanism which has previously been reported in the context of Ni steam-reforming catalysis.
In the context of electrochemically tested and technologically relevant cells, the majority of the microstructural work is performed on a cell tested at 850°C under relatively severe conditions for 17,500 hours. It is demonstrated that the major Ni rearrangements take place at the interface between anode and electrolyte. It is also
shown that the degree of Ni sintering is dependent on the position along the fuel gas flow. The sintering is found to be most severe close to the fuel gas outlet. This difference in Ni sintering along the fuel gas flow is attributed to the increasing concentration of H2O at high fuel utilizations.
Two-dimensional microstructural analyses of the anode from the cell tested for 17,500 hours indicate a general increase of the Ni volume-fraction close to the electrolyte interface. From three-dimensional reconstructions using FIB-SEM it can be concluded that Ni must have segregated from the outer parts of the anode in order to yield the measured Ni content close to the electrolyte. It is also concluded that the Ni segregation has taken place on the length scale of several micrometers in the anode of this long-term tested cell.

Risø-PhD-32(EN)
March 2008

ISBN 978-87-550-3625-3

Contract no.:

Group's own reg. no.:

Sponsorship:

Cover :

Pages: 112
Tables:
References:

Information Service Department
Risø National Laboratory for Sustainable Energy
Technical University of Denmark
P.O.Box 49
DK-4000 Roskilde
Denmark
Telephone +45 46774004
bibl@risoe.dk
Fax +45 46774013
www.risoe.dtu.dk

NIELS BOHR INSTITUTE
FACULTY OF SCIENCE
UNIVERSITY OF COPENHAGEN

Microstructural Degradation of Ni-YSZ Anodes for Solid Oxide Fuel Cells

Karl Thydén

Ph.D. thesis which was publicly defended on Thursday 13 March, 2008, at 1.15 p.m. in lecture hall 4, at the H.C. Ørsted Institute, University of Copenhagen, for the degree of Doctor of Philosophy (Ph.D.) in Engineering.
External opponents: Prof. Detlev Stöver, Forschungsdirektor im Forschungsbereich Energie (EN), Jülich, Germany and Dr. Charlotte C. Appel, Haldor Tosøe A/S.
Chairman: Prof. Robert Feidenhans'l, Niels Bohr Institute, University of Copenhagen.

Risø-PhD-32(EN)
ISBN 978-87-550-3625-3

Fuel Cells and Solid State Chemistry Department
Risø National Laboratory for Sustainable Energy
Technical University of Denmark
DK-4000 Roskilde
Denmark
http://www.risoe.dtu.dk

and

Niels Bohr Institute
Faculty of Science
University of Copenhagen

Cover: 3D-reconstruction of nickel (Ni)- yttria-stabilized zirconia (YSZ) anode cermets, where the grey color represent metallic nickel, blue represent pores while YSZ is transparent. Top: non-tested anode. Bottom: anode tested under relatively severe condition for a period of 17,500 hours.

Preface

This thesis is submitted to the University of Copenhagen as a partial fulfillment of the requirements for the degree of Ph.D. The thesis at hand is the product of three years of work performed mainly at the Fuel Cells and Solid State Chemistry Department, Risø National Laboratory. Chapter 6 of this thesis is based on work performed during a five week visit to the Department of Materials Science and Engineering and the Major Analytical Instrumentation Center, University of Florida. The Ph.D. project was financed by Eltra-PSO, project no. 5302 and 5849. The formal responsibility of this work was undertaken by the Niels Bohr Institute, University of Copenhagen.

I would like to acknowledge my supervisors:
-Senior scientist Yi-lin Liu, Fuel Cells and Solid State Chemistry Department, Risø National Laboratory, for advice, many fruitful discussions and daily supervision.
-Associate Professor Erik Johnson, the Niels Bohr Institute, University of Copenhagen, for advice and guidance during the project.
-Research Engineer Rasmus Barfod, Topsøe Fuel Cell A/S, for advice, suggestions and fruitful discussions.

I gratefully acknowledge the many colleagues in the Fuel Cell and Solid State Chemistry Department and the Materials Research Department, for discussions, helpfulness and assistance during this Ph.D. project. Also, Professor Eric Wachsman and graduate student Danijel Gostovic, the Department of Materials Science and Engineering, University of Florida, for making the FIB-SEM work possible to perform, the hospitality and the great time in Gainesville.

Last but not least, I would like to thank Kristina, min skat, for her love, patience and support. She also helped me correct the worst grammar mistakes and gave useful suggestions for improvement of the manuscript.

Karl Thydén
Roskilde, Denmark, November 2007

Abstract

Ni-YSZ cermets have been used as anode materials in SOFCs for more than 20 years. Despite this fact, the major cause of degradation within the Ni-YSZ anode, namely Ni sintering / coarsening, is still not fully understood. Even if microstructural studies of anodes in tested cells are of technological relevance, it is difficult to identify the effect from isolated parameters such as temperature, fuel gas composition and polarization. Model studies of high temperature aged Ni-YSZ cermets are generally performed in atmospheres containing relatively low concentrations of H_2O.

In this work, the microstructural degradation in both electrochemically long-term tested cells and high-temperature aged model materials are studied. Since Ni particle sintering / coarsening is attributed to be the major cause of anode degradation, this subject attains the primary focus. A large part of the work is focused on improving microstructural techniques and shows that the application of low acceleration voltages ($\leq$ 1 kV) in a FE-SEM makes it possible to obtain two useful types of contrast between the phases in Ni-YSZ composites. By changing between the ordinary lateral SE detector and the inlens detector, using similar microscope settings, two very different sample characteristics are probed: 1) The difference in secondary emission coefficient, δ, between the percolating and non-percolating Ni is maximized in the low-voltage range due to a high δ for the former and the suppression of δ by a positive charge for the latter. This difference yields a contrast between the two phases which is picked up by an inlens secondary electron detector. 2) The difference in backscatter coefficient, η, between Ni and YSZ is shown to increase with decreasing voltage. The contrast is illustrated in images collected by the normal secondary detector since parts of the secondary signals are generated by backscattered electrons.

High temperature aging experiments of model Ni-YSZ anode cermets show that Ni sintering / coarsening is significantly increased, not only at higher temperatures, but also when the concentration of H_2O in the reducing atmosphere is increased. It is proposed that the mobility of Ni is facilitated by the formation of Ni-OH complexes which are capable of segregating on the Ni particles surface, on the YSZ surface and via gas phase. This is a mechanism which has previously been reported in the context of Ni steam-reforming catalysis.

In the context of electrochemically tested and technologically relevant cells, the majority of the microstructural work is performed on a cell tested at 850°C under

relatively severe conditions for 17,500 hours. It is demonstrated that the major Ni rearrangements take place at the interface between anode and electrolyte. It is also shown that the degree of Ni sintering is dependent on the position along the fuel gas flow. The sintering is found to be most severe close to the fuel gas outlet. This difference in Ni sintering along the fuel gas flow is attributed to the increasing concentration of H_2O at high fuel utilizations.

Two-dimensional microstructural analyses of the anode from the cell tested for 17,500 hours indicate a general increase of the Ni volume-fraction close to the electrolyte interface. From three-dimensional reconstructions using FIB-SEM it can be concluded that Ni must have segregated from the outer parts of the anode in order to yield the measured Ni content close to the electrolyte. It is also concluded that the Ni segregation has taken place on the length scale of several micrometers in the anode of this long-term tested cell.

Contents

1 Introduction

The principal idea of a fuel cell has been known since the first half of the nineteenth century. In 1839, Sir William Robert Grove, British judge and scientist, conducted experiments where he used electricity to split water into hydrogen and oxygen. He got the idea that it should be possible to reverse this reaction and instead extract electricity from hydrogen and oxygen. The name "fuel cell" appeared in the late nineteenth century when the first attempts to build practical devices using this principle were made. Since then, the internal combustion machine and the use of fossil fuels has reached a wide spread on the market, leaving only niche markets such as e.g. space shuttle applications for the fuel cell technology.

In the late twentieth century, the interest in fuel cell technology as an application for a wider market started to increase. The increased interest and investments in research for fuel cells goes hand in hand with the search for alternative energy production aiming to replace fossil fuels. Fuel cells have a relatively high efficiency for converting chemical energy, from a variety of possible fuel gases, directly to electrical energy. Today, there is a number of different types of fuel cell solutions, each suitable for different technological applications. The one of interest in this thesis is the solid oxide fuel cell (SOFC).

1.1 The Solid Oxide Fuel Cell

A solid oxide fuel cell consists of three layers of functional materials. The three layers are the anode, the electrolyte and the cathode (see Figure 1-1). The anode is defined as the electrode where the oxidation reaction takes place and the cathode as the electrode where the reduction reaction takes place. The cathode is fed with air or oxygen while the anode is fed with fuel gas (e.g. hydrogen or natural gas).Thus, the function of the cathode and the anode respectively is to provide environments where oxygen gas is readily reduced and fuel gas is readily oxidized. At the cathode, where electrons are supplied via the external electrical circuit, oxygen molecules are reduced to oxygen ions. The oxygen ions are conducted through the electrolyte to the anode. At the anode, oxygen ions oxidize the fuel gas and forms water and carbon dioxide, while the resulting free electrons are transported via the external circuit back to the cathode. The separation of the reduction and oxidation reactions, by the solid oxide

electrolyte, facilitates external utilization of the electrons involved in the total cell reaction and, consequently, direct conversion of chemical energy to electrical energy.

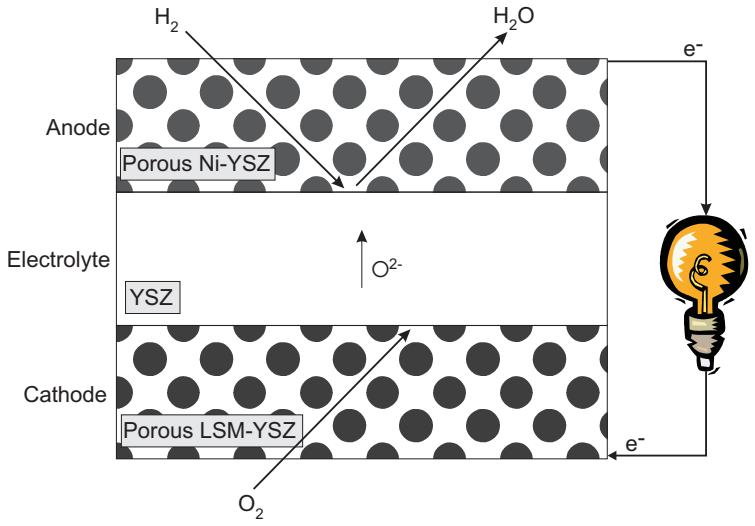

Figure 1-1. Schematic illustration of the cross section and the principal of operation for the solid oxide fuel. The separation of reduction and oxidation reactions facilitates external utilization of the electrons involved in the total redox reaction (chemical energy → electrical energy).

One cell produces a potential of approximately 1 V when no current is extracted from it. In order to achieve a higher voltage, cells are coupled in series. For the planar SOFC this is done by stacking cells, with a gas tight and electrically conducting interconnect plate between each cell.

1.2 The fuel cell components

A fuel cell must be mechanically and chemically stable from room temperature and up to the operational temperature (700-1000°C). Hence, the fuel cell components must have similar thermal expansion coefficients. Below, a short description of the state-of-the-art materials used in the key components of a solid oxide fuel cell is given. In addition to these functional materials, it should be kept in mind that many other components are also crucial in order to have a fully functional SOFC power-generator system. [1]

1.2.1 Electrolyte

The solid oxide electrolyte separates two different gas environments (fuel and air) and should be selectively permeable for oxygen ions (O^{2-}). The performance of the electrolyte is largely defined by how well it conducts the oxygen ions at operational conditions for the cell. The higher the ion conductivity is and the thinner

the electrolyte is, the lower the ohmic resistance over the cell will be. The thickness of the electrolyte in a state-of-the-art fuel cell depends on whether the electrolyte should provide mechanical strength to the cell or not. In an electrolyte supported cell, the electrolyte thickness is 150-250 μm. If the mechanical strength instead is provided by the anode, as in an anode supported cell, the electrolyte thickness can be reduced by a factor of ten.

ZrO_2 doped with Y_2O_3 has relatively high oxygen ion conductivity at temperatures >700°C, due to the introduced oxygen vacancies. The maximum conductivity for yttria-stabilized zirconia (YSZ) has been found to be at an yttria content of 8 mol% (8YSZ). Furthermore, 8YSZ is stable at high temperatures in both oxidizing (cathode) and reducing (anode) atmospheres. In this context it can also be mentioned that YSZ is an important ceramic in modern technology with a wide range of industrial applications such as metal coatings, refractory material, abrasives, catalyst support, and gas sensors. Especially 8YSZ is readily available for industrial applications.

1.2.2 Anode

The most commonly used anode material for SOFCs is a porous cermet (ceramic and metal) consisting of Ni and YSZ. Ni-YSZ anodes are processed and sintered as a NiO-YSZ composite with low porosity. NiO is then reduced to metallic Ni at high temperature prior to cell operation. Upon the reduction of NiO, the resulting volume decrease generates the desired porosity, which makes the anode permeable for fuel and exhaust gases. The electrochemical reactions take place at, or close to, the anode / electrolyte interface, which makes gas permeability an important parameter for the anode structure. The metallic Ni surface is catalytically active for adsorption and dissociation of hydrogen molecules. At the anode / electrolyte interface the dissociated hydrogen atoms readily react with oxygen ions transported through the electrolyte from the cathode, as shown in reaction **(1-1)**.

$$H_2 + O^{2-} \rightarrow H_2O + 2e^- \qquad \textbf{(1-1)}$$

The resulting electrons are transported, from the reaction site to the interconnect plates, through the Ni phase in the anode. It is therefore crucial that the

Ni phase is well percolated all the way from the anode / electrolyte interface through the anode to the interconnect plates.

The YSZ network acts as a backbone-structure and in an anode supported cell it provides mechanical strength to the whole cell. Another important function of the YSZ network is to stabilize the Ni phase and prevent it from coarsening [2]. The necessary adhesion between the anode and the electrolyte is accomplished when YSZ from the anode is sintered to the electrolyte YSZ. This connection also results in an extension of the electrolyte into the YSZ structure of the anode, and hence, the number of available reaction sites for the anode reaction is maximized. S. Primdahl et al. [3] have demonstrated that the extension of the reaction zone can reach several micrometers from the electrolyte interface into the anode structure.

Mixed ionic and electronic conducting oxides, such as gadolinium or samarium doped ceria, are also considered as potential anode materials. By use of mixed ion and electron conducting oxides it is possible to extend the reaction zone even further, due to a higher electronic conductivity in comparison to YSZ.

One important term used for describing both the anode and cathode reactions is the so-called triple phase boundary; TPB. The TPB describes a site in the electrode where reduction of oxygen or oxidation of fuel takes place. In the case of the anode, this site is where all three phases (Ni, YSZ and fuel gas) are in contact with each other. Since a supply of oxygen ions (YSZ), fuel gas (pore) and transport-way for the electrons (Ni) are simultaneously required, it is only at the TPB that the electrochemical reactions can take place. In order to optimize the electrode performance it is therefore important to maximize the number of available and active TPBs. It is also important to remember that in order for a TPB to be an active reaction site all three phases need to be percolating. This means that the pore must be connected to the gas stream, Ni must be connected to the interconnect plate, and the YSZ must be connected either directly to the electrolyte or via YSZ in the anode.

1.2.3 Cathode

At the cathode, oxygen is provided with electrons and reduced to oxygen ions in accordance with reaction **(1-2)**.

$$\tfrac{1}{2}O_2 + 2e^- \rightarrow O^{2-} \qquad \textbf{(1-2)}$$

Strontium doped lanthanum manganite (LSM) is electronically conducting and catalytically active for adsorption and dissociation of oxygen molecules. It has therefore proven to be a good choice as cathode material. The function of LSM is analogous to the function of Ni in the anode. As for the anode, an adhesion between the layers and extension of the reaction zone is attained by mixing LSM with YSZ. A variety of new promising cathode materials are also being developed, such as e.g. $La_{1-x-y}Sr_xFe_{1-z}Co_zO_3$ (LSFC) perovskites [4].

1.2.4 Interconnect plates

The interconnect plate should provide electronic contact between the anode of one cell to the cathode of the next cell as a number of cells are coupled in series in a cell stack. Just like the electrolyte, the interconnect plates separate an oxidizing cathode atmosphere and a reducing anode atmosphere at high temperature. Corrosion stable metal alloys, such as ferritic steels, provide chemical compatibility and mechanical strength at a low cost and are state-of-the-art for this application. However, in order to increase the chemical compatibility, the composition of the steel have to be tailored and often the steel plates need to be coated to prevent elemental segregation.

1.3 Cell performance

The cell voltage is an important parameter which describes the overall cell performance. The maximum voltage is dictated by the overall cell reaction and depends on the type of electrode gas and the reaction product(s) present. The maximum reversible cell-voltage, or electromotive force (EMF), is given by the Nernst equation for the specific system. Due to internal resistance, from e.g. transport resistance and concentration gradients, the cell-voltage will decrease as current is extracted from the cell. The difference between the operating cell-voltage (U) and the EMF is termed polarization (η). The total polarization over an operating cell can be divided into four types of polarization; charge transfer polarization (η_{ct}), diffusion polarization (η_{diff}), chemical reaction polarization (η_{chem}), and resistance polarization (η_{Ω}).

$$\eta = \eta_{ct} + \eta_{diff} + \eta_{chem} + \eta_{\Omega} \qquad \textbf{(1-3)}$$

Losses due to *charge transfer* are sometimes called activation losses and arise due to the threshold determined by the required activation energy for the reactions taking place in the cell. The reactions can be e.g. adsorption, electron transfer or desorption. The electrode reaction rate is a function of operating conditions and electrode materials and the activation energy can be altered by the presence of catalytically active materials.

Diffusion (or concentration) polarization is observed when the electrode reactions are not supplied with reactants, or drained from products, fast enough. A slow supply of reactants will alter the concentration at the reaction sites, thus slowing down the reaction. Chemical reaction polarization has the same effect as diffusion / concentration polarization, but is due to limiting reactions for producing or removing reactants or products. The diffusion loss and the chemical reaction loss are often collectively referred to as mass transport polarization (η_{mass}).

Resistance polarization is caused by the ohmic resistance towards transportation of ions and electrons through the electrolyte, electrode materials and the current collector arrangement. Resistance polarization is therefore commonly referred to as ohmic resistance or series resistance (R_S), and should be separated from the other polarization phenomena.

During operation of a fuel cell, polarization will inevitably be present. However, it can be minimized by material selection, cell design and operating conditions. By recording the cell-voltage at different current densities a so-called I-V curve can be constructed. This curve provides information on the overall cell performance at different current loads. A typical I-V curve is illustrated in Figure 1-2.

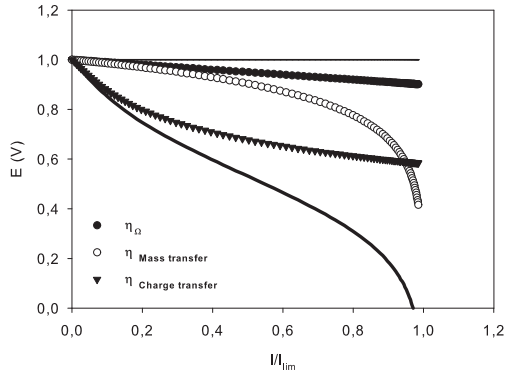

Figure 1-2. Schematic illustration of a typical I-V curve for a fuel cell (solid curve), including the contributions from individual internal resistances.

In this figure the characteristics of the contributions from the internal resistances defined above are also illustrated. [1]

When current is extracted from a cell, the resulting drop in voltage from the open circuit voltage (OCV) is defined as the cell polarization, or over-potential, at this specific current density. From the cell polarization and corresponding current density an *area specific cell resistance* can be defined as shown in equation **(1-4)**.

$$ASR = \frac{EMF - U}{i} \qquad \textbf{(1-4)}$$

Current extraction will also lead to consumption of fuel gas and a shift in fuel gas composition. If the fuel gas flow is not adjusted accordingly, or if a certain fuel-utilization is wanted during operation, this will lead to a change in the theoretically achievable EMF. In order to be able to compare ASR values independently of fuel gas composition, it is important to make corrections for the difference in fuel gas composition. For this purpose, an ASR_{cor} can be calculated. The background and procedure of these calculations are described in detail by M. Mogensen et al. [5].

1.4 Cell degradation

The function of the fuel cell is to facilitate the reactions and transportation of species mentioned above with the lowest possible resistance. The density of reactions sites (per cell area) and transport paths should hence be maximized during fabrication. The commercial requirements for SOFC systems include a cell and stack life time in the order of 40,000-50,000 hours. In order to facilitate such a long life time the, degradation rate must be very low in all components of the cell and stack. It is therefore important to increase the fundamental understanding of the degradation mechanism for each component in SOFCs. During operation, any change in the cell which causes blocked reaction sites or transport paths for species, will increase the overall cell resistance, and thereby the degradation. Especially changes in the electrode / electrolyte interfaces and grain boundaries are critical for the degradation of the fuel cell. These interfaces do not only provide the TPB but are also active for mass transportation, diffusion and segregation of species involved in the fuel cell reactions during operation. Microstructural changes in the interface regions, such as impurity segregation [6], will inevitably affect the cell performance.

The potential problems of cell degradation depend on at which conditions the cell is operated. The most obvious factor influencing degradation is the operating temperature, due to the generally increased atom mobility. Furthermore, A. Hagen et al. [7] have demonstrated that the overall degradation of the cell voltage over a full cell is more closely correlated to the polarization than to the current density. These findings were based on long-term tests of 1500 hours on cells relevant to this work. At high polarization, and especially at low temperatures, A. Hagen et al. report cathode degradation to be dominant. However, at lower polarizations and / or higher temperatures, the anode and cathode contribute more equally to the electrical degradation.

From cell tests it is difficult to assign any degradation mechanisms seen in electrical impedance measurements to a specific degradation mechanism. R. Barfod et al. [8] have studied the degradation of technologically relevant cells using electrical impedance spectroscopy. At 750°C and high polarization, it was concluded that cathode degradation dominated the overall degradation. However, the anode degraded by 80-120%. From impedance analysis, the degradation mechanism could not be determined, showing the importance of correlating electrical measurements and microstructural changes.

From impedance measurements on the Ni-YSZ anode, up to three separate responses have been reported [3]. At high frequency, a response that is proposed to be due to charge transfer between Ni and YSZ and the limiting reaction step at the TPB [3,9] is found. This response is seen to vary with operational temperature and is affected by thermal aging and microstructure of the anode. The other two responses arise at lower frequency and were not seen to be temperature dependant. The two latter responses have been assigned to gas diffusion and gas conversion, respectively [10,11], thus depending on the fuel / exhaust gas mixture surrounding the TPB.

1.4.1 Electrolyte degradation

Cubic zirconia stabilized with yttria (YSZ) is often used as electrolyte in SOFCs. 8 mol% Y_2O_3-92 mol% ZrO_2 (8YSZ) is found to have the highest ionic conductivity in the temperature interval of 850-1000°C. However, at 1000°C 8YSZ degrades more than e.g. 9.5YSZ and after only a few hundred hours the conductivity is well below that of 9.5YSZ. This degradation is shown to be due to precipitation and growth of tetragonal YSZ (t-YSZ) within the cubic YSZ (c-YSZ) [12,13]. Thus, 8

mol% yttria is not enough to fully stabilize the cubic phase at this temperature. The precipitation of t-YSZ is reported to accelerate in c-YSZ sintered in the presence of NiO, which dissolves into YSZ [14]. This is a potential problem at the electrolyte / anode interface since the anode most often is produced from NiO.

The degradation of conductivity for 8YSZ is greatly reduced as the temperature is decreased and below 800°C, 8YSZ and 9.5 YSZ have similar conductivity / degradation over the first 1000 hours [15]. Nevertheless, it can be concluded that a slightly higher concentration of Y_2O_3, or an alternative extra dopand, would be beneficial for the conductivity and phase stability of c-YSZ.

As NiO, also the presence of Mn affects the conductivity of YSZ. At 1000°C, a Mn content above 2 mol% is shown to have a stabilizing effect on 7.9YSZ, while a lower Mn content do not. At 850°C up to 5 mol% of Mn in 7.9YSZ is not found to stabilize the conductivity, but instead Mn addition is only detrimental for the overall conductivity [16]. This is a potential problem at the electrolyte / cathode interface since the cathode most often consists of Mn, which could dissolve into YSZ during sintering.

It has also been reported that during annealing of cubic stabilized Y_2O_3-ZrO_2, yttrium, silicon, sodium, iron and potassium are found to segregate to the external surface of single crystals [17,18]. This segregation is observed even at very low concentrations (< 100 ppm) of impurities [19]. Since these impurities are invariably present in YSZ and the manufacturing of the material generally involves calcination and sintering at elevated temperatures, it can not be avoided that impurities will segregate to the surface. The impurities do not only accumulate at the external surface, but also at the grain boundaries of polycrystalline YSZ [6]. These segregations affect electrochemical reactions in the SOFC and other applications [20] and makes it difficult to define the studied system in detail [21].

1.4.2 Anode degradation

The most often mentioned degradation problem within the Ni-YSZ anode is Ni particle sintering and coarsening [22,23]. The reason for the Ni coarsening is the relatively low sintering temperature of Ni in combination with the fact that Ni does not wet the YSZ surface. A coarsening of Ni results in a reduction of available TPBs and loss of electrical conductivity in the anode and the anode support. Temperature is the most important parameter, but also other operating conditions have been proven to

play an important role on the Ni coarsening. For technologically relevant operation a high current load and fuel utilization is needed. During such conditions of operation the anode will experience a concentration gradient along the fuel gas flow path. Assuming that the fuel gas is H_2, a high concentration of H_2 will be replaced by a high concentration of H_2O as the gas flows across the cell [24]. Because the reaction only takes place close to the interface, from where H_2O diffuses out through the anode support to the gas stream, a similar gradient is also expected to be present in the direction towards the anode / electrolyte interface.

A. Hagen et al. report that the anode degrades more at higher temperature [7]. In the same report they attribute the anode degradation to Ni coarsening at 750°C and 850°C, and also to Ni loss from local areas of the anode close to the electrode interface at 850°C. They mention Ni evaporation as one of the possible mechanisms for the Ni loss. The number of reports on this subject is limited, but Gubner et al. [25] see this phenomena at 950°C both in water / hydrogen (1:1) and especially methane / water (1:2) atmospheres.

As previously mentioned, impurities tend to segregate to the surface of YSZ. This segregation will inevitably affect the anode and the interface between Ni and YSZ. Several studies of the influence of impurities on the TPB of Ni-YSZ anodes have been reported [26-29]. The segregation of impurities to the Ni-YSZ interface is demonstrated to increase the polarization resistance for the anode reaction.

A slightly different, and more direct, degradation problem for the Ni-YSZ anode is the risk of re-oxidation, or what is called the redox behavior. If a Ni-YSZ anode is subjected to an oxidizing atmosphere at a high temperature, Ni will react to NiO, bringing about a significant volume expansion. Even if this is the state of the anode before the initial reduction, a rearrangement of Ni and NiO results in a great risk of mechanical failure of the YSZ structure [30,31]. It is therefore important to have a stable fuel gas supply and to minimize the risk of accidental gas leaks leading to oxidation of the anode.

1.4.3 Cathode and interconnect degradation

Ferrite stainless steels are often the preferred choice of material for the interconnect plates. At high temperatures and long-term operation, oxide layers are formed on the surface of the metallic interconnect, resulting in an increase of the electrical resistance between stacked cells. In addition, volatile Cr species are formed

over the oxide layer in oxidizing atmospheres. The Cr species can deposit at the interface between the cathode / electrolyte, causing a severe loss of cathode performance [32]. Evidence of surface diffusion of Cr species through the physical contact between interconnect and cathode, has also been presented [33].

Moreover, LSM and YSZ are found to react and form lanthanum zirconate (LZO) at the cathode / electrolyte interface. The presence of LZO increases the electrode resistance and can lead to cathode / electrolyte delamination [34]. The LZO formation is known to be dependent on operating conditions, sintering temperature and the composition of the LSM phase [35].

1.5 Objective of the thesis

The use of Ni-YSZ cermets as the anode material in SOFCs is not a recent invention. However, the major cause of degradation within the Ni-YSZ anode, namely Ni sintering and coarsening is still not fully understood. Even if microstructural studies of anodes in tested cells is of technological relevance, it is difficult to identify the effect from isolated parameters, such as temperature, fuel gas composition and polarization. Model studies of high temperature aged Ni-YSZ anode cermets are generally performed in atmospheres consisting of relatively low concentrations of H_2O.

The objective of this thesis is to gain a better understanding of the microstructural degradation mechanisms in the Ni-YSZ anode for SOFCs in general and as a function of different operation conditions. The microstructural changes in both model anode cermets and anodes from electrochemically long-term tested cells are studied. Since Ni particle coarsening and sintering is attributed as a major cause of anode degradation, this subject will also attain the primary focus. In order to study and characterize the microstructural rearrangements and degradations within the Ni-YSZ anode cermet, appropriate imaging and analysis techniques are needed. Another issue during this work is therefore to improve and develop the existing microscopic techniques in order to attain relevant microstructural information concerning the Ni-YSZ anode. The microstructural analysis is performed by a combination of optical microscopy, scanning electron microscopy (SEM), X-ray energy dispersive spectroscopy (X-EDS) and focused ion beam combined with SEM (FIB-SEM).

1.6 Thesis layout

In chapter 2 a general description is given concerning the experimental methods and techniques used throughout this work.

Chapter 3 presents the development and application of two useful low-voltage SEM techniques for characterization of Ni-YSZ cermets.

Chapter 4 presents a study of the effect of temperature, H_2O concentration in a reducing atmosphere of H_2 and current load, during high temperature aging of Ni-YSZ anode support materials.

Chapter 5 presents a microstructural study of the Ni-YSZ in a cell operated for 17,500 hours.

Chapter 6 presents the work to characterize the Ni-YSZ anode degradation in the long-term tested cell presented in chapter 5 by three-dimensional reconstruction.

In chapter 7, 8 and 9 an overall discussion, final conclusions and an outlook are presented, respectively.

2 Experimental methods and techniques

In this chapter, the main techniques utilized throughout this project are presented and described. A large part of the work has been devoted to perform high temperature aging treatments of Ni-yttria stabilized zirconia (YSZ) cermets, combined with in-situ conductivity measurements. Thereafter the microstructure of the cermets has been studied. In addition to the aged Ni-YSZ cermets that have experienced conditions without concentration gradients or polarization, the microstructures of tested cells have been studied by the same techniques. The Ni particle sizes in the samples have been determined and qualitative studies concerning general appearance have been performed. A long-term tested cell was selected for three-dimensional reconstruction based on images acquired by use of a focused ion beam-scanning electron microscopy (FIB-SEM).

With focus on microstructural characterization of Ni-YSZ cermets, the application of low-voltage SEM has been explored. By use of low voltage and different electron detectors, two microscopy techniques have been developed for this specific purpose. The first technique utilizes a form of charge contrast and is in the following referred to as SEM-CC. SEM-CC yields a clear distinction between percolating and non-percolating Ni within the cermet. The Ni phase that is percolating appears bright, while non-percolating Ni, YSZ and pores appear dark in the images. Thus, by this charge contrast the Ni particles that contribute to the electrical conductivity and to the active TPBs are readily visualized.

In the later part of the project, a second low-voltage technique was developed in order to overcome the lack of contrast between Ni and YSZ in SEM. Unfortunately, at this point it was not possible to redo the particle size analyses and results presented in this thesis are not based on the newly developed low-voltage SEM technique. The two low-voltage SEM techniques are presented in a separate chapter (Chapter 3), along with a theoretical background for the effective contrast mechanisms.

2.1 Heat treatment and in-situ conductivity measurements

The objective of this work is to study the effect of temperature, partial pressure of water and current load on changes in electrical conductivity and microstructure of Ni-YSZ cermets. In order to do this, samples of Ni-YSZ were treated under a variety of conditions with regard to temperature, atmosphere and current load. The electrical

conductivity is determined by the percolating Ni phase and may therefore give a good indication of Ni rearrangements within the materials. Based on this assumption, the conductivity of the material was continuously measured in-situ during the heat treatment. After the aging, microstructural analysis was performed and correlated to the acquired conductivity data. The experimental setup for these experiments is presented below, while sample preparations and the results are presented and discussed in Chapter 4.

2.1.1 Experimental set-up

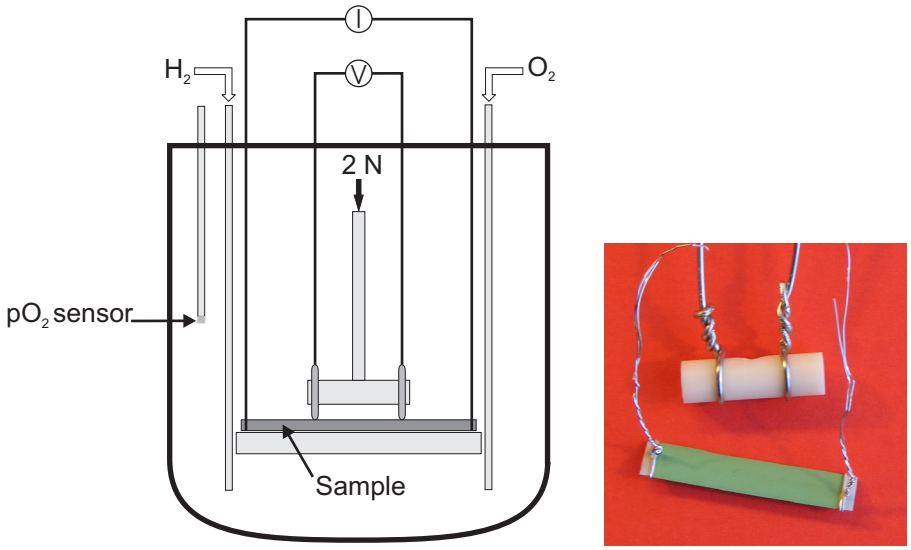

Figure 2-1. Schematic illustration of the furnace setup (left) and sample / probe mounting (right).

Two samples at a time were mounted in a vertical tube furnace, see Figure 2-1, and treated for 300 hours under various conditions. The parameters varied were: temperature (750 or 1000°C), H_2O / H_2 ratio in the aging atmosphere (3, 50 or 85% water), and electrical current load (no current load or 4.5 A / cm^2 constant current). After aging treatment, the Ni-YSZ samples were mounted into epoxy resin under vacuum, ground and polished for both optical microscopy (OM) and SEM. The reduced reference samples were prepared by the same procedure. The temperature was measured by an S-type thermocouple (Pt-Pt / Rh 10%) and the O_2 potential was measured over an yttria-stabilized zirconia sensor. Two gas inlets were connected to the furnace. The first gas inlet was used for air, 9% H_2 / Ar or 100% H_2. The second gas inlet was used to add O_2 to the H_2 atmosphere, and thereby produce the wanted pO_2. The gas supplies were fed to the bottom of the furnace, while the exit gas was lead out at the top.

Mixing H_2 and O_2 at a high temperature leads to the equilibrium reaction given in **(2-1)**.

$$H_{2(g)} + \frac{1}{2}O_2 \leftrightarrow H_2O_{(g)} \quad \textbf{(2-1)}$$

This equilibrium is highly shifted towards formation of H_2O and the concentration of H_2O is in principle controlled by the stoichiometrically limiting reactant. In order to obtain e.g. a 50 / 50 mixture of H_2O and H_2, the gas flows were set at a O_2 / H_2 ratio of 0.25. pO_2 for the wanted gas mixture was calculated at the relevant temperature by use of the expression for the equilibrium constant, *K*, given in **(2-2)** [36].

$$K = \frac{pH_2O_{(g)}}{pH_{2(g)} \cdot \sqrt{pO_{2(g)}}} = 10^{-\left(2.958 - \frac{13022}{T}\right)} \quad \textbf{(2-2)}$$

The EMF to be expected at this pO_2 was subsequently calculated by use of Nernst equation for an oxygen concentration cell.

$$EMF = \frac{R \cdot T}{4 \cdot F} \cdot \ln\left(\frac{pO_{2,reference}}{pO_{2,furnace}}\right) \quad \textbf{(2-3)}$$

In this equation, *R* is the gas constant, *T* is the temperature and *F* is Faradays constant. Air was used as reference gas, i.e. $pO_{2,reference}$=0.21 atm. The gas composition was adjusted manually by changing the O_2 flow to the furnace so that the correct EMF was read from the oxygen monitor. To achieve a H_2O concentration of 3%, the gases were moisturized in water at RT.

The electrical resistance of the samples was measured by 4-probe DC measurements during the treatment. Current was applied via Pt-probes connected to the sample, either continuously or only when measurements were performed. Pt-paste was used to ensure good contact to the edges of the sample. Voltage probes, separated by a distance of 10 mm, were pressed down on top of the sample stripes using a 200 g load. The current was generated by an external DC power supply (GW instek, GPS-3030DD). A Keithly 2700 multimeter (Keithly Instruments Inc., Cleveland, OH) was utilized to measure voltages and resistances continuously in intervals of 2-15 minutes.

This instrument has a resolution down to 100 μΩ and 0.1 μV in the relevant measurement ranges (~100 mΩ and ~10 mV). Offset-compensation was used in order to overcome possible thermal emfs.

The resistance (R) measured across the sample was converted to conductivity (σ) by equation **(2-4)** and degradation can be seen as a decrease in conductivity.

$$\sigma = \frac{l}{a \cdot b \cdot R_{measured}} \qquad \textbf{(2-4)}$$

Here l is the distance between the voltage probes, a is the sample width and b is the sample thickness. The contribution of conductivity from the dense YSZ is neglected and the sample thickness used in the calculations therefore excludes the thickness of the dense YSZ layers.

After treatment, the samples were subjects for microstructural analysis.

2.2 Cell testing

Microstructural analysis was also performed on electrochemically tested full cells after long-term operation. Results from theses microstructural analyses and the specific operating conditions during the cell tests are presented and discussed in Chapter 5. The SOFCs studied were anode-supported cells consisting of a Ni-YSZ anode, YSZ electrolyte and a lanthanum strontium manganite (LSM)-YSZ cathode. The overall cell dimensions were 5 cm × 5 cm with an active cell area of 4 cm × 4 cm.

The electrochemical tests were performed in alumina test-houses with gold and Ni foils as current collectors on the cathode and anode side respectively. LSM and Ni-YSZ gas distribution components were used on the cathode and anode side, respectively. Standard glass-ceramic composite seals were used to seal the cell. The test setup and method for testing full cells are described in detail by M. Mogensen et al. [5,37] while the cell fabrication is described elsewhere [38]. The cells were heated to 1000°C in air, where after the anode reduction procedure took place in two steps. In the first step the gas was changed from air to humidified diluted H_2 (9% in N_2, 4% H_2O) and in the second step, after two hours, the gas was changed to humidified H_2 for one hour.

After reduction of the anode, and before close down of the cell tests, AC and DC characteristics were obtained at 750°C and the operational temperature with air

and humidified H_2 as cathode and anode gases, respectively. The impedance spectra were acquired by use of a Solatron 1260 frequency response analyzer.

A mixture of CO_2 and H_2 (1:4) was used as fuel gas. At high temperatures, the two equilibrium reactions given in **(2-5)** and **(2-6)** will take place.

$$CO_2 + 4H_2 \leftrightarrow CO + H_2O + 3H_2 \quad \textbf{(2-5)}$$

$$CO + H_2O + 3H_2 \leftrightarrow CH_4 + 2H_2O \quad \textbf{(2-6)}$$

The two reactions given above correspond to the reverse of the reactions utilized in steam-reforming of CH_4 and the water-gas-shift reaction commercially used to produce H_2. A fuel gas with a CO_2 / H_2 ratio of 1:4 corresponds to pre-reformed methane with a steam / carbon ratio of 2. At equilibrium this results in a H_2O concentration of approximately 20% in the inlet fuel gas. During the cell tests, the fuel utilization was controlled by measuring the pO_2 of the gas outlet and the fuel utilization was set to 75-85%. Compressed air was used as cathode gas (pH_2O ~0.1 %).

The cells were tested and analyzed as part of a larger program, with the aim of identifying degradation mechanisms. The practical cell testing is outside the scope of the presented work. Data from the electrical measurements on tested cells have been analyzed in this work and is presented in Chapter 5. However, the practical cell testing was not a part of this Ph.D. project.

The anode microstructure of three tested cells and two references were analyzed. The cells had all been tested at an operation temperature of 850°C, with various current loads and operating times. In Table 2-1, the cell ID and current density are presented for the three cells. In addition, cells from the same production batches were reduced by the same procedure as the tested cells and used for microstructural reference.

Table 2-1. Presentation of the cells analyzed in this work, including the specific operating conditions.

Cell ID	Current density (A/cm^2)	Operation time (hours)
DK-34	1.00 (0.63)	17,500
PSC6953	0.25	1,500
PSC7069A	1.93	1,500

During cell testing, the performance of the cell is mainly characterized by the operating cell voltage. The cell is operated under constant current (galvanostatic mode). If the cell resistance changes over time, a different cell polarization will be needed in order to keep the constant current. Thus, a change in the operating cell voltage will reflect a change in the cell resistance. The area specific resistance (ASR) is determined from I-V curves recorded before and after the degradation test.

Electrical impedance spectroscopy is one of the most important techniques used for detailed evaluation of the electrical performance of cell components and full cells. By applying an alternating signal $v(t) = V_m \sin(\omega t)$, across the electrode or cell, a resulting current $i(t) = I_m \sin(\omega t + \theta)$ can be measured. θ is the phase difference between the voltage and current signals, and $\theta = 0$ for a purely resistive response. Analogous to Ohm's law, the impedance can be defined as $Z(\omega) = v(t)/i(t)$. The magnitude of the impedance is $|Z(\omega)| = V_m / I_m(\omega)$ and the phase angle is $\theta(\omega)$. By rearrangements of the expression above, the impedance can be expressed in complex form and rectangular coordinates in accordance to **(2-7)** and **(2-8).**

$$\mathrm{Re}(Z) = Z' = |Z|\cos(\theta) \qquad \textbf{(2-7)}$$

$$\mathrm{Im}(Z) = Z'' = |Z|\sin(\theta) \qquad \textbf{(2-8)}$$

Here, the phase angle, θ, is expressed in accordance to **(2-9)**.

$$\theta = \tan^{-1}(Z''/Z') \,. \qquad \textbf{(2-9)}$$

Impedance spectra are generally represented by either the Nyquist or the Bode plot. In the Nyquist, plot the imaginary part is plotted versus the real part of the impedance. In the Bode plot, the absolute impedance and the phase shift are plotted versus the angular frequency. [39]

At high frequency, the measured resistance consists mainly of a series resistance, R_s, which is caused by the ohmic resistance across the cell. In general, the dominating cause of R_s is the transport of oxygen ions in the electrolyte. At lower frequencies the polarization resistances becomes more dominant. Within the cell, different transport and transfer mechanisms have different relaxation times and can thereby sometimes be separated in an impedance spectrum. There are three overall

"mechanisms" that are crucial for the SOFC function; 1) transformation of $O_{2(g)}$ to O^{2-} at the cathode, 2) transport of the oxygen ions through the electrolyte from the cathode to the anode and 3) reduction of the fuel gas at the anode. All these overall "mechanisms" consists of a number of separate reaction steps with different rate constants, temperature and microstructural dependency, which to some degree still are not fully understood. Nevertheless, by a large number of systematic measurements on both single components and full cells, where parameters such as temperature, gas and composition, microstructure and material are varied, it has been shown possible to assign impedance responses to specific mechanisms that are important during cell operation [3,9-11,40,41].

2.3 Microstructural analysis

In order to study and characterize the microstructural rearrangements and degradation within a Ni-YSZ anode cermet, appropriate imaging and analysis techniques are needed. The Ni-YSZ anodes for SOFC are most often comprised of Ni and YSZ particles in the size range from sub-micrometers up to a few micrometers, which is also the case for samples studied in this work. From a random cross-section of this material it can therefore be expected that particle sections with a diameter in the nanometer range will be present. In order to be able to distinguish and image the smallest particles and features on this scale, a resolution of 10-100 nm is needed. With SEM, this resolution can be obtained and it is also the most commonly used tool for qualitative imaging of Ni-YSZ cermets.

In order to correlate the microstructure with the electrical performance it is often necessary to conduct full characterization of the microstructure of the three components; Ni, YSZ and pores. At ordinary acceleration voltages (10-20 kV) used for SEM, Ni and YSZ have very similar backscatter coefficients which results in a lack of contrast between the two phases in a SEM backscatter image [42-44]. In an SEM image it is possible to distinguish Ni from YSZ by eye, based on shape and surface features, and manual measurements can be readily performed in local areas. However, the lack of contrast makes it impossible to analyze and measure particle size and area fraction of the three components by use of image analysis software. In order to perform a statistically sufficient image analysis of a sample, a strong contrast between Ni and YSZ is necessary. One solution to this problem is to use optical microscopy (OM) where Ni, on a polished cross section, will appear very bright. In

order to achieve contrast between YSZ and pores it is required to sputter the surface with an interference film of Fe_2O_3 [43]. However, the utilization of OM for microstructural characterization of Ni-YSZ anodes is limited by its relatively low resolution. The Ni and YSZ particles are often in the sub-micrometer range, while the theoretical resolution of OM is ≥ 0.2 μm.

Another possibility is to use X-ray mapping. This technique results in a clear distinction between Ni and YSZ, but it is time-consuming and suffers not only from low spatial resolution but also from a low depth resolution.

In this work OM was used to perform statistical Ni particle size analysis. Due to the relatively low resolution, a fraction of the smallest Ni particle cross sections was lost in the analysis. Despite the compromise with regard to resolution it was demonstrated that optical imaging can give relevant microstructural information concerning Ni sintering. The YSZ structure is assumed to be stable during operating conditions and no quantitative measurements were performed on this phase. This assumption is verified in literature [43] and makes the optical images useful even without the possibility to distinguish YSZ from the pores.

In this project, work has been devoted to find a better technique for imaging Ni-YSZ cermets with higher resolution so that even the small particles can be detected and analyzed. The outcome of this work is presented in Chapter 3, where it is demonstrated how to achieve contrast between Ni and YSZ and between percolating Ni and non-percolating Ni (SEM-CC) by use of low-voltage SEM.

In the above description microscopy techniques are applied to a polished cross section, yielding two-dimensional information. In order to acquire three-dimensional information of anode microstructures FIB-SEM was used. This technique is presented in section 2.3.5.

In Table 2-2, below, an overview of the utilized microscopic techniques is given, along with the specific application and advantages / disadvantages. A description of the low-voltage SEM and SEM-CC techniques can be found in Chapter 3.

Table 2-2. Overview of the used microscopic techniques indicating specific characteristics.

Technique	Application	Remarks	Resolution
Optical microscopy	Ni phase	fast	low
Conventional SEM	all phases	no contrast for Ni-YSZ	high
Low-voltage SEM	all phases	FEG-SEM	high
SEM-CC	percolating Ni	FEG-SEM	high
EDS	chemical comp.		low
FIB-SEM	all phases and 3D	time consuming	high

2.3.1 Sample preparation

A major part of the performed microscopy and microstructural analyses were applied to polished sample cross sections. During polishing it is important to make sure that the sample structure is not altered due to artifacts introduced from the polishing. The samples consist of two materials with very different mechanical properties and at the same time the structure is porous. The polishing procedure was hence carefully evaluated and in order to reduce the effect from porosities the samples were cold mounted under vacuum into a low-viscous slow curing epoxy (Epofix from Struers A/S, Denmark). The mounting process was carried out in a vacuum impregnation apparatus (Epovac from Struers A/S, Denmark). The epoxy penetrates the porosities well and reduces the amount of residues present after the mechanical polishing. In addition, the epoxy reduces topographic effects during imaging in SEM and optical microscope.

The grinding and polishing procedures are outlined in Table 2-3.

Table 2-3. Grinding and polishing procedures for the polished cross-sections. Polishing cloths, abrasives and lubricants are commercially available from Struers A/S, Denmark.

	Grinding 1	Grinding 2	Grinding 3
Abrasive	320 SiC-paper	500 SiC-paper	1000 SiC-paper
Lubricant	Water	Water	Water
	Polishing 1	**Polishing 2**	**Polishing 3**
Surface	Dur cloth	Mol cloth	Mol cloth
Abrasive	6µm diamond suspension	3µm diamond suspension	1µm diamond suspension
Lubricant	DP-Blue	DP-Blue	DP-Blue

Between each polishing step the samples were cleaned in ethanol in order to remove residues from the previous step. In Figure 2-2 the final cross section of a sample is shown. The sample surface was coated with a conducting carbon layer for ordinary SEM, EDS and FIB-SEM while low-voltage SEM and optical microscopy were applied to non-coated sample surfaces.

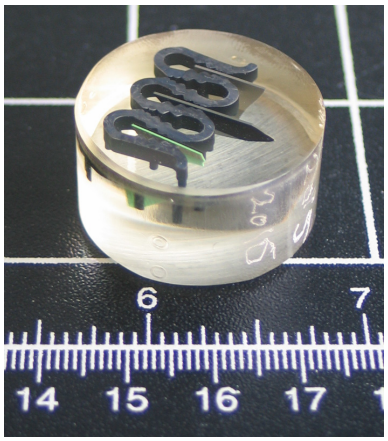

Figure 2-2. Polished cross sections of epoxy mounted cell samples.

2.3.2 Optical microscopy

In this work an Aristomet microscope (Leitz) and a DC 300 (Leica) digital camera were used. In an optical microscope the Ni phase reflects light and appears brighter than the YSZ and the pores (epoxy). From the optical images it is therefore possible to distinguish and analyze the size and shape of the Ni particles, see Figure 2-3a-b. The resolution of this technique is >0.2 μm.

2.3.3 Scanning electron microscopy

The microscope used in this work was a Zeiss Supra 35. This microscope is equipped with a field emission gun, GEMINI electron-optics, a lateral secondary electron (SE) detector (Everhart-Thornley), a backscatter detector, an inlens SE detector and a Noran System SIX X-ray microanalysis system.

The main characteristic of the GEMINI optics is the use of a beam booster and an objective lens which acts as a combined electrostatic / electromagnetic lens. The electrons generated at the gun tip are accelerated to the set acceleration voltage as they are accelerated towards the anode. However, the beam booster, which is installed directly after anode, is always at a potential of an extra 8 kV when the set acceleration voltage is ≤20 kV. When low voltages are used, this arrangement will ensure that the

energy of the electrons in the beam path will always be 8 kV higher than the set acceleration voltage and will reduce the influence of magnetic stray fields on the electron beam. Before the electron beam exits the objective lens, the electrostatic lens reduces the potential by an opposite applied 8 kV. The main advantage of this technique is that a stable beam is obtained even at low acceleration voltages.

In addition to acting as a retardant towards the electrons ejected from the electron column, the electrostatic lens will act as a collector for the electrons generated at the sample surface. The sample electrons are accelerated and focused back up the beam path, where the inlens SE detector is positioned (annular detector). The combination of the electrostatic lens and the inlens detector results in a very high detection efficiency for the inlens detector even at low acceleration voltages (< 1 kV). [45]

2.3.4 Two-dimensional image analysis

Digital images from optical microscopy and SEM images where percolating Ni appears bright (SEM-CC) were used to analyze the total amount of Ni particles and the percolated Ni particles, respectively. A clear contrast was obtained for Ni in both optical and SEM-CC image. The Ni particles were separated on basis of the grey scale by manual application of a threshold and the images were converted to binary colors. In Figure 2-3, below, typical OM and SEM-CC images and the corresponding binary images are shown. The binary images were analyzed using Image-Pro Plus (Media Cybernetics, USA).

Morphological filtering was applied to the binary images in order to eliminate any noise effect around the edges of the particle objects. The average diameter for each particle, measured from the cross section, was automatically measured at 2° intervals around the centroid of each particle by the software. Particle clusters were measured as one object. In addition, the area fraction of the Ni phase / percolating Ni phase was measured. All particles cut by the image boarders were excluded from the particle size measurements, but included for the area fraction measurements.

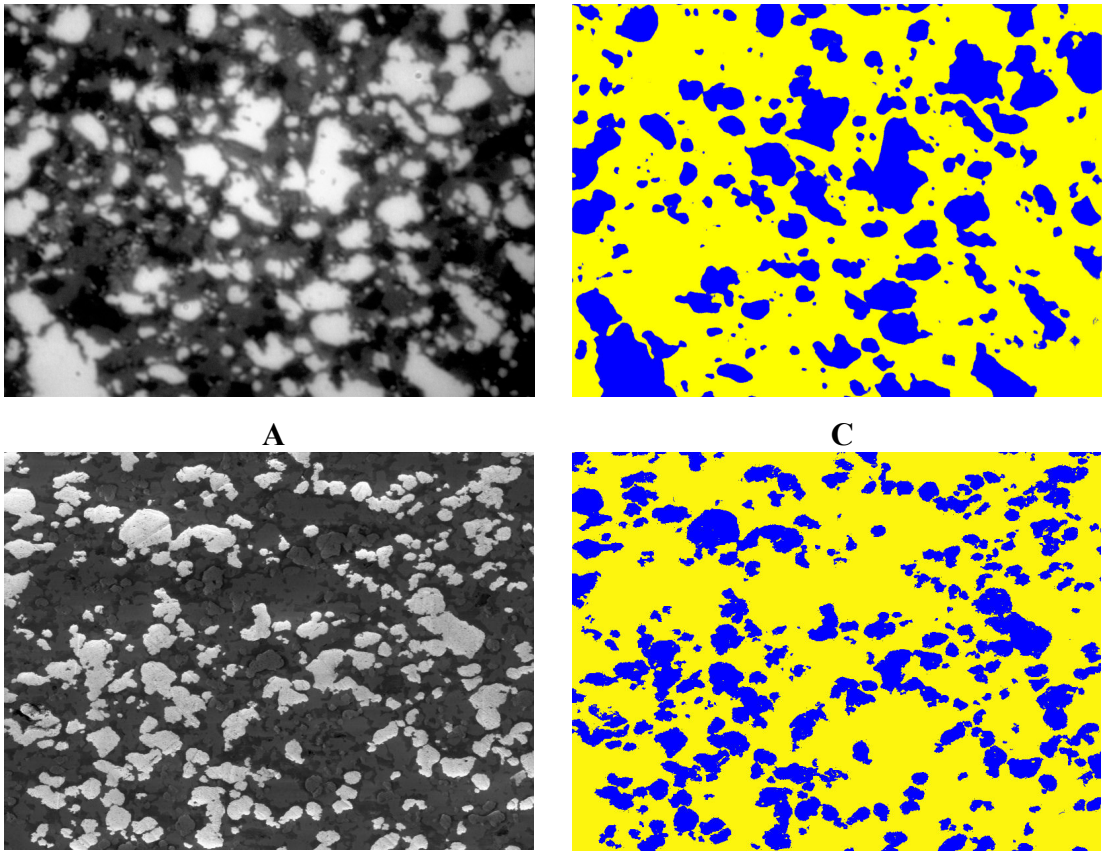

Figure 2-3a-d. Optical image where all the Ni particles appear bright (a), a charge contrast image where only the percolated Ni particles appear bright (b) and the corresponding binary images used for microstructural analysis (c-d).

It should be kept in mind that the measured diameter of each particle in a cross-section does not equal the absolute particle diameter. In order to estimate the absolute particle diameter it is necessary to make assumptions on not only the particle shape but also the particle size distribution. These assumptions require that the studied material to a great extent already is well defined with regard to particle shape and particle size distribution [46]. When the aim is to use quantitative microstructural data from two-dimensional imaging in electrochemical modeling of SOFC electrodes, this is a major drawback. J.R. Wilson et al. [47] expresses the general disadvantages of two-dimensional microstructural analysis in the following way;

"Current methods of microstructural analysis, such as SEM, only provide two-dimensional anecdotes of the microstructure, and thus limited information about how regions are interconnected in three-dimensional space."

The citation of Gustav Herdan below, given by E. E. Underwood in [46], well describes the purpose of the two-dimensional quantitative microstructural analysis performed in this work.

"But although absolute dimensions of particle size may not – because of the lack of uniqueness of that concept – be attainable, we may yet arrive at valid comparisons… by using the appropriate statistical technique, and so provide the type of information which is needed in particle technology."

Thus, the chosen microscopic technique must reflect the purpose of the wanted results. In the context of this work, the latter cited philosophy means that the aim is not to determine absolute particle sizes, but to arrive at valid comparisons between samples treated under varying conditions in order to detect any differences in the microstructural changes. Quantitative results should be used carefully and always be correlated to qualitative impressions from the images.

2.3.5 Focused Ion Beam-SEM and three-dimensional microscopy

Microstructural analysis on a selected long-term tested cell was performed by three-dimensional reconstruction using a microscope combining focused ion beam (FIB) and SEM. The microscope and the software used in this work are presented below, while the procedure for acquiring the data and the image reconstruction are presented separately in Chapter 6 followed by the results.

2.3.5.1 The microscope

The FIB-SEM work was performed during a five week visit to the Department of Materials Science and Engineering, University of Florida, in collaboration with Professor Eric Wachsman and graduate student Danijel Gostovic. A dual-beam FEI Strata DB 235 FIB / SEM situated at the Major Analytical Instrumentation Center, University of Florida, was used.

The FEI Strata DB 235 is equipped with both a FEG-SEM and a liquid-Ga ion gun, at a coincident angle of 52°. The SEM and the FIB can be operated between 0.2-30 kV and 1-30 kV, respectively. The FIB enables material etching with an accuracy within 10-20 nm. A gas injection system enables electron beam or ion beam assisted deposition of Pt, with a precision within a few tens of nanometers. The system is equipped with scripts for computer aided "slice and view" operation, where the

microscope automatically can acquire image series by sequential ion milling and SEM imaging.

2.3.5.2 The software

3D visualization software Amira 4.1, Mercury Computer System Inc, was used to reconstruct and visualize the acquired images. Amira enables automatic, semi-automatic or manual alignment of image-stacks representing a volume. The program also enables image segmentation by grey-scale thresholding or a variety of manual interactive segmentation tools.

3 Application of low-voltage scanning electron microscopy for Ni-YSZ*

In this chapter, a technique for visualizing the degree of percolation of the electrically conducting Ni-phase by low-voltage SEM is described and evaluated. The inlens secondary detector in the Supra 35 FE-SEM, Zeiss, is utilized and applied to a non-coated sample surface. In addition, a technique for attaining contrast between Ni and YSZ is described. This technique is also based on low voltage applied on the same type of samples and the same microscope as above, but with the ordinary lateral secondary electron detector.

A combination of these two techniques offers the possibility to fully characterize the microstructure of the Ni-YSZ anode, providing parameters such as size and distribution of all four components (percolating Ni, non-percolating Ni, YSZ and pores).

3.1 Introduction and background

It is of interest to develop a technique to visualize percolation of the electronically conducting phase within the SOFC electrodes, because the interconnectivity determines the amount of active reaction sites in the electrode which in turn governs a main part of the cell performance. In this context, charge contrast has been used to image phases with different electrical conductivity in low vacuum or environmental SEM, where the degree of charging can be manipulated via variable gas pressure [48]. In high vacuum SEM the main part of the early published work making use of charge contrast, such as imaging the percolating conductive fillers in an isolating PVC matrix [49], distinguishing percolating / non-percolating indium clusters in indium films [50], and visualization of alumina particles in an aluminum matrix [51] has been performed at intermediary to high acceleration voltages (10-30 kV) using Everhart-Thornley (E-T) type detectors. The recent developments of the FE-SEM equipment have given rise to new possibilities of imaging phases with different electrical conductivity. Johansen et al. [52] have utilized low-voltage SEM to study the connectivity between crystal grains in laser-fractured fluoride materials. They observed that at low voltages, non-connected grains charge positively and

* The content of this chapter has been published as K. Thydén, Y.L. Liu and J.B. Bilde-Sørensen, *Microstructural characterization of SOFC Ni-YSZ anode composites by low-voltage scanning electron microscopy*, Solid State Ionics **178** 1984-1989 (2008).

appear dark, whereas the same grains charge negatively and appear bright at high voltages.

With regard to contrast between Ni and YSZ; the backscatter coefficient for materials is often considered to be independent of the acceleration voltage. This is generally true when the acceleration voltage is limited to a range of > 5 kV. However, FE-SEMs which deliver sufficient intensity and imaging resolution at low voltages have recently become available. From experimental data in the literature the backscatter coefficient for acceleration voltages in the range of 1-5 kV is often seen to vary with the acceleration voltage [53]. It is of interest to explore these variations and investigate the possibility to achieve contrast between Ni and YSZ at lower voltages in a FE-SEM.

3.2 Theory

3.2.1 Contrast between percolating Ni and non-percolating Ni

It is well-known that many materials have a secondary emission coefficient (δ) higher than 1 in the low-voltage range. In Figure 3-1 (a-b) the secondary electron (SE) coefficient for pure Ni is shown as a function of acceleration voltage. Figure 3-1a is an illustration of existing SE data collected by D.C. Joy [53] and Figure 3-1b is a schematic drawing which illustrates the contrast mechanism. In the range around 1 kV, the secondary electron yield for Ni is high, reaching a maximum at approximately 1.3. For Ni which has a percolation path to ground, a high secondary yield will be obtained. However, the non-percolating Ni and the insulating phases cannot be effectively supplied with electrons to replace those emitted as SE. As a consequence, these phases will charge positively [54]. The charging will increase until the sum of emitted electrons is suppressed to equal the amount of the incoming electrons as expressed in equation **(3-1)**.

$$\eta + \delta_T = 1 \qquad \textbf{(3-1)}$$

In this equation η is the backscatter coefficient and δ_T is the total SE coefficient presented in equation **(3-2)**. The SE have energies in the range below 50 eV, with the majority of the signal in the range < 10 eV, which means that only a small positive charge is needed to suppress the SE yield until $\delta_T = 1 - \eta$. Since $\eta \approx 0.3$

for Ni, this corresponds to $\delta_T \approx 0.7$ for the non-percolating Ni. δ_T is marked as a dashed line in Figure 3-1b and the value of η is taken from calculations presented in the following section.

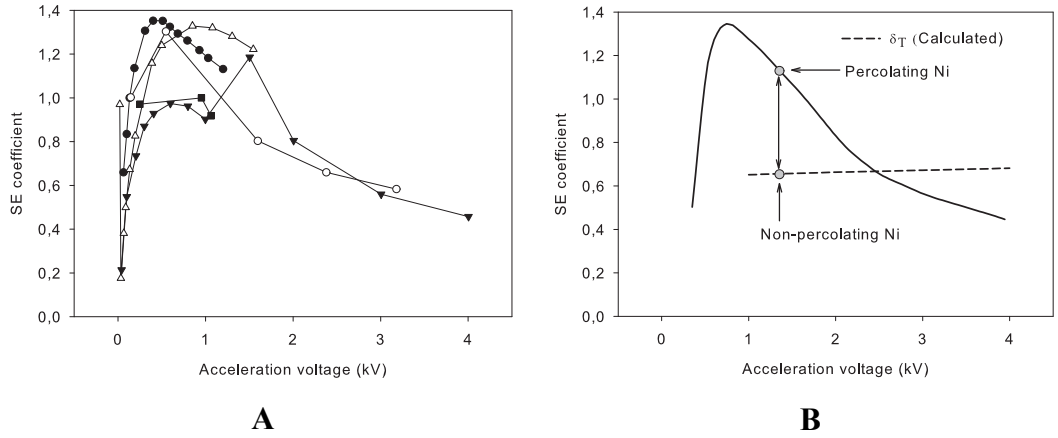

Figure 3-1. Secondary electron coefficient for Ni as a function of acceleration voltage. (a) compiled data from literature [53] and (b) a schematic drawing illustrating the contrast mechanism.

The inlens detector at a short working distance picks up the primary SE (SE_1) signal much more efficiently than the lateral SE detector [55]. Thus, the SE_1 part is dominant in the signal collected by the inlens detector and a contrast which is due to SE_1 can be expected in an inlens image.

3.2.2 Contrast between Ni and YSZ

The total electron yield from a sample in the SEM is the sum of backscattered and secondary electrons (BSE & SE). There are in general three principally different SE signals defined in SEM. The SE_1 is generated by the primary electrons of the incident beam, and the SE_2 is generated by the outgoing BSEs. The SE_1 signal is a function of the secondary electron coefficient (δ_1) of the investigated material, while the SE_2 signal is a function of δ_2 and η. Thus, the total SE signal emerging from the sample surface is a function of δ_T when expressed in the following way

$$\delta_T = \delta_1 + \delta_2 \eta \,. \qquad \textbf{(3-2)}$$

Due to the angle distribution and energy reduction of the backscattered electrons, δ_1 and δ_2 are not equal and the ratio δ_2 / δ_1 is generally in the range of 3 to 4, but varies with the acceleration voltage [55,56].

The third type of SE (SE_3) is generated by BSEs emitted from the sample surface, which collide with the pole pieces at the bottom of the electron column in the SEM. The SE_3 signal is a function of η and this indirect backscatter electron signal is collected by a lateral SE detector [55]. A lateral SE detector will detect all three types of SE signals and will therefore give an image where the contrast not only depends on δ but also on η and the geometry of the pole pieces and the detector.

η is often assumed to be dependent on Z in single element materials or on the mass fraction in a compound, but to be independent of the acceleration voltage. The Z dependence is often a good approximation, but more correctly the dependence is on the number of electrons or the electron fraction [57]. The voltage independence is only true when an intermediary to high acceleration voltage is applied. At lower voltages the available data for backscatter yield is incomplete, but in general a change in η at low voltages can be seen from published data [53]. In the present work, a number of Monte Carlo calculations of the backscatter coefficients for Ni and YSZ as a function of acceleration voltage have been performed. The calculations were based on different models available in the software Casino [58]. The results from the various models differed to some extent with respect to the absolute values of η, but on the other hand it was a general trend that η is almost constant for YSZ in the range 1-10 kV, while it for Ni increases with decreasing voltage. Figure 3-2 shows one of the calculations of η for Ni and YSZ at different acceleration voltages (here the choice of models were Browning for the total cross section and the partial cross section and Casnati for the effective section ionization). An ordinary backscatter detector is not efficient at such low voltages, but the difference in η can be readily detected by a lateral SE detector as mentioned before.

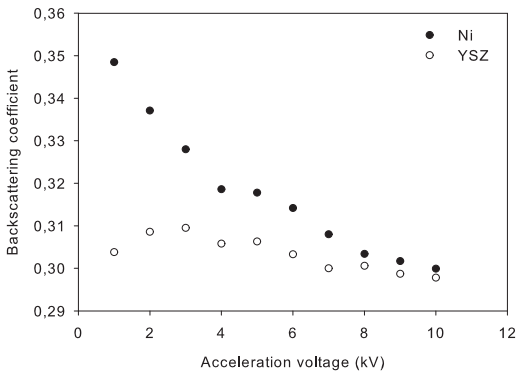

Figure 3-2. Illustration of the results from Monte Carlo calculations of backscatter coefficients for Ni and YSZ as a function of acceleration voltage.

3.3 Materials and Experimental

Cross sections of epoxy impregnated porous Ni-YSZ samples were prepared as for ordinary SEM imaging, see Chapter 2. No conductive coating or further treatment was applied to the sample surface. The samples were grounded to the sample stage in the microscope, either via a metal wire from the sample through the epoxy, or via a carbon tape attached to the polished sample surface. In order to achieve a sufficient signal / noise ratio, Carl Zeiss SMT Ltd recommends an acceleration voltage ≥ 1 kV for the lateral SE detector whereas an acceleration voltage down to 100 V is applicable for the inlens SE detector [45]. Images from optical microscopy, X-EDS mapping and ordinary SEM, from the same sample area, were also used in order to evaluate and compare images from the two presented contrast mechanisms.

3.3.1 Imaging by inlens SE detector

In order to achieve optimum contrast between percolating and non-percolating Ni, the parameter window was probed with regard to acceleration voltage, working distance, scan speed, beam current and sample preparation. To avoid charging from the surrounding epoxy, carbon tape was applied to the epoxy surfaces close to the sample. The optimum acquisition conditions were found to be: acceleration voltage 0.6-0.8 kV, working distance 3-5 mm, and frame time 0.1 sec / frame. In order to obtain a sufficient signal / noise ratio, 200 images were superimposed to form one image. In images taken under these optimum conditions, such as the image in Figure 3-3, the percolating and the non-percolating Ni grains can be clearly distinguished, i.e. the former are bright, and the latter (together with YSZ and epoxy) appear dark.

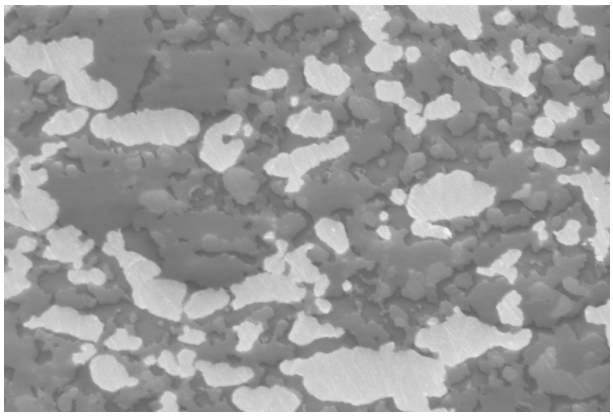

Figure 3-3. Image recorded by use of low voltage and the inlens SE detector (same area as in Figure 3-6). The bright phase is percolating Ni and the dark parts are non-percolating Ni and non-conducting phases.

No difference could be seen depending on how the samples were grounded (metal wire or carbon tape). The effects of acceleration voltage and scan rate are evaluated and illustrated below.

3.3.1.1 Effect of acceleration voltage

The maximum contrast was obtained between 0.5 and 1.0 kV, which correlates well with what can be expected from Figure 3-1 above. The contrast between percolating and non-percolating Ni also decreases with increasing voltage as predicted in Figure 3-1. The effect of acceleration voltage is illustrated by the images shown in Figure 3-4 (a-c).

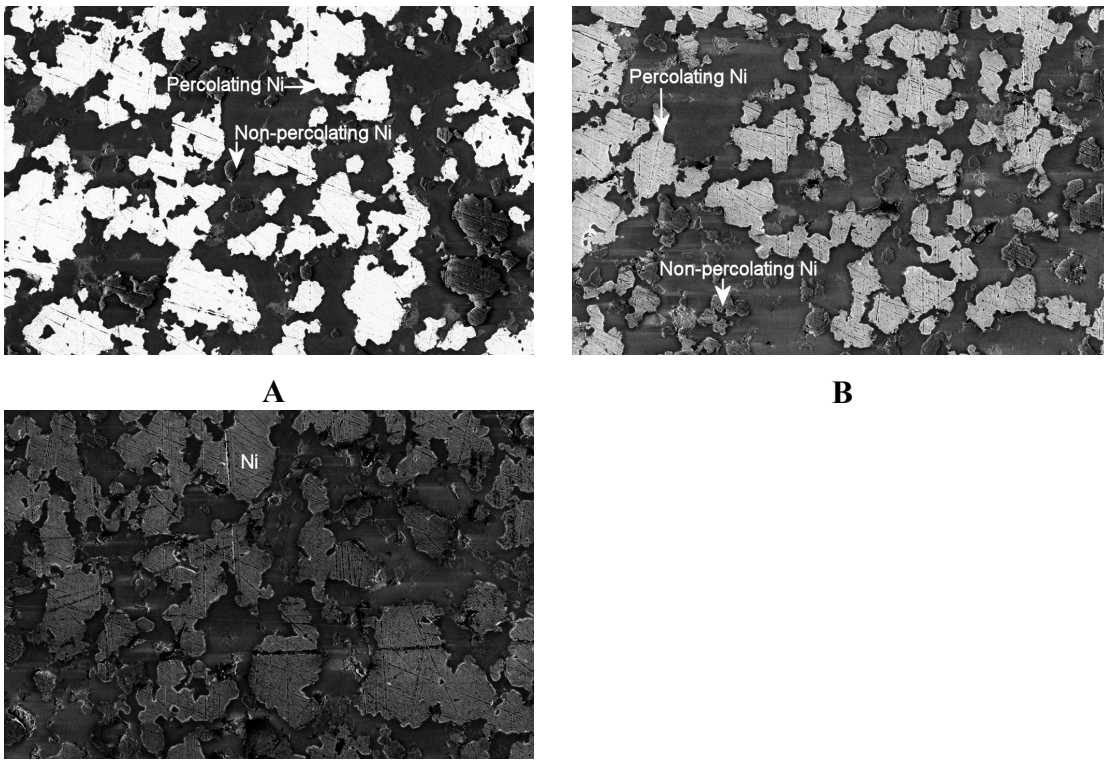

Figure 3-4. Illustration of the effect of acceleration voltage on the contrast between percolating and non-percolating phases using (a) 1.0 kV, (b) 1.6 kV and (c) 2.2 kV. [Images acquired by J. B. Bilde-Sørensen]

3.3.1.2 Effect of scan rate

The maximum contrast was found in images acquired using relatively slow scan rates (20 sec / frame). The contrast between percolating and non-percolating Ni decreases with increasing scan rate. This is a transient effect that arises because the beam dwell time at each pixel is shorter under a faster scan. Hence, there is less time

for a sufficiently large positive charge to build up in the non-percolating Ni to suppress the secondary yield. As a result, the non-percolating Ni appears brighter than when imaged with a slow scan rate, see Figure 3-5 (a-b). It is interesting to note that for images recorded by slow scan rates, the non-percolating Ni grains appear brighter at the upper left edges (Figure 3-5a), while for images recorded by faster scan rates almost the whole non-percolating Ni particles appear brighter (Figure 3-5b). This indicates that a certain amount of time is needed for the positive charge to build up to attain sufficient suppression of the SE-signal. This is also confirmations that the contrast is caused by positive charging.

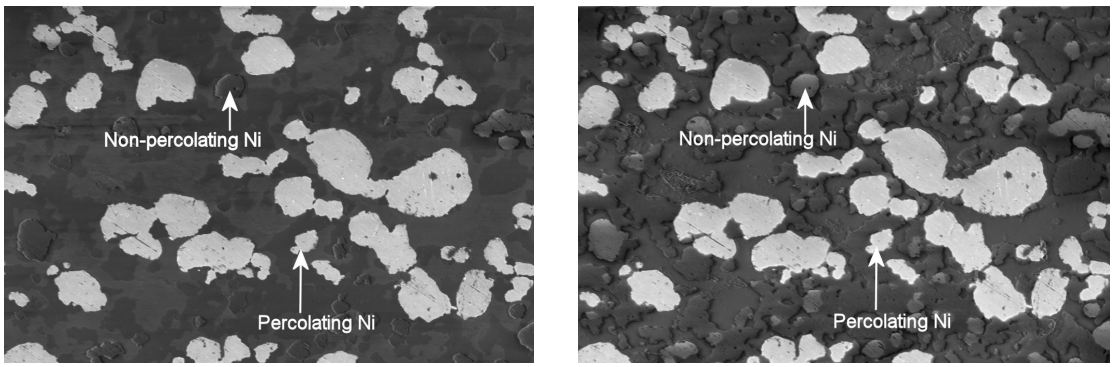

A **B**

Figure 3-5. Illustration of the effect of scan rate on the image formation. The scan rate is (a) 20 sec / frame and (b) 0.1 sec / frame.

Even though maximum contrast is attained at slow scan rates (Figure 3-5a), the optimum conditions for image acquisition was in practice defined to be at faster scan rates, as shown in Figure 3-3 and Figure 3-5b. The reasons for this definition are: 1) the contrast in images obtained by faster scan rates is sufficiently good, 2) disturbances due to undesirable charging in the images acquired are reduced, and 3) some contrast between YSZ and epoxy is also attained.

3.3.2 Imaging by lateral SE detector

Acceleration voltage and working distance were varied in order to find the optimum contrast between Ni and YSZ. At 1 kV, the signal reaching the detector was low, but it was still possible to acquire images with a sufficient signal / noise ratio. The contrast between Ni and YSZ is illustrated in Figure 3-6, where the bright phase is Ni, the grey phase is YSZ and the dark phase is epoxy.

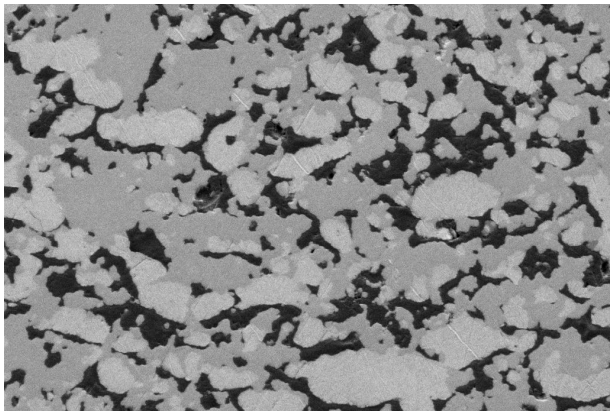

Figure 3-6. Image recorded by use of a low voltage and the lateral SE detector. The bright phase is Ni, the grey phase is YSZ and the dark phase is epoxy.

3.4 Application

By combining the two techniques, all four different components in the Ni-YSZ anode, i.e. percolating Ni, non-percolating Ni, YSZ and pores can be readily distinguished. After application of basic image processing and analysis to Figure 3-6 and Figure 3-3, which were taken from exactly the same area, all four components were mapped into a single image (Figure 3-7) and parameters such as size, shape, and volume fraction can be measured.

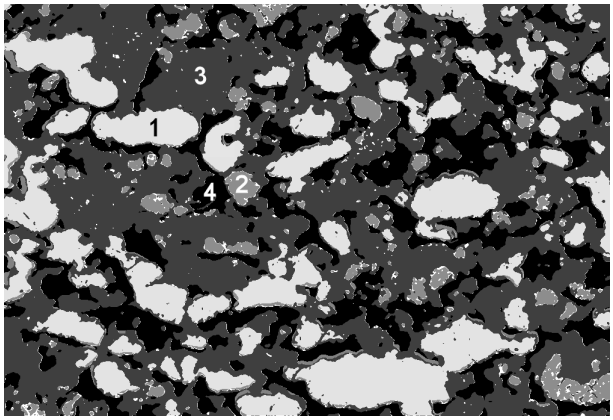

Figure 3-7. Image combining the segmented phases from the two contrast techniques (Figure 3-6 and Figure 3-3) to give information on all four components, (1) percolating Ni, (2) non-percolating Ni, (3) YSZ and (4) pores.

The contrast between percolating and non-percolating Ni allows for correlating the microstructure of this composite electrode with the electrical properties, and also for evaluation of how well dispersed the percolating Ni grains are. In these materials, the electronically conducting phases do not only have to contribute to sufficient conductivity, but it should also be well dispersed in a network to generate a high

density of active reaction sites. The latter is not necessarily revealed by pure conductivity measurements and the technique is therefore useful for studies of SOFC composite electrodes. The technique has also been successfully applied to strontium doped lanthanum manganite (LSM)-YSZ cathode composites.

The low-voltage charge contrast method is difficult to apply to samples that are thinner than ~50 μm and surrounded by non-conductive mounting materials. The charging caused by the surrounding mounting materials disturbs the low energy electrons and results in image distortion. This undesirable charging can be avoided if conductive mounting materials are used instead. In this work, 250 μm thick samples were studied and it was not necessary to acquire images close to the non-conducting mounting materials. In this way, the undesirable charging from epoxy could be avoided.

Furthermore, it is also important to keep the sample clean and free of dust. As is well-known, a single dust particle, which is negatively charging, can produce a dark ring with a diameter of up to several millimetres around the particle. The ring arises because the potential difference between the particle and the surface around it creates a radial field directed towards the particle. The secondary electrons emitted close to the particle are captured by this field and returned to the specimen rather than being collected by the detector [59]. In agreement with this we have observed that the presence of a dust particle can eradicate the contrast from percolating Ni at rather large distances from the particle.

3.5 Conclusions

This work shows that the application of low acceleration voltages (≤ 1 kV) in the FE-SEM Zeiss Supra 35 renders it possible to obtain two useful types of contrast between the different phases in Ni-YSZ composites. It also shows the importance of using various sample preparation methods, microscope settings and detectors to pick up the relevant signals that contain the phase information of interest. By changing from the ordinary lateral SE detector to the inlens SE detector, while using similar microscope settings, two very different sample characteristics are probed.

1) The difference in secondary emission coefficient δ between the percolating and non-percolating Ni is maximized in the low-voltage range due to the high δ (> 1) for the former and the suppression of δ by a positive charge for the latter. This difference is picked up by the inlens detector, in which SE_1 is dominant.

2) The difference in backscatter coefficient η between Ni and YSZ increases with decreasing voltage. The contrast is shown in images collected by the normal secondary detector since parts of the secondary signals (SE_2 and SE_3) are generated by backscattered electrons.

The application of low voltage allows the usage of an uncoated sample surface, which is essential for achieving images with the contrast based on the mechanisms described.

4 High temperature aging of Ni-YSZ cermets

4.1 Introduction and background

One of the main degradation and aging mechanisms for the Ni-YSZ cermet anode is rearrangement and coarsening of the metallic Ni phase [1,23]. The function of the Ni phase is to provide a high number of TPBs at the electrolyte interface and an electronic conduction path throughout the anode and the anode support. These functions can be significantly altered if the Ni phase is not stable during operation. Electrochemical cell testing is often accompanied by microstructural studies. These studies yield valuable information about the effect of operating conditions on the cell degradation in general, including changes within the anode structure. However, it is difficult to define local conditions such as gas composition, polarization and temperature in an operating anode [24]. This makes it even harder to define the effect of local conditions on any degradation mechanisms. By performing high temperature aging experiments on Ni-YSZ cermets and subsequent microstructural analysis, Ni rearrangements can be studied in a defined uniform environment. This type of model experiments provides a possibility to correlate changes to certain conditions or material systems. A number of studies have been reported on the degradation of Ni-YSZ cermets, but the sintering and microstructural changes of Ni-YSZ cermets are still not fully understood.

A combination of high temperature aging, conductivity measurements and microstructural studies has previously been utilized to study changes in Ni-YSZ cermets. The purpose of these studies has been to compare the effect of different material compositions, volume fractions and processing parameters [2,60-62]. Similar studies, but with the focus on establishing relations between conductivity / microstructure [43,63,64] and sintering mechanism [65] have also been reported. The main reasons for Ni coarsening is expected to be a high surface energy of Ni and the fact that Ni does not wet YSZ, whereas surface diffusion of Ni atoms on Ni particles is proposed to be the dominant mechanism for coarsening [60,65,66]. However, the existing reports are studies from aging at 1000°C and at relatively dry conditions (<5% H_2O). Ni sintering behavior has also been reported to be affected by the H_2O partial pressure from small variations in the low range [2], but the isolated effect of high H_2O partial pressure on the microstructure has not been reported. The H_2O concentration at a fuel cell anode can be expected to be up to 65-85%, depending on

the fuel gas and fuel utilization. An effect of high H_2O concentration on the sintering of Ni steam-reforming catalysts has, however, been reported [67,68]. Even though steam-reforming catalysts consist of smaller Ni particles it is reasonable to expect an effect of high H_2O partial pressure also within the Ni-YSZ anodes.

In this work, Ni-YSZ cermets representing a typical anode support were aged under various conditions concerning temperature, atmosphere and current load for a period of 300 hours. The electrical conductivity was measured in-situ and the resulting microstructure was studied in order to evaluate the effect of the different aging conditions.

4.2 Thermally induced microstructural changes

At elevated temperatures the Ni phase in a Ni-YSZ cermet can rearrange and transform by a number of material transport mechanisms. In order to understand the potential microstructural changes, a short introduction to the subject of thermally induced microstructural changes is given below. The different transport mechanisms are reviewed and their possible effects on the microstructure of a Ni-YSZ cermet are discussed.

4.2.1 The driving force for sintering and coarsening

The driving force for thermally induced microstructural changes is a reduction of the interface and grain boundary energies of the material. The surface energy (i.e. the interface energy between solid and surrounding gas) for a given material depends on the size and shape of the particles or grains that the material consists of. S.-J. L. Kang [69] derives two important equations for expressing the size and shape dependency. This is done by assuming equilibrium between condensed phase α and vapor phase β of a single component system, separated by a curved interface. When α is a solid and β is a dispersed phase that follows the ideal gas law, S.-J. L. Kang arrives at equation **(4-1)** and **(4-2)**.

$$P^{\alpha} = P_{\infty} + \frac{2\gamma}{r} \qquad \textbf{(4-1)}$$

$$P^{\beta} = P_{\infty} + \frac{2\gamma}{r}\frac{P_{\infty}V_m^{\alpha}}{RT} = P_{\infty}\left(1 + \frac{2\gamma V_m^{\alpha}}{RTr}\right) \qquad \textbf{(4-2)}$$

In these equations, P^{α} is the bulk pressure of the solid material, γ is the surface energy, r is the radii of curvature, P^{β} is the vapor pressure of α, V_m^{α} is the molar volume of α, and P_{∞} is the pressure when r approaches infinity. From **(4-1)** it can be seen that the bulk pressure of the solid, P^{α}, will increase when r is positive and decreasing. Similarly in **(4-2)**, the vapor pressure of α, P^{β} will also increase when r is positive and decreasing. From these equations three thermodynamic gradients can be found at a curved interface; bulk pressure, vapor pressure and vacancy concentration. The gradients will act simultaneously to induce material transport and reduce the surface energy. All gradients are dependant on surface energy and surface radii.

There will always be a driving force for matter to strive towards positions within the microstructure where the surface energy is lower. The overall result from these microstructural changes will ultimately be a reduction of the total surface area. The energy gained by this surface area reduction, which is also another way of explaining the overall thermodynamic driving force, comes from the fact that

$$\gamma_{S-S} < \gamma_{S-V} \,. \qquad \textbf{(4-3)}$$

$\gamma_{S\text{-}S}$ and $\gamma_{S\text{-}V}$ are the surface energy between solid-solid and solid-vapor, respectively.

4.2.2 Sintering of particles in contact

Sintering and annealing are terms used to describe heat treatments of materials in order to deliberately attain a microstructural transformation. The purpose of sintering can be to transform a powder compact into a dense material, by elimination of porosity, or to make the powder particles bond to each other without densification. In the initial state of this process the material most often consists of particles in physical contact but without any strong bonding. During heat treatment, the outcome of the process depends on the diffusion mechanism of which matter is transported within the material. In the literature, six different transportation mechanisms are often defined, which are presented in Figure 4-1 and Table 4-1. Matter will diffuse towards the lowest energy position, which is the contact point between particles, where the surface radius is small and negative. The result is formation of a neck between the particles.

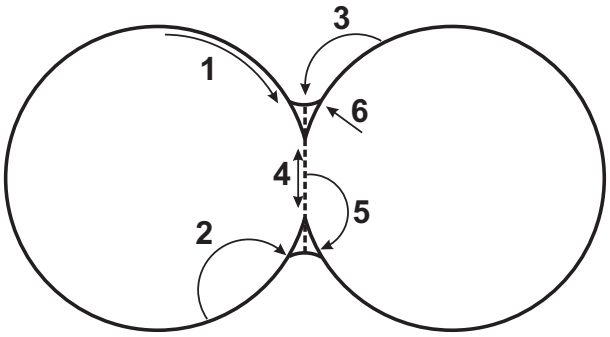

Figure 4-1. Illustration of diffusion mechanisms during neck growth between two particles [70].

Table 4-1. Summary of diffusion mechanisms illustrated in Figure 4-1.

Mechanism	Transport path	Source of matter	Sink of matter
1	Surface diffusion	Surface	Neck
2	Lattice diffusion	Surface	Neck
3	Vapor diffusion	Surface	Neck
4	Boundary diffusion	Grain boundary	Neck
5	Lattice diffusion	Grain boundary	Neck
6	Lattice diffusion	Dislocations	Neck

Which diffusion path(s) that will be dominating depend on numerous factors, e.g. material, temperature, particle size and size distribution, atmosphere, impurities and defects present. Vapor phase, surface or bulk diffusion involving transport of matter from the particle surface to the neck will not affect the position of the particle centers. Thus, when matter is transported from the surface to the neck this will not lead to shrinkage or densification. The effect of diffusion of material only from the surface is illustrated to the left in Figure 4-2. On the other hand, if matter is transported from the grain boundary between particles to the neck, this type of sintering will bring the centre of the particles closer together as illustrated to the right in Figure 4-2.

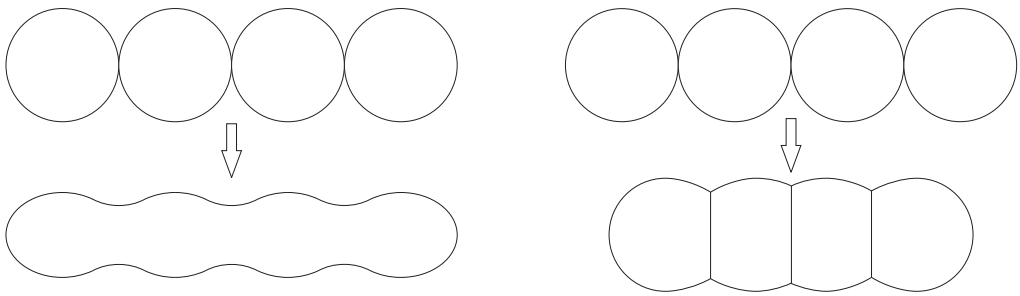

Figure 4-2. Schematic illustration of the effect of matter diffusing from the surface (left) and from the grain boundary (right) on a row of close-packed spheres [70].

The driving force for sintering via neck formation will initially be high, but it is reduced when material comes from the particle surface to the neck. This is due to fact that the shape of particle surface near the neck will become less rounded (larger radius of curvature). This phenomenon is called under-cutting, see S.-J. L. Kang [69] and references within.

R. Vassen et al. [65] describe the Ni sintering within a Ni-YSZ cermet under the presumption that undercutting has already taken place, thus the driving force for neck formation is no longer present. Instead, the size difference of adjacent particles is ascribed to be the driving force for Ni rearrangements and the cause of coarsening and conductivity loss. Since the smaller Ni particle has a smaller surface radius, and thereby a higher surface energy, matter will diffuse towards the larger particle. Also in this case, when the driving force is the difference in particles size, the 6 alternative diffusion paths presented in Table 4-1 are still applicable.

4.2.3 Sintering of particles without physical contact

Particle diffusion and coalescence is closely related to sintering. In this model the particles are not initially in contact but have the ability to move towards each other and merge into larger particles. This model involves a certain degree of particle movement and is often encountered in the area of supported metal catalysis [71]. The particle movement on a surface is driven by topography of the supporting material and random movement of the particles. When two particles collide, the process of coalescence can be described as sintering. Particle migration is shown to be reduced as the particle diameter is increased in the range between 10-100 nm [67]. In a Ni-YSZ anode structure it is reasonable to assume that all the Ni-particles have a diameter larger than 100 nm. At the same time, particle movement should also be highly constrained by the YSZ-network.

Ostwald ripening is another mechanism that can play a role for Ni particle coarsening within a Ni-YSZ cermet. In this model no physical contact exists between the particles and no neck formation takes place. The driving force for this mechanism is also a difference in size and size distribution between particles. As mentioned above, a small particle has a higher surface energy than a larger particle. Ostwald ripening assumes that atoms from the small particle are able to diffuse via a surrounding media (e.g. gas or YSZ surfaces) to the larger particles. The overall effect

of this mechanism is that large particles grow on expense of small particles, which at the same time will lead to a reduction of the total surface energy.

4.2.4 Ni atom mobility

All the microstructural rearrangements of the Ni phase discussed above involve mechanisms in which Ni atoms have a certain degree of mobility. These mechanisms are assumed to be thermally activated. Hence, Ni atoms gain mobility at elevated temperatures. The problem is to understand through which path(s) the major or crucial rearrangements will occur. This is a difficult task, not only because the Ni-YSZ microstructure in it self is a complex system, but also because during cell operation there are concentration and polarization gradients present within the material. These gradients may well alter the mechanism locally.

As mentioned above, it has been suggested that surface diffusion of Ni atoms on Ni particles is the dominant mechanism of Ni sintering and coarsening within Ni-YSZ anodes. However, the sintering is largely affected by a change from dry to moisturized hydrogen atmosphere, both for Ni-YSZ and Ni steam reforming catalysts [2,72]. Within the field of SOFC, no studies concerning the presence of high H_2O concentrations have been presented. On the other hand, this is not the case within the field of supported metal catalysts research. Here, metal particle sintering is seen to be generally accelerated in the presence of H_2O vapor in reducing atmospheres. J. Sehested et al. [67] present two alternatives for Ni surface diffusion on a Ni particle surface. The first is formation and diffusion via Ni adatoms, while the second is formation and diffusion via OH-bonded Ni dimers. From density functional theory (DFT) calculations of the stability and diffusivity of these transport species, they conclude that formation of OH-bonded Ni dimers is the dominating transport mechanism for the surface transport of Ni on the particle surface. Ni dimers are found to have lower energy of formation than Ni adatoms (58 kJ mol^{-1} less).

Moreover, Sehested et al. [67,68] have demonstrated that Ostwald ripening takes place on supported Ni catalysts. Ni is seen to diffuse via the surface of the supporting material above 700°C at high partial pressures of H_2O in a reducing atmosphere at 1 bar. Even though the Ni particles in these studies are considerably smaller in comparison to what is typically found in SOFCs and the supporting material different, also this mechanism should also be considered for Ni particle growth in the anode structure.

Ni vapor phase transport has been reported, but is not well documented. A. Gubner et al. [25] report evidence of Ni evaporation at 950°C, when a gas flow of H_2 and H_2O (1:1) is applied to a Ni-YSZ anode. No microstructural changes where seen in the anode, except a diffuse whitening of the surface. This whitening is assumed to be condensed Ni. At the same time they could measure a doubled polarization resistance of the samples over 1,000 hours of testing. Further, A. Gubner et al. present thermodynamic calculations of the partial pressures of gaseous Ni species from 0.6 to 98.8 mol fraction of H_2O / H_2. They found $Ni(OH)_2$ to have the highest vapor pressure in a system of H_2O, H_2 and Ni and that the vapor pressure was seen to increase as the H_2O to H_2 ratio was increased.

4.3 Sample preparation and aging conditions

The type of samples studied in these experiments is a model material representing the anode support and is comprised of a thick anode support-layer (NiO-YSZ), an anode layer (NiO-YSZ) and a dense YSZ layer. Yttria-stabilized zirconia from Tosoh Co. and NiO from Alfa Aesar were used in the preparation of the samples. The fabrication process of the samples is described elsewhere [42]. The samples were cut into 35 × 5 mm sized tapes and sintered in air.

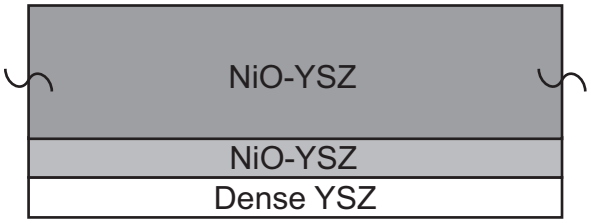

Figure 4-3. Cross sectional illustration of studied sample.

The model Ni-YSZ cermets were aged for 300 hours in different temperatures (750 and 1000°C), H_2O / H_2 atmospheres (3, 50 and 85% water) and current loads (0, 4.5 A/cm^2). The conductivity of the model anodes was monitored in-situ during aging. Subsequently, microstructural analyses were performed and correlated to the acquired conductivity data.

The experimental setup is described in Chapter 2 and the treatment conditions and corresponding sample-ID are presented in Table 4-2. The presented sample ID will in the following be used when referring to the samples.

All samples were heated to 1000°C in air and subsequently reduced according to the following procedure: When the temperature was stabilized, the gas was changed from air to 9% H_2 / Ar and after 2 hours to 100% H_2. All gases were moisturized at RT and the flow rate was 100 ml / min. After an additional hour in moisturized H_2 the specific aging condition was applied. After 300 hours the current and the O_2 flow were stopped, the gas was changed to 9% H_2 / Ar and the temperature was lowered to RT. Reference samples were prepared by the same reduction and cooling procedure, but the aging treatment was excluded. In Figure 4-4, sketches of the two different temperature profiles used are shown. The specific atmospheres and corresponding times are also indicated in the sketches. It should be noted that the time scales are not linear.

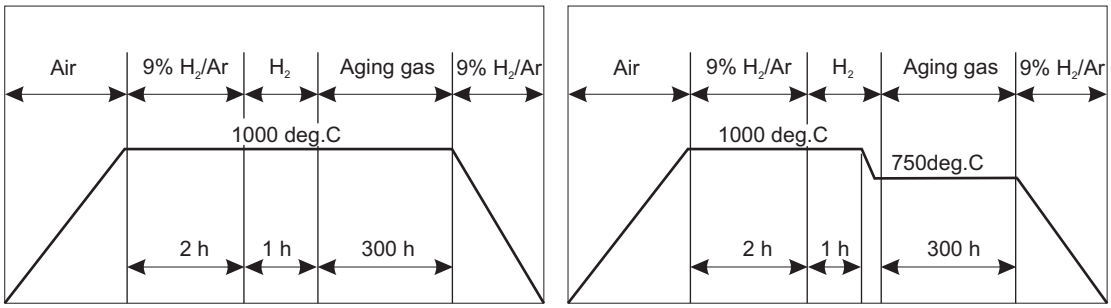

Figure 4-4. Temperature profiles including illustrations of gas shifts and times for aging treatment at 1000 (left) and 750°C (right). NB: the time scale is not linear.

The metallic characteristic of the conductivity was confirmed by measurements on the reduced cermet in the temperature range of 700-1000°C. An Arrhenius plot of the data demonstrated a linear trend in this temperature range and the activation energy was calculated to be 5.7 kJ/mol. This is in good agreement with previously reported values for Ni-YSZ cermets and in the same range as for pure Ni [61,73].

Table 4-2. Sample ID and treatment conditions for the type-1 samples. The column labeled "Heating gas" indicates the gas fed to the sample, moisturized at RT, during heating. The second and third columns indicate the conditions applied during reduction of the samples. Columns 5-7 indicate the conditions applied during the 300 hours of treatment. The gas is given by numbers indicating the H_2O / H_2 ratio (e.g. 97-3 specifies 97% H_2 - 3% H_2O).

ID	Heating gas	Reduction gas	Reduction temp./°C	Aging temp./°C	Aging gas	Current /A cm^{-2}
1-A_1	Air	9% H_2/Ar	1000	1000	97-3	4.5
1-A_2	Air	9% H_2/Ar	1000	1000	97-3	-
1-B_1	Air	9% H_2/Ar	1000	1000	97-3	-
1-B_2	Air	9% H_2/Ar	1000	1000	97-3	-
1-C_1	Air	9% H_2/Ar	1000	1000	97-3	-
1-C_2	Air	9% H_2/Ar	1000	1000	97-3	-
1-D_1	Air	9% H_2/Ar	1000	1000	50-50	4.5
1-D_2	Air	9% H_2/Ar	1000	1000	50-50	-
1-E_1	Air	9% H_2/Ar	1000	1000	50-50	4.5
1-E_2	Air	9% H_2/Ar	1000	1000	50-50	-
1-F_1	Air	9% H_2/Ar	1000	1000	50-50	4.5
1-F_2	Air	9% H_2/Ar	1000	1000	50-50	-
1-G_1	Air	9% H_2/Ar	1000	1000	15-85	-
1-G_2	Air	9% H_2/Ar	1000	1000	15-85	-
1-H_1	Air	9% H_2/Ar	1000	750	97-3	4.5
1-H_2	Air	9% H_2/Ar	1000	750	97-3	-
1-I_1*	Air	9% H_2/Ar	1000	750	50-50	4.5
1-I_2*	Air	9% H_2/Ar	1000	750	50-50	-
1-Ref_1	Air	9% H_2/Ar	1000	-	-	-
1-Ref_2	Air	9% H_2/Ar	1000	-	-	-

* The sample set 1-I was accidentally kept at 1000°C one hour longer than sample set 1-H before the temperature was reduced to 750°C.

After aging, treatment the Ni-YSZ cermets were mounted into epoxy resin under vacuum, ground and polished for both optical microscopy and SEM. Quantitative microstructural analyses were performed on the tested samples and the reference samples. The particle size and area fraction of Ni was measured and analyzed in images acquired by optical microscopy. In addition, the particle size and area fraction of the percolating Ni was measured in images acquired by SEM-CC. Nine images from optical microscopy and nine images from SEM-CC were analyzed for each sample, corresponding to a total measured area of 0.014 mm^2 and 0.04 mm^2, respectively.

4.4 Results

4.4.1 Electrical conductivity

Before the reduction, the conductivity of the NiO-YSZ was measured and calculated to be ~0.05 S/cm at 1000°C in air. After the gas was changed from air to

9% H_2 / Ar, the conductivity increased four orders of magnitude and reached a maximum after ~35 min. The maximum conductivity differed somewhat between the samples and was measured to be in the range of 500-750 S/cm at 1000°C. The initial conductivity and pO_2 is given vs. time for sample 1-F_1, tested at 1000°C with 50% H_2O, in Figure 4-5. Here it can be seen how the conductivity starts to decrease at a high rate directly after the maximum has been reached. In total the conductivity drops by 150-200 S/cm during the first three hours.

When the specific aging conditions were applied, the conductivity was seen to be affected differently by the specific aging conditions (H_2O concentration). At the point when aging conditions were initiated, the conductivity of the samples was measured to be in the range between 370-540 S/cm.

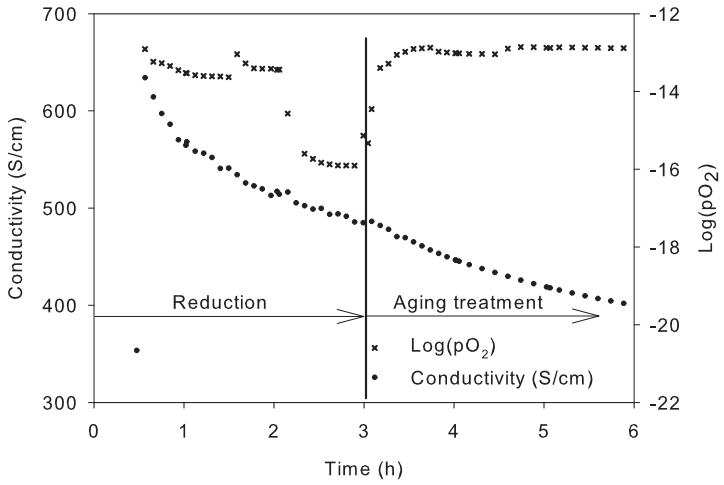

Figure 4-5. Conductivity and Log(pO_2) vs. time during the reduction and initial aging. The example is taken from the measurements performed on sample 1-F_1, which was aged at 1000°C with 50% H_2O / H_2.

The conductivity measurements from the specific aging treatments are presented in the following.

4.4.1.1.1 Aging at 1000°C in various atmospheres

The absolute conductivity (σ) and relative conductivity (σ / σ_0) vs. time for the samples aged at 1000°C with 3% H_2O are shown in Figure 4-6. σ_0 is the conductivity directly after reduction. The samples exhibit high degradation rates during the first ~25 hours, where after the rate is significantly reduced. However, the degradation rate is still significant at 300 hours. In the plot where the absolute conductivity is given, it

can be seen that sample 1-B_1 differs slightly, while from the relative plot it can be seen that the behavior of the sample pairs 1-B and 1-C are similar.

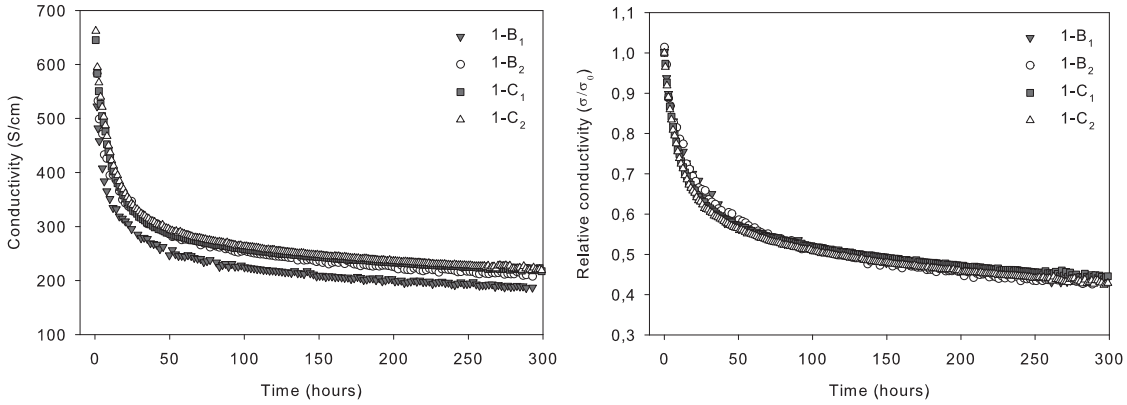

Figure 4-6. Collection of conductivity curves for samples aged at 1000°C with 3% H_2O. The conductivity is given as a function of time, where time zero is the time when reducing atmosphere is applied. To the right, the measured conductivity is normalized to the conductivity directly after reduction (3 hours).

Similar plots for the samples aged at 1000 °C with 50% and 85% H_2O are shown in Figure 4-7 and Figure 4-8, respectively. These samples demonstrate an accelerated degradation rate when the atmosphere is changed from 3% H_2O directly after reduction. The change in degradation rate can be seen in Figure 4-5 for one of the samples aged at 50% H_2O (sample 1-F_1). After this instant change, the conductivity continues to decrease in an exponential manner. Compared to the samples aged with 3% H_2O, the degradation rate is initially increased. However, the conductivity stabilizes faster and after 300 hours the samples aged in 3, 50 and 85% H_2O have conductivities in the same range. The curves for samples 1-D have an irregular behavior from 30 to 60 hours. This irregularity is caused by a temperature change in the furnace, the temperature suddenly dropped to a stable value of 980°C in this period. At 60 hours, the temperature was increased and stabilized at 1000°C again. The conductivity data for the sample set 1-E is only plotted up to 230 hours as the furnace broke down at this point. This incident caused the samples to oxidize at high temperature. The sample set 1-D was oxidized at high temperature directly after the aging treatment was finished. Because of these two incidents, no microstructural analysis could be performed on the sample sets 1-D and 1-E.

The conductivity measurements from samples aged in higher concentrations of H_2O were somewhat scattered. The scattering was most severe for the measurements performed at 85% H_2O, where no accurate data can be presented after ~75 hours of

aging. However, among the scattered data points a vague trend can be approximated up to 150 hours. Following this approximated trend the conductivity was relatively stable already after 50-75 hours. The reason for scattering at higher H_2O concentrations is not fully understood.

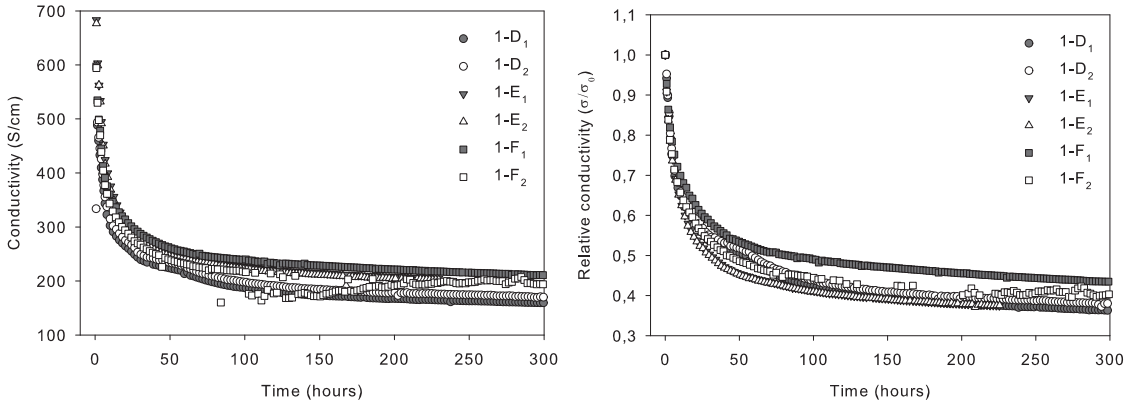

Figure 4-7. Collection of conductivity curves for samples aged at 1000°C with 50% H_2O. The conductivity is given as a function of time, where time zero is the time when reducing atmosphere is applied. To the right, the measured conductivity is normalized to the conductivity directly after reduction (3 hours).

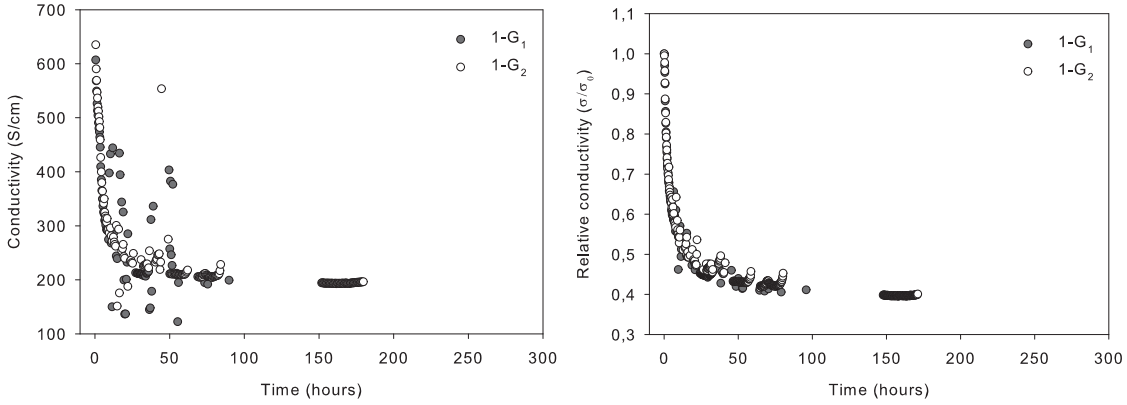

Figure 4-8. Collection of conductivity curves for samples aged at 1000°C with 85% H_2O. The conductivity is given as a function of time, where time zero is the time when reducing atmosphere is applied. To the right, the measured conductivity is normalized to the conductivity directly after reduction (3 hours).

In Figure 4-9, the relative conductivity vs. time for all samples aged at 1000°C in various H_2O concentrations is collected. The light grey, the medium grey and the black curves indicate samples aged in 3, 50 and 85% H_2O, respectively. From these figures, the effect of the H_2O concentration can be clearly seen. The rate of degradation is increased at higher H_2O concentrations. It is also clear that the effect of

H_2O concentration is most significant within the first few hours, while over a longer time, the effect is not as significant.

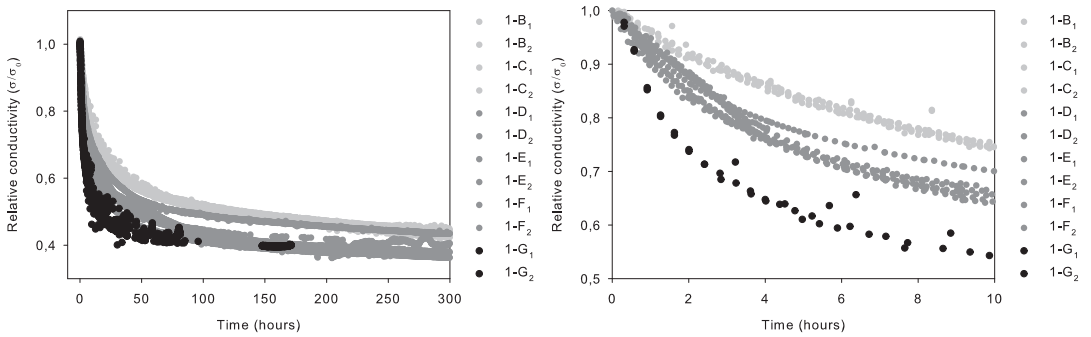

Figure 4-9. Collection of conductivity data from all samples treated at 1000°C with varying H_2O concentrations. The relative conductivity is plotted vs. time, starting from the reference point after 3 hours of reduction.

The degradation of conductivity is given at different reference times for each sample in Table 4-3. There is a clear correlation among the samples treated in similar atmospheres, however, the difference in conductivity between the samples aged under the various conditions decreases over time. No difference is seen between samples aged with / without constant current.

Table 4-3. Relative conductivity, normalized to the conductivity after 3 hours, at different times for samples treated at 1000°C.

ID	Gas	σ_7/σ_0	σ_{50}/σ_0	σ_{100}/σ_0	σ_{150}/σ_0	σ_{300}/σ_0
1-B_1	97-3	0.82	0.60	0.52	0.49	0.44
1-B_2	97-3	0.82	0.60	0.52	0.49	0.43
1-C_1	97-3	0.80	0.61	0.52	0.49	0.44
1-C_2	97-3	0.79	0.57	0.51	0.48	0.43
1-D_1	50-50	0.71	0.53	0.44	0.41	0.38
1-D_2	50-50	0.70	0.52	0.43	0.40	0.37
1-E_1	50-50	0.69	0.46	0.42	0.40	-
1-E_2	50-50	0.70	0.46	0.42	0.40	-
1-F_1	50-50	0.74	0.54	0.50	0.47	0.41
1-F_2	50-50	0.70	0.50	0.45	0.43	0.39
1-G_1	15-85	0.58	0.43	0.41	-	0.39*
1-G_2	15-85	0.59	0.43	0.41	0.40	0.39*

* Extrapolated values.

Any difference between the sample-sets with the same nominal H_2O concentration can be explained by variations in the oxygen gas flow, which was manually controlled. Due to this variation in the O_2 gas flow, the H_2O concentration in the furnace varied ~5% over time. When the gas was moisturized in water at RT in order to achieve a H_2O concentration of 3%, the variation was below ± 2%. There is a spread in the relative conductivity among the samples aged at 50% H_2O. However, after 7 hours of aging a clear difference can be seen between the different gas compositions. The samples aged in 3 and 85% H_2O display a loss of 40% at 50 and 7 hours, respectively. This means that the samples aged in 85% H_2O degrades more than 7 times faster up to this point. Over time the difference between the samples decreases. This is further illustrated in Figure 4-10, where the derivative of the conductivity vs. time is given as a function of H_2O concentration in different time intervals. The derivative is calculated as the slope of the secant between 0-2, 2-7, 7-22, 22-48, 48-100, 100-150 and 150-300 hours in the conductivity curves given above. The given rates are the averages from samples aged under similar conditions. In the first two hours the degradation rate is approximately 20, 40 and 65 $Scm^{-1}h^{-1}$, corresponding to H_2O concentrations of 3, 50 and 85%, respectively. However, already in the time interval between 2-7 hours the rate is similar for the three sets of aging conditions and later on the rate is seen to be lower for the samples treated at higher concentrations of H_2O. In the end of the aging treatment the loss of conductivity only differs with a few percent between the different aging atmospheres.

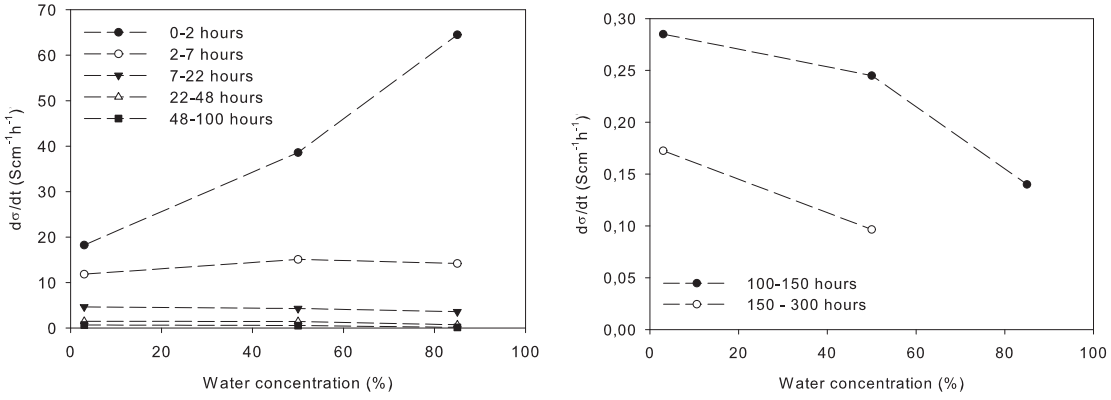

Figure 4-10. Derivative of the conductivity vs. time as a function of H_2O concentration in different time intervals for samples aged at 1000°C. The derivatives given within the first 100 hours (left) and after 100 hours (right) are given on a different scale. Data are based on the averages from samples aged under similar conditions.

4.4.1.1.2 Aging at 750°C in various atmospheres

At 750°C, the conductivity loss is significantly reduced compared to the aging treatments performed at 1000°C. However, a significant difference between the samples aged in 3 and 50% H_2O can be seen. In Figure 4-11, the absolute and relative conductivity for all samples aged at 750°C can be found. The samples aged in 3% H_2O show a linear conductivity loss throughout the 300 hours of aging. There is no sign of a decrease in the slope within this time range and the total loss over the time period is 16 S/cm for both samples, which equals a relative loss of 3.5% over the measured period. As was observed for the experiments performed at 1000°C, an increased concentration of H_2O results in an altered degradation behavior. For these samples the degradation rate is not constant, but proceeds at a higher rate initially. The total loss over the time period for these samples is 24 S/cm, which corresponds to a relative loss of 6%. In the plot of the relative conductivity, time zero is taken as the time where the temperature was stabilized at 750°C for the samples kept one hour longer at 1000°C (sample set 1-I).

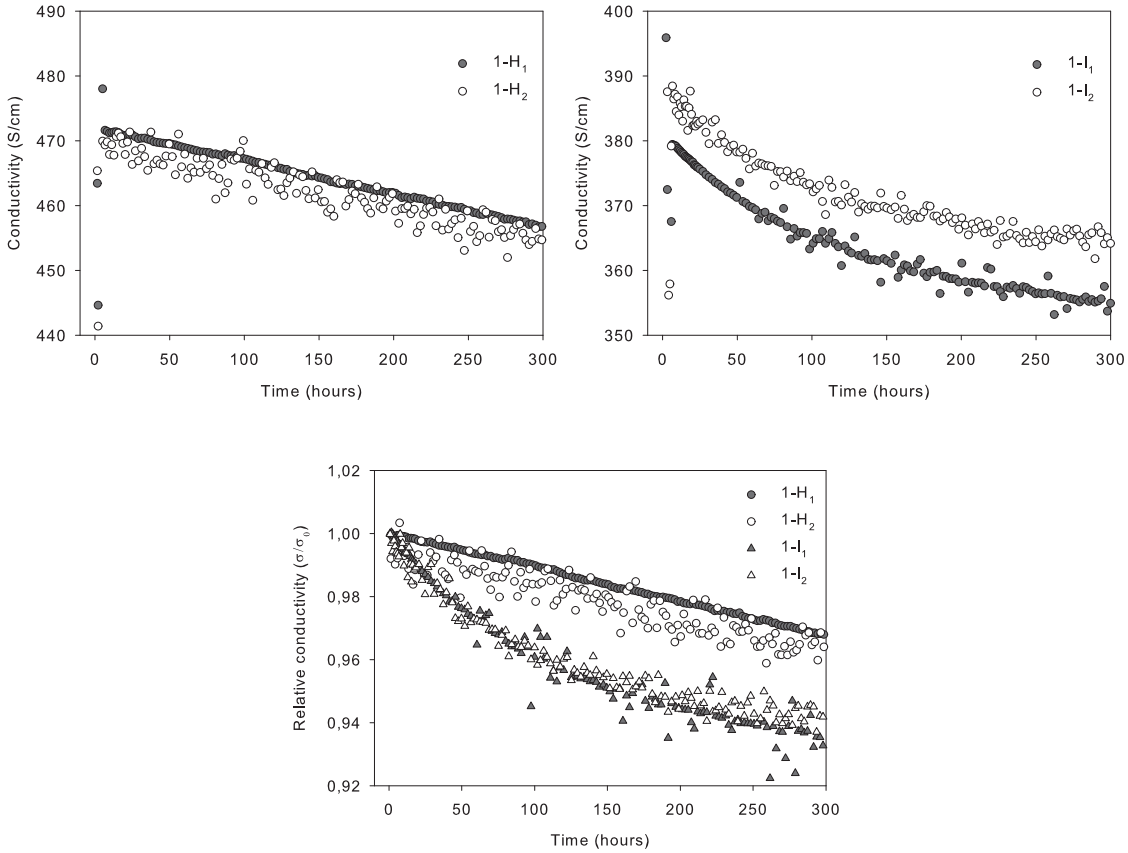

Figure 4-11. Conductivity vs. time for samples aged at 750°C in an atmosphere of 3% (upper left) and 50% (upper right) H_2O / H_2. Below is a collection of the relative conductivity for all the samples treated at 750°C.

The scattering of the data points from measurements performed without constant current is due to the fact the measured variations in resistance over the samples approaches the resolution limit of the used multimeter (Keithly 2700). The measurements at constant current were possible to perform at a higher current, which subsequently resulted in higher measured potentials.

The degradation of conductivity is given at different reference times for each sample in Table 4-4. An effect can be seen from the H_2O concentration.

Table 4-4. Relative conductivity at different reference times ($\sigma t/\sigma_0$) for samples treated at 750°C.

ID	Gas	σ_7/σ_0	σ_{50}/σ_0	σ_{100}/σ_0	σ_{150}/σ_0	σ_{300}/σ_0
1-H_1	97-3	1.00	0.99	0.99	0.98	0.97
1-H_2	97-3	1.00	0.99	0.99	0.98	0.96
1-I_1	97-50	0.99	0.98	0.96	0.95	0.94
1-I_2	97-50	0.99	0.98	0.96	0.95	0.94

In Figure 4-12, the derivative of the conductivity vs. time is given as a function of H_2O concentration in different time intervals. The derivative is calculated as the slope of the secants between 0-25, 25-50, 50-150 and 150-300 hours. In 3% H_2O, the degradation rate is constant over the entire aging experiment, thus the rate in all intervals is represented by a single point at 3% H_2O. At 50% H_2O the rate varies significantly over time. Between 0-25 hours the rate is more than 4 times higher that at 3% H_2O, while in the interval of 150-300 hours the degradation rate is lower that what was observed at a H_2O concentration of 3%. It can be noted that the degradation rates observed at 750°C (Figure 4-12) are on the same scale as the rates after longer times of aging at 1000°C (to the right in Figure 4-10).

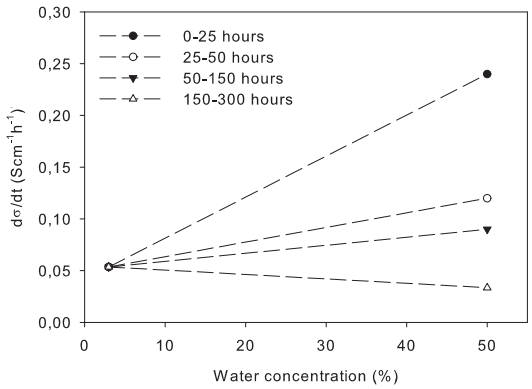

Figure 4-12. Derivative of the conductivity vs. time as a function of H_2O concentration in different time intervals for samples aged at 750°C.

4.4.2 Microstructural analysis

A selection of optical images, one for each set of aging treatments, is shown in Figure 4-13. Below each image the treatment conditions, H_2O concentration and temperature are given. Since no effect could be seen from aging with or without current, no specific images are shown concerning this parameter.

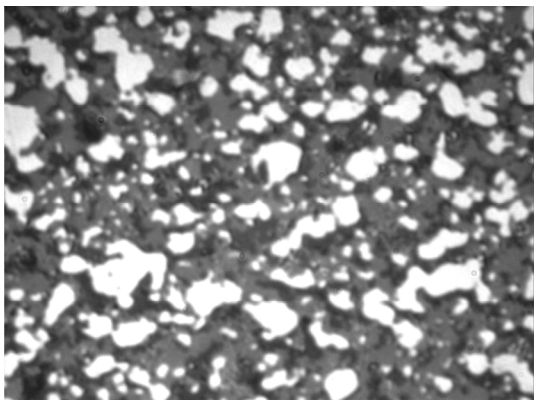

Reference

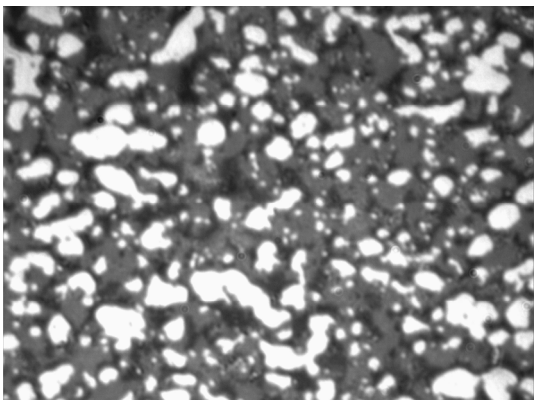

3% H_2O / H_2 – 750°C

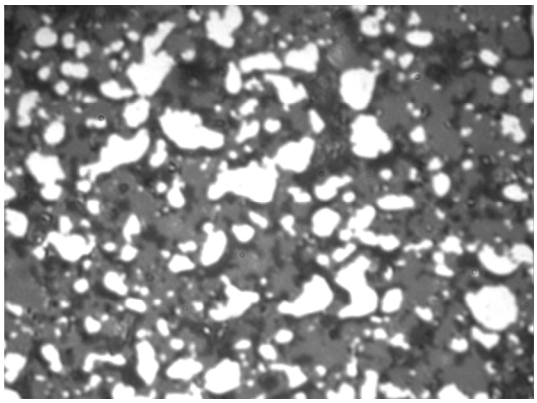

50% H2O / H2 – 750°C

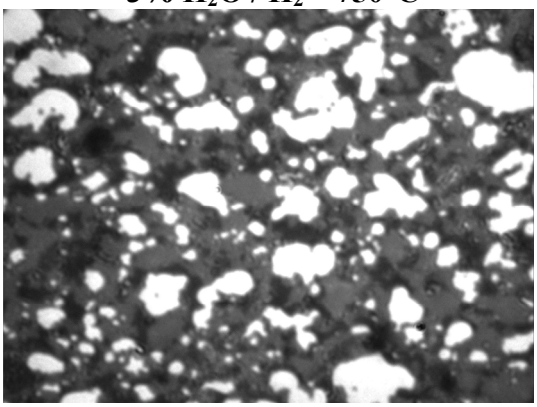

3% H_2O / H_2 – 1000°C

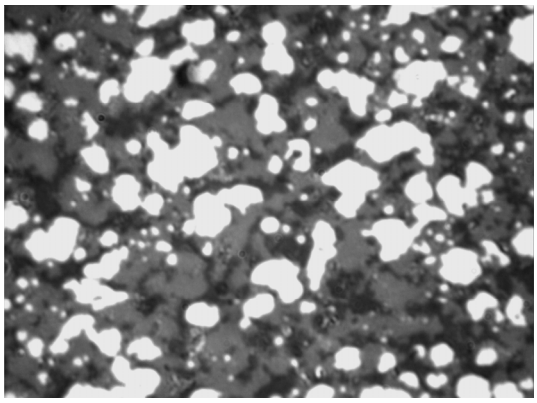

50% H_2O / H_2 – 1000°C

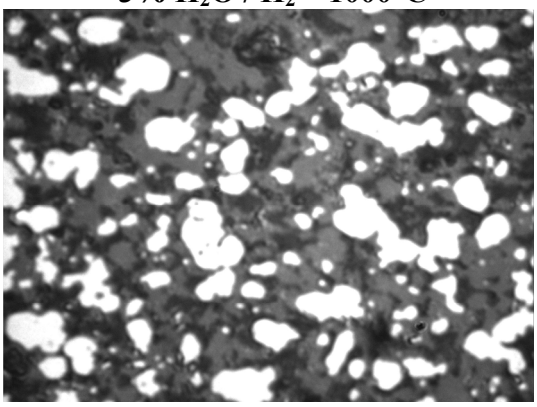

85% H_2O / H_2 – 1000°C

Figure 4-13. Optical images from cross-sections of samples aged at different temperature and in different gas compositions.

When studying the optical images above it appears to be the case that the spatial density of particles is lower in the samples aged at 1000°C. Among the samples aged at 1000°C, the particle spatial density also decreases as the H_2O concentration is increased. At the same time as the Ni particle spatial density decreases, the frequency of pores without any Ni present is increased. However, even though the density seems to decrease with higher H_2O concentrations, small particles are present in all samples. In Table 4-5, the results from the quantitative microstructural analyses from the optical microscopy are summarized, along with the specific aging conditions and the remaining conductivity after 300 hours. Only particles measured to be larger than 0.2 μm are included in the calculation of the Ni particle average diameter. The results presented in Table 4-5 are elucidated below.

Table 4-5. Microstructural data from optical microscopy including, aging temperature, aging atmosphere, remaining conductivity after 300 h, average Ni particle diameter, measured standard deviation and total number of measured Ni particles. Diameters and standard deviations are normalized to the mean diameter of the reference samples.

Sample ID	Aging T. / °C	Aging atmosphere	σ_{300}/σ_0	Normalized diameter	Standard deviation	Number of Ni particles
1-C_1	1000	97-3	0.44	1.09	1.01	1304 (76%)
1-C_2			0.43	1.10		
1-F_1	1000	50-50	0.41	1.14	1.08	1209 (71%)
1-F_2			0.39	1.14		
1-G_1	1000	15-85	0.39*	1.22	1.13	1093 (64%)
1-G_2			0.39*	1.20		
1-H_1	750	97-3	0.97	0.97	0.85	1857 (108%)
1-H_2			0.96	0.96		
1-I_1	750	50-50	0.94	1.00	0.90	1637 (96%)
1-I_2			0.94	1.00		
1-Ref_1				1.01	0.82	1713 (100%)
1-Ref_2				0.99		

* Extrapolated values.

The area fraction of Ni measured from the cross sections was not seen to vary outside the confidence interval (95%) of ±2%. The area deviation between individual images was relatively high and in order to measure the area fraction with better confidence significantly larger areas must be analyzed. The confidence interval (95%) for the normalized average particle diameter varies between 0.04-0.07. The interval

becomes wider for samples exhibiting large average particle diameters, as the number of particles becomes less and the standard deviation larger.

As expected from the measured and calculated average particle sizes, the aged samples have a size distribution shifted towards larger particles and agglomerates. This is seen as a relative increase of larger particles and a corresponding decrease of smaller particles. The most significant change is in the peak of the distribution, which becomes wider for the samples exhibiting larger particle sizes. The appearance of the particle size distributions corresponds well to the average particles sizes presented Table 4-5.

In Figure 4-14, a selection of SEM-CC images are presented. The SEM-CC images yield information exclusively from a particular type of Ni particles within the sample. The requirement for Ni particles to be visualized by this method is that they are in physical contact with other Ni particles and to ground. A change in average particle size, particle spatial density or area fraction is therefore not necessarily due to the same mechanisms as in images from optical microscopy. From the images presented in Figure 4-14 it is evident that the percolating Ni network becomes coarser after aging, especially after aging at 1000°C. The samples aged at 1000°C all exhibit larger areas without any percolating Ni, in comparison to both the reference and the samples treated at 750°C.

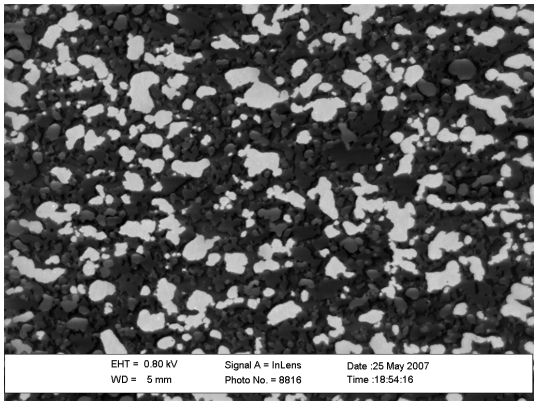

Reference

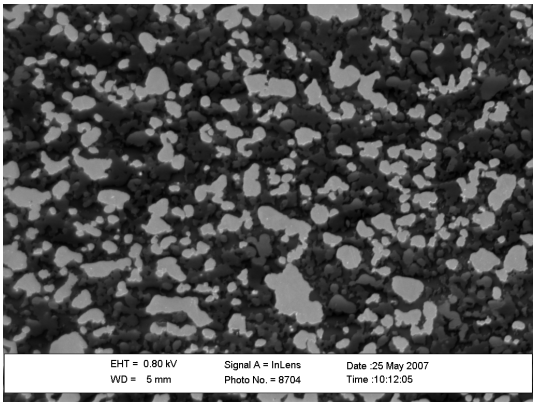

3% H_2O / H_2 – 750°C

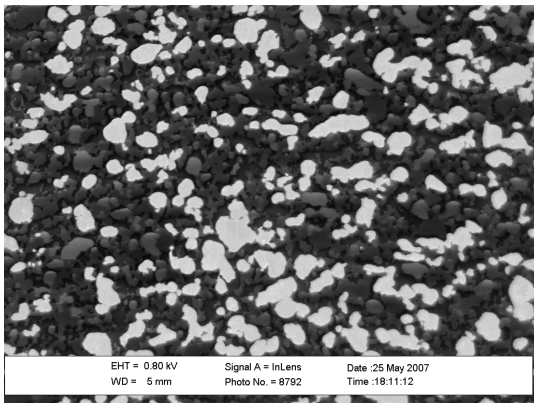

50% H_2O / H_2 – 750°C

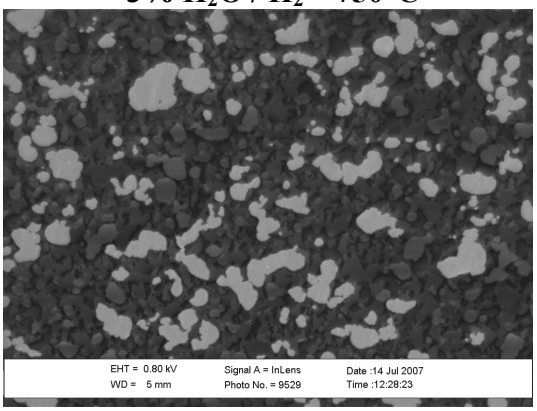

3% H_2O / H_2 –1000°C

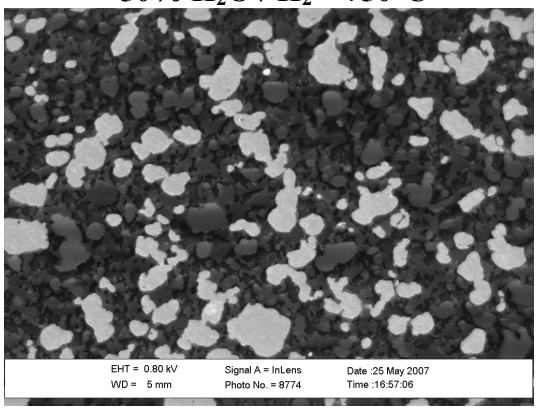

50% H_2O / H_2 – 1000°C

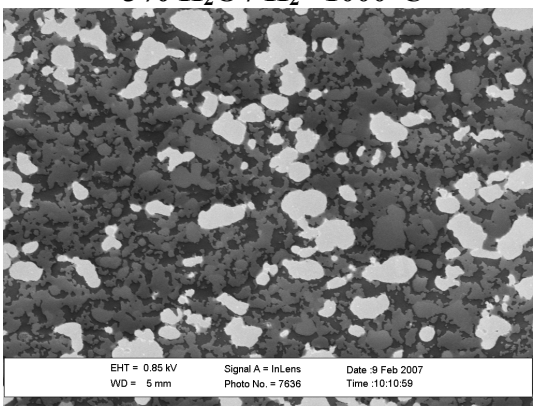

85% H_2O / H_2 – 1000°C

Figure 4-14. SEM-CC images from cross-sections of samples aged at different temperatures and in different atmospheres.

Results from the quantitative microstructural analyses of the SEM-CC images are summarized in Table 4-6, along with aging condition and the remaining conductivity after 300 hours. The results presented in Table 4-6 are elucidated below.

Table 4-6. Microstructural data from SEM-CC images including; aging temperature, aging atmosphere, remaining conductivity after 300 h, average Ni particle diameter, measured standard deviation, total number of measured Ni particles and percolating Ni area fraction. Diameters and standard deviations are normalized to the mean diameter of the two reference samples.

Sample ID	Aging T. / °C	Aging gas	σ_{300}/σ_0	Normalized diameter	Standard deviation	No. of Ni particles	Area fraction
1-C_1	1000	97-3	0.44	1.25	0.90	335	0.74
1-C_2			0.43	1.24		(47%)	0.70
1-F_1	1000	50-50	0.41	1.32	1.00	316-271	0.79
1-F_2			0.39	1.43		(44-38%)	0.77
1-G_1	1000	15-85	0.39*	1.33	0.99	296	0.75
1-G_2			0.39*	1.36		(41%)	0.75
1-H_1	750	97-3	0.97	1.06	0.81	621	1.00
1-H_2			0.96	1.10		(87%)	0.98
1-I_1*	750	50-50	0.94	1.15	0.84	518	0.92
1-I_2*			0.94	1.14		(73%)	0.93
1-Ref_1				1.00	0.77	714	1.05
1-Ref_2				0.99		(100%)	1.00

* Extrapolated values.

The confidence interval (95%) for the normalized average particle diameter varies between 0.03-0.07. In order to facilitate a comparison of the two techniques with regard to the particle spatial density, the number of particles given in the table is normalized to the same measured area as for the OM measurements. From the results presented in Table 4-6 it can be seen that the samples aged at 1000°C have larger average particle sizes and lower area fractions of percolating Ni compared to the samples aged at 750°C. This difference is also observed in the images presented in Figure 4-14. At 1000°C, the average particle size increase and the number of particles decrease when the H_2O concentration is increased from 3% to 50% and 85%. The two analyzed samples treated in 50% H_2O show slightly different conductivity losses, while the average particle size, spatial density and area fraction measured from OM images are very similar. However, the average particle size and spatial density measured from SEM-CC differs slightly between these two samples. The sample exhibiting a lower conductivity has larger and fewer number of percolating Ni particles.

It is reasonable to assume that the differences seen between the samples aged at 750°C are due to the different reduction procedures.

From plots of the particle size distributions from the SEM-CC images it can be seen that the aged samples have sizes significantly shifted towards larger particles and agglomerates. However, the difference between the samples aged in 50% and 85% H_2O is not as clear as in the size distributions collected from optical images.

In conformity with the area fractions measured in the optical images, a larger area must be measured in order to attain a sufficiently narrow confidence interval also for the SEM-CC images.

4.5 Discussion

The kinetics of Ni sintering and coarsening in the aged Ni-YSZ cermets are seen to be strongly influenced by temperature and H_2O concentration in the aging atmosphere. This is evident in the results both from electrical conductivity measurements and microstructural analyses. In terms of electrical conductivity, the effect of temperature was seen as a 10-20 times more severe degradation at 1000°C compared to 750°C. Thus, the degradation rate and total loss of electrical conductivity was considerably higher at 1000°C. At the same time, an initially higher degradation rate was seen at higher H_2O concentrations. Over time, however, the rate of degradation decreases and becomes lower than the corresponding degradation rates seen for samples aged under drier conditions. This effect of the H_2O concentration was observed both at 750°C and 1000°C. No effect was observed from the constant current load.

In terms of microstructural changes, the increase of Ni particle size and decrease in the number of particles that could be measured in OM images are also more significant at 1000°C. The samples aged at 750°C all exhibit a mean particle size in the same range as the reference samples. Even though all samples aged at 1000°C display a conductivity loss in the same range, the mean particle sizes and particle spatial densities differ significantly within these samples. At 1000°C, the samples were aged at three different H_2O concentrations. The average particle size measured in OM images increases with increasing H_2O concentration, and at the same time the number of particles decreases. This effect of the H_2O concentration at 1000°C is illustrated in Figure 4-15 below.

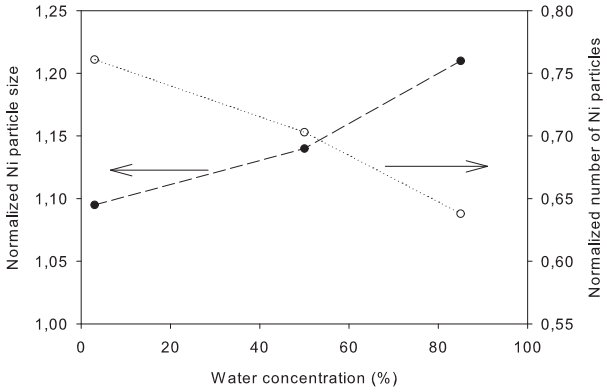

Figure 4-15. Average Ni particle size and number of Ni particles measured, as a function of H_2O concentration from aging at 1000°C. Both size and particle numbers are normalized to what was measured in the reference samples.

In this figure, the particle size and measured number of particles have been normalized to what was measured in the reference samples and plotted as a function of H_2O concentration. It can be seen that when the H_2O concentration is increased from 3 to 50% and from 3 to 85%, the particle size increases by 4 and 10%, respectively. At the same time, the particle spatial density measured in the optical images decrease with increasing H_2O concentration. In a figure such as the above, both the reference samples and the samples aged in 750°C would be at ~1.0 on both the right and the left hand scales. Thus, on this time scale no significant effect on the Ni coarsening from aging at 750°C for 300 hours can be seen.

It is well-known that metal atoms become considerably more mobile at the so-called Tamman temperature. The Tamman temperature is defined to be half the melting point in Kelvin. The melting and the Tamman temperatures for Ni are 1455°C and 591°C, respectively. Thus, at both 750°C and 1000°C some degree of atom mobility is expected for Ni. In combination with the overall driving force for surface energy reduction, the increased atom mobility is likely to result in Ni particle sintering and coarsening and a subsequent loss of contact points in the electrically conducting Ni-network. There is a number of possible mechanisms that can be involved in this particle sintering and coarsening of the Ni phase in the Ni-YSZ cermet. In Table 4-1, six mechanisms for which the driving force is neck formation between particles in contact, are summarized. The driving force for such diffusion will vanish as the neck formation proceeds. It might be reasonable to expect that neck formation is already completed after the three hours of reduction at 1000°C. However, the same

mechanisms will also be present when adjacent particles or agglomerates with different radius sinter. In this case, the driving force is the difference in particle sizes and the driving force will successively decrease as the smaller particles and agglomerates merge with the larger particles. In addition, Ni atoms may also have the ability to diffuse on the YSZ surface or to be transported via gas phase. It is reasonable to expect all the mentioned mechanisms to exhibit a higher rate of sintering directly after the samples are reduced and, when necks are filled up and the smallest particles are lost, the rate is decreased. This is due to a loss of the driving force for sintering when the radii of the Ni particles increase.

In this work, a higher degradation rate was observed at higher temperatures. This can be explained by the fact that all mechanisms for Ni mobility and diffusion take place at a higher rate at elevated temperatures. A higher degradation rate was also observed at higher H_2O concentrations. This is taken as a clear indication that the presence of H_2O enhances the Ni atom mobility. According to what was presented in section 4.2.4, due to the presence of H_2O, three separate types of Ni mobility can be considered. These are 1) Ni surface diffusion on Ni particles, 2) Ni surface diffusion on YSZ and 3) Ni transport via the gas phase. The reason to why the presence of an increased H_2O concentration should increase Ni transportation via these mechanisms can be explained by a formation of OH-bonded Ni dimers as described by J. Sehested et al. [67]. A. Gubner et al. [25] have presented thermodynamic calculations of the partial pressures of gaseous Ni species from 0.6 to 98.8 mol fraction of H_2O / H_2. They found $Ni(OH)_2$ to have the highest vapor pressure in a system of H_2, H_2O and Ni and that the vapor pressure was seen to increase as the H_2O / H_2 ratio was increased. The presented values are well in agreement to what has been calculated in this work by use of the software FactSage. In Figure 4-16, the calculated partial pressure of $Ni(OH)_2$ and Ni at 750°C and 1000°C are presented. In this figure it can be observed that, at a given H_2O concentration, the partial pressure of $Ni(OH)_2$ increases by more than 2 orders of magnitude when the temperature is increased from 750°C to 1000°C. At the same time, at a given temperature, the partial pressure of $Ni(OH)_2$ increases exponentially by more than 2 orders of magnitude from 3% to 50% H_2O and by 1 order of magnitude from 50% to 80% H_2O. Thus, in the present case, Ni(OH) species does exist in the system. Even though no measurable loss of Ni was observed in the studied samples, it is reasonable to assume that due to a higher vapor phase pressure,

the concentration of Ni-OH species increases at the Ni surface. It is also interesting to note that the partial pressure of Ni increases by 4 orders of magnitude as the temperature is increased from 750°C to 1000°C.

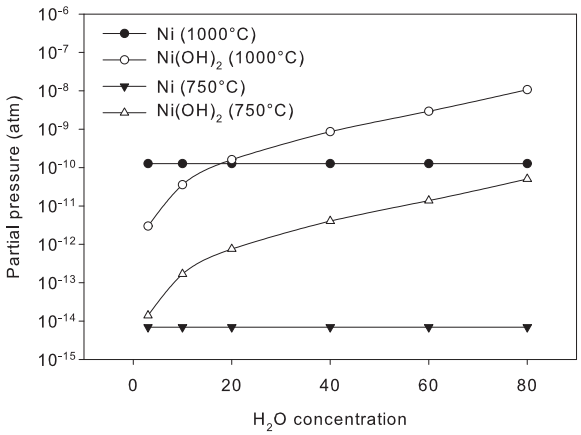

Figure 4-16. Partial pressure of Ni species in equilibrium with a H_2 / H_2O atmosphere over a Ni surface as a function of water concentration. Calculations were made by use of FactSage.

In this work, the particle size was observed to increase in samples aged in an atmosphere containing high concentrations of H_2O. For adjacent particles of different size, particle growth can be caused by surface diffusion of Ni atoms on the Ni particles alone. It is therefore likely that this mechanism is active and consequently, one of the reasons for the observed particle growth and conductivity loss under all the studied conditions. This model has been successfully applied in order to explain Ni particle coarsening by R. Vassen et al. [65]. In comparison to the effect of an increased temperature, the magnitude of the conductivity loss is only slightly correlated to the increased H_2O concentration and the average particle size. An increase of the particle size by 10%, 14% and 21% corresponds to a conductivity degradation of 57%, 60% and 61%, respectively. Compared to previous reported studies, the correlation between particle size and the absolute loss of conductivity found in this work is very weak. D. Simwonis et al. [43] report a 13.2-26.0% growth of Ni particles and a corresponding loss of conductivity of 10.3-33.3% after long-term aging at 1000°C in 3% H_2O / 4% H_2 / Ar.

If the particle size increases for a given volume fraction, the concept of contiguity predicts less percolation and lower conductivity. This prediction must be based on the assumption that similar sintering mechanism(s) are active in the studied material system. At lower H_2O concentrations, the dominating sintering mechanism in

Ni-YSZ cermets is generally identified as surface diffusion of Ni atoms on the Ni particles [65]. It is reasonable to assume that this type of surface diffusion increases in the presence of H_2O, as reported by J. Sehested et al. [67]. Accordingly, it can be concluded that the rate of conductivity degradation and the growth of Ni particles are controlled by surface diffusion on Ni particles. However, in this work the absolute loss of conductivity is not well correlated to the particle size at high concentrations of H_2O and hence, it is reasonable to expect that there is one or more additional active Ni diffusion route(s) at higher H_2O concentrations. The additional route(s) should contribute to particle coarsening but not as much to the loss of electrical conductivity. A possible mechanism yielding this effect can be Ostwald ripening by diffusion of Ni-OH species over the YSZ surface or / and vapor phase transport, from smaller non-percolating Ni particles to larger and percolating Ni particles. This is strengthened by the fact that the total spatial density of Ni particles measured in OM images decreases for the samples aged in higher H_2O concentrations, whereas the spatial density of percolating Ni is less affected. In this context it should be mentioned that if the anode structure is also used to achieve internal reforming of CH_4, the catalytic activity will only be dependent on the amount of available Ni surface. Thus, this type of coarsening, without any significant effect on conductivity, would be detrimental for internal reforming. Furthermore, a re-oxidation and volume expansion of Ni to NiO after considerable particle coarsening would result in a severe risk of crack formation on the YSZ network and the YSZ electrolyte.

In the conducted experiments, no effect was observed from aging the Ni-YSZ cermet under constant current load. The applied current density of 4.5 A/cm^2 is higher than what is encountered under cell operation.

Even if no conclusions can be drawn with regard to the effect on the microstructure from different H_2O concentrations at 750°C, it is interesting to note that the area fractions measured from SEM-CC images differ along with the absolute conductivity of these two samples. The absolute conductivities of ~455 and 360 S/cm correspond to the normalized area fractions of 0.99 and 0.93, respectively. Furthermore, from the samples aged at 1000°C it can be seen that a conductivity of ~200 S/cm corresponds to an area fraction of ~0.75. An aged anode support sample, similar to the ones presented here, showed a conductivity of ~115 S/cm and a

percolating Ni area fraction of 60%*. The observed relationship between the percolating Ni area fraction and conductivity is plotted in Figure 4-17.

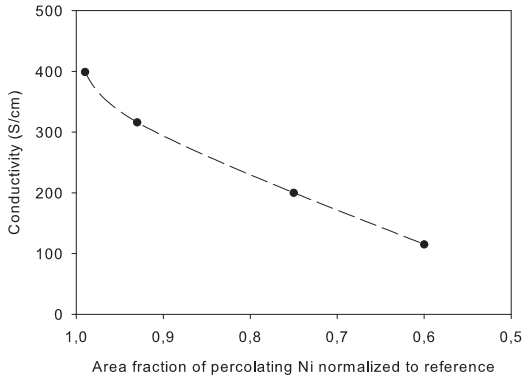

Figure 4-17. Conductivity at 1000ºC vs. area fraction of percolating Ni (conductivities measured at 750ºC are corrected to correspond to data measured at 1000ºC). The area fraction is normalized to the area fraction in the reference samples. The line is a smooth curve crossing the measured data points.

Part of the initial conductivity loss during the reduction can be related to the volume reduction during transformation of NiO to Ni. This effect is described by Minh et al. [1]. In this description it is assumed that the maximum conductivity is obtained when enough NiO has been reduced and formed a conducting Ni-metal matrix and that the abrupt initial drop corresponds to a loss of Ni particle contact as the particles shrink due to further reduction of the NiO. However, after 3 hours of reduction at 1000°C, the transformation of NiO to metallic Ni is expected to be completed. In [74] N. M. Tikekar et al. present results from experiments where pressed NiO-YSZ bars have been reduced and re-oxidized at different temperatures with the purpose of studying the reaction kinetics. The thickness of the reduced layer is given as a function of reduction time at different temperatures (600-800°C). It is concluded that the rate of reduction is increased by over an order of magnitude when the temperature is increased from 600°C to 800°C and at 800°C the reduction proceeds at a rate of 249μm/h. Considering the thickness of the samples in this study and the even higher reduction temperature, it is reasonable to expect full reduction in less than 3 hours. This is also confirmed by SEM analyses of the reduced reference samples used in this study, where no NiO was found present.

* The data was acquired from additionally performed experiments which have not been presented in this thesis.

4.6 Conclusions

High temperature aging experiments of model Ni-YSZ anode supports show that Ni sintering and coarsening are significantly affected not only by the temperature, but also by the H_2O concentration in the aging atmosphere. It is suggested that the presence of H_2O facilitates Ni surface diffusion via OH-bonded complexes, which has been reported in the context of Ni steam-reforming catalysts. The result of an increased surface mobility of Ni is seen as significantly larger average Ni particle sizes in samples aged in the presence of high H_2O concentrations.

In the studied samples, the increased Ni particle size at high H_2O concentrations is not well correlated to the decrease in conductivity of the cermets. In the studied time scale it is therefore proposed that the recorded conductivity loss is mainly due to the surface diffusion on Ni particles driven by the size difference between adjacent Ni particles. Particle coarsening with a weaker correlation to conductivity the loss is observed at higher H_2O concentrations. It is proposed that the presence of H_2O facilitates Ni diffusion and coarsening that has a less detrimental effect on the Ni percolation. The proposed routes are surface diffusion on the YSZ surface and vapor phase transportation of volatile OH-bonded Ni species. Based on this observation it can also be concluded that electrical conductivity measurements do not describe the full process of microstructural rearrangements within the Ni phase in the presence of high H_2O concentrations.

No effect was observed from aging the Ni-YSZ cermet under constant current load of 4.5 A/cm^2.

The charge contrast in FE-SEM is a useful technique for studying the Ni phase percolation microscopically. As illustrated in Figure 4-17, this technique can also be used in order to correlate the area fraction of percolating Ni in the cermet to the electrical conductivity.

5 Aging of long-term tested cells

5.1 Introduction and background

In this chapter, a cell that has been tested for 2 years (17,500 hours) is analyzed with regard to microstructural changes in the anode and at the interface between anode and electrolyte. Recorded electrochemical data, I-V curves and impedance spectra, have been used in order to describe how the performance of the cell changed over the operation period. Since the microstructural analysis only focuses on the anode, a conclusive correlation between performance and microstructure is not expected. In order to facilitate such correlations the cathode must also be considered and the study should preferably be based on more than one cell. However, this kind of long-term tested cells is relatively rare and the microstructural analysis of this cell should be considered a case-study. The definition of "long-term" concerning cell operation is relative, but the commercial requirement for SOFC systems is often considered to be in the order of 40,000-50,000 hours. In this period of time, the degradation rate must be very low in order to make such systems attractive on a wider market [23]. It is therefore necessary to gain an understanding of the degradation mechanisms for every component included in the SOFC system.

The studied cell had been continuously operated for less than half of the time set to be the commercially required life-time. The cell will in the following be referred to as DK-34. The operating conditions for DK-34 can be regarded as relatively severe with regard to the anode. The cell was operated at a temperature of 850°C and an initial constant current density of 1 A/cm^2. Under these operation conditions, cells tested for significantly shorter time have been reported to show microstructural changes in the Ni-YSZ anode. The predominant change is coarsening of the Ni phase, which can be seen even at the lower operation temperature of 750°C [7].

To put the microstructural analysis of the DK-34 cell into perspective, three different anode samples are used for comparison. The first is a reference sample where the anode was reduced by the same procedure as DK-34, but no electrochemical testing was performed. The two additional samples have been

operated at the same temperature and fuel utilization as DK-34, but with different current densities (0.25 and 1.93 A/cm^2) and for 1,500 hours only.

In the following the operation history of DK-34 is summarized and a few data from electrochemical measurements are presented as a background to the microstructural analysis. Further, the results from the microstructural analysis are presented, discussed and correlated to the reference sample that was only reduced. Finally, results from the microstructural analysis of the cells tested for 1,500 hours are presented and compared to DK-34.

5.2 Cell tested for 17,500 hours

In Figure 5-1 a plot of the cell voltage vs. operating time for DK-34 is shown. A number of incidents affecting the cell voltage during operation are indicated in the figure. The incidents are listed and described below.

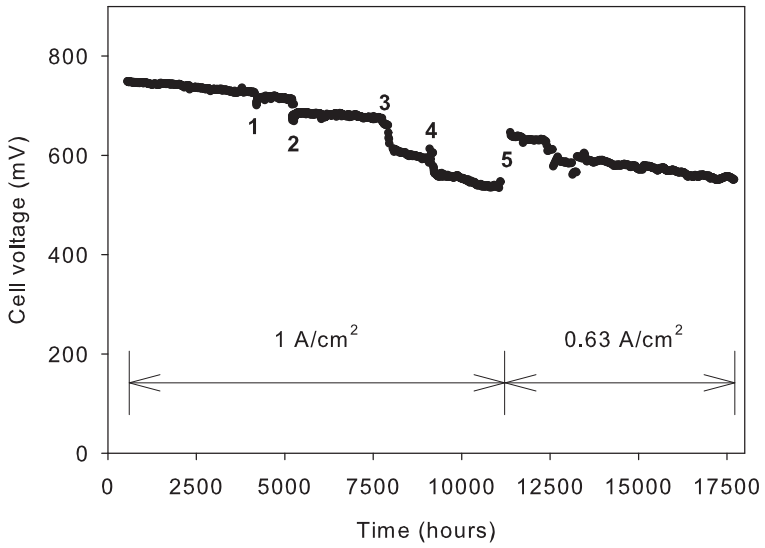

Figure 5-1. Cell voltage vs. time for DK-34. Numbers are indicating specific incidents affecting the cell voltage degradation.

1) After ~4,200 hours a power failure caused a shut down of the air supply to the cathode. The incident resulted in a cell voltage drop from 730 to 715 mV.

2) After ~5,200 hours the cell was subjected to an accidental thermal cycle, where the temperature dropped 700°C before it was increased to 850°C again after 3 hours. This incident resulted in a cell voltage drop from 715 to 680 mV.

3-4) I-V curves were recorded at operating conditions and at OCV (after 8,000 and 9,200 hours). During these procedures, the cell voltage dropped from 660 to 613 mV and from 600 to 560 mV, respectively. The large drop, marked 3, occurred when

the gas supply shifted to "safety mode" during a power failure. In safety mode the fuel gas is automatically shifted from operating gas to humidified diluted hydrogen (9% H_2 in N_2) and the cell was set to OCV. The exact cause of the voltage drop is not known, but generally the cell is seen to be more sensitive towards gas fluctuations later in the operation period. Incidents 3 and 4 seamed to increase the degradation rate somewhat.

5) Due to a gas leak, the pO_2 in the outgoing fuel gas increased over time. Due to the fact that the cell voltage was still relatively high indicates that the leak arose close to the fuel gas outlet. In order to compensate for this leak, the current density was reduced from 1.00 to 0.63A/cm^2 while the gas flows were kept constant. By this adjustment the cell was still operated at ~80% fuel utilization, with the gas leak taken into account.

During the 17,500 hours of testing, a number of impedance spectra were recorded. In Figure 5-2, Nyquist plots of selected impedance data acquired at 850°C spanning over the time of the cell test are shown. All impedance spectra shown here were recorded with air on the cathode and 20% H_2O / H_2 on the anode. Due to the assumed gas leak it is likely that the ratio between H_2O and H_2 have been altered over time despite the set fuel gas mixture.

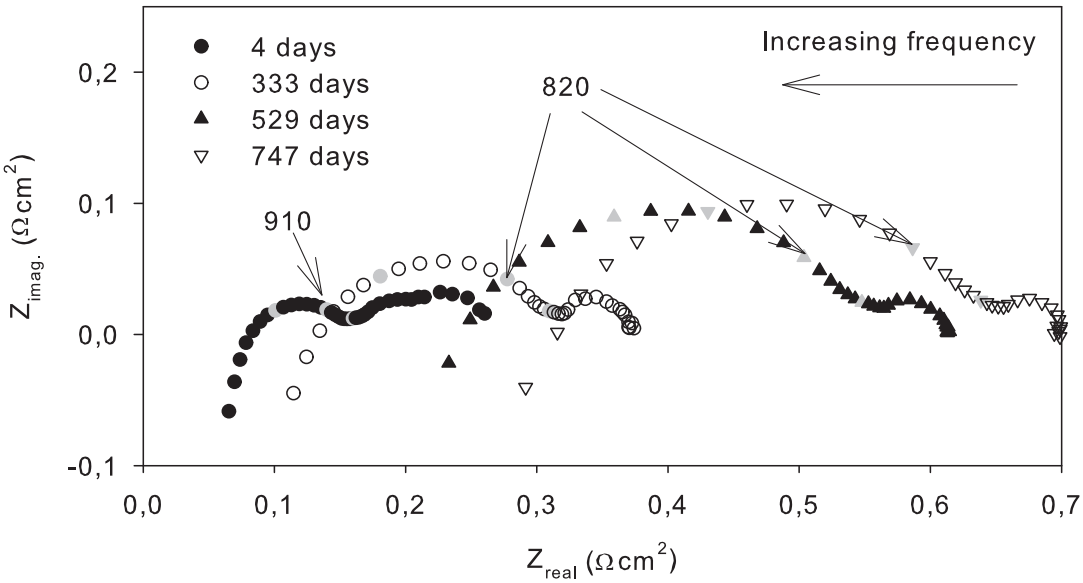

Figure 5-2. Nyquist plot of the impedance of DK-34 at different times during the testing obtained at 850°C. Fuel gas composition is 84% H_2 -16% H_2O. Each plot is named from the number of days the cell test has proceeded when the impedance data was acquired. Symbols in grey mark each decade in the spectra.

Directly from the Nyqvist plot above it can be seen that the ohmic resistance (R_s) and the polarization resistance (R_p) increase significantly over time. In Figure 5-3, Bode plots of the real and imaginary part of the same impedance are shown. The Bode plot of the imaginary part of the impedance gives an indication of a gas leak in the spectra after 529 and 747 days. This can be seen in the lower frequency range, where the response decreases over time. At ~3 Hz, a response that is sensitive to pH_2O / pH_2 have been reported and ascribed to diffusion and gas conversion at the anode [41]. Thus, this response can be expected to decrease if pH_2O is slightly increased due to a gas leak of air into the anode compartment. The change is most significant between the spectra after 333 and 529 days and it is assumed that the leak arose after the third incident listed above. After this incident the cell also showed signs of active cell area loss. The data presented in Figure 5-3, and in the following, are corrected for an active cell area loss of 2.5 cm^2. The size of the area loss was estimated from macroscopic inspection of the cell after testing as presented below.

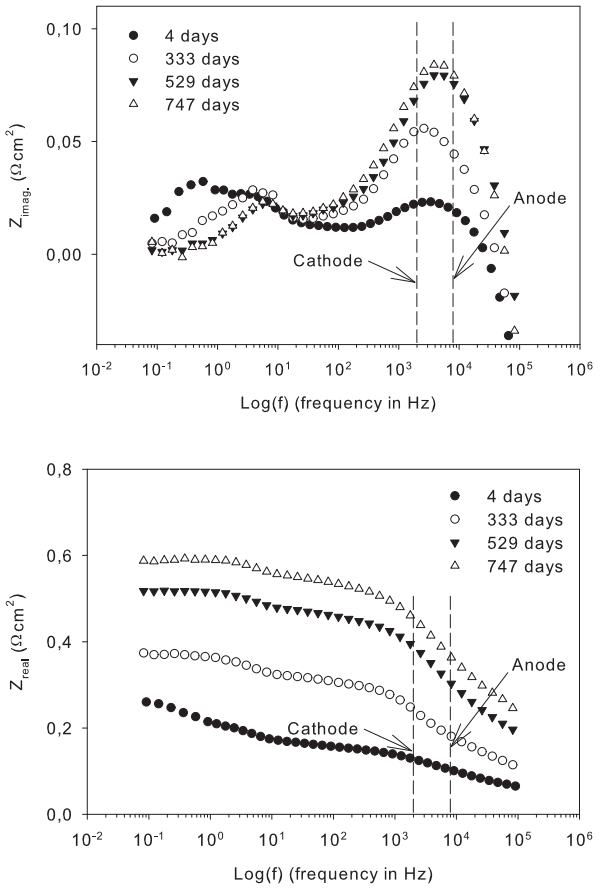

Figure 5-3. Bode plots of the imaginary (top) and real impedance (below) of DK-34 at different times during the testing obtained at 850°C. The fuel gas composition was 20% H_2O / H_2. Each plot is named after the number of days the cell test had proceeded when the impedance data was acquired. The plots are corrected for an area loss of 2.5 cm^2.

Also in these Bode plots it is clear that the ohmic resistance and the polarization resistance increase over time. By use of the Bode plot it is convenient to see in what frequency range changes occur. Typical frequencies for the cathode and anode responses [41] are indicated as vertical dashed lines in Figure 5-3. From the plots it can be seen that major changes occur in these regions. However, based on the presented impedance spectra obtained at 850°C it is not possible to distinguish unambiguously between anode and cathode degradations.

From the acquired I-V curves the ASR_{cor} could be calculated. Furthermore, the ohmic resistance, R_s, was extracted from the acquired impedance spectra. In Figure 5-4, the ASR_{cor} and R_s are plotted together with cell voltage vs. time.

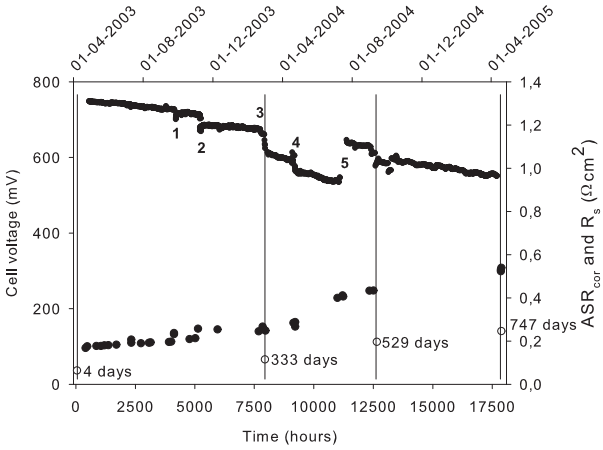

Figure 5-4. Cell voltage (line), ASR_{cor} (filled circles) and R_s (circles) vs. time of operation. The vertical lines indicate when the above presented impedance spectra were acquired.

From the presented electrical measurements it is evident that the cell performance is affected by the two years of testing. The cell voltage drops relatively linearly over the first 8,000 hours, except for the instant drop due to the unintentional thermal cycle (850-700-850°C). Over this time period both the ASR and R_s values increase with a lower rate than what is seen later on. Within the first 4,000 hours a degradation rate of ~6 mV per 1,000 hours is measured, which is less then 1% per 1000 hours. In the same time interval, R_s and ASR increase ~10% and 6% per 1,000 hours, respectively. After 8,000 hours the slope of the cell voltage curve changes, which to some degree is believed to be due to the gas leakage. Over the last 4,000 hours of operation, the cell voltage degrades by 10 mV per 1,000 hours. In Table 5-1 the cell voltage, ASR_{cor} and R_s are given at times where I-V curves and impedance spectra, yielding ASR_{cor} and R_s respectively, were acquired. In the right column, the

ratio between R_s and ASR is given. R_s is defined to be the serial ohmic resistance, while ASR is a measure of the cell resistance during current load. Thus, ASR includes not only the serial resistance but also the cell polarization resistances (see Figure 1-2). It can be seen that from 4 to 333 days, the ratio is changed from 0.39 to 0.46, which shows that R_s increased more in relation to ASR. However, from the later measurements the ratio between R_s and ASR remains constant. R_s and ASR are both related to the active cell area, which means that any degradation causing a loss of the total active cell area would result in a constant ratio between R_s and ASR.

Table 5-1. Cell voltage, ASR_{cor} and R_s extracted from Figure 5-4.

Time after reduction (days)	Cell voltage (mV)	ASR_{cor} (Ωcm^2)	R_s (Ωcm^2)	R_s/ASR_{cor}
4	750	0.17	0.067	0.39
333	660	0.25	0.115	0.46
529	590*	0.43	0.197	0.46
747	550*	0.53	0.246	0.46

* Cell voltage at lower current density than the previous measurements.

5.2.1 Sample description and preparation

In Figure 5-5 (left), an image of the DK-34 cell taken before it was tested, can be found. The cell is shown with the cathode (black) side on top. The dimensions of the whole cell is 5×5 cm, while the cathode cover an area of 4×4 cm. The outer parts consist only of anode support, anode and electrolyte. The green color is due to the NiO present. In a reduced state, Ni-YSZ is grey. Thus, the color of the cermet can be used as a macroscopic indication for distinguishing between NiO-YSZ and Ni-YSZ.

The image to the right shows the same cell after the two years of testing. At this point the cell was quite well sintered to the glass ceramic seals and to the alumina test-house. The green pieces are oxidized anode from the outer parts of the cell, but slight oxidation within the active cell area in the two corners closest to the gas outlet was also seen. At these positions the cell was very fragile. One or both of the corners are believed to be the reason for the leakage of gas as assumed in connection to the electrochemical measurements. As mentioned before, the active cell area with clearly visible oxidation and mechanical damage was estimated to be ~2.5 cm^2.

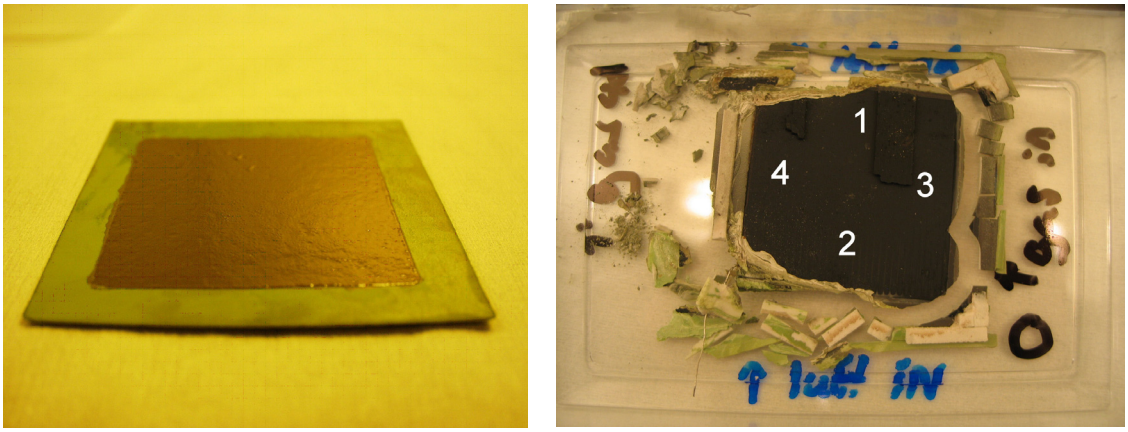

Figure 5-5. Images of the DK-34 cell before (left) and after test (right). Numbers indicate where samples for microstructural analysis were taken.

Four sample pieces of the cell (0.5×0.5 cm) were cut by a diamond saw, mounted into epoxy resin and cross sections were prepared as described in Chapter 2. The sample pieces were taken as indicated by numbers 1-4 in Figure 5-5. The sample pieces will in the following be referred to as sample 1-4, corresponding to the position on the cell. Sample 1 and 2 are from the upstream and downstream of the cathode gas, respectively. Sample 3 and 4 are from the upstream and downstream of the anode gas, respectively. All sample pieces were studied by SEM. In addition sample 3 and 4 were studied by optical microscopy and SEM-CC and analyzed with regard to Ni particle size and percolating Ni. SEM and X-EDS were used in order to search for any agglomerates of impurities close to the anode / electrolyte interface.

5.2.2 General microstructural overview

In Figure 5-6, selected SEM images from each of the positions marked out in Figure 5-5 and a reference sample are shown. The images illustrate cross sections of the interface between the anode (top) and the electrolyte (bottom). The Ni and YSZ phases are indicated in the top left image. From a comparison by eye it is possible to see that the Ni particles are significantly less dispersed and seen in larger agglomerates after test. Ni is even seen to surround YSZ particles at some positions, mainly close to the electrolyte interface, which is not seen in the reference sample. At the same time, pores without any presence of Ni are seen more frequently in the YSZ network. From a qualitative impression, and in comparison to the reference, significant Ni coarsening has taken place at all positions in the tested cell. However, a general impression is that less severe sintering has occurred in sample 3 in comparison to the other positions.

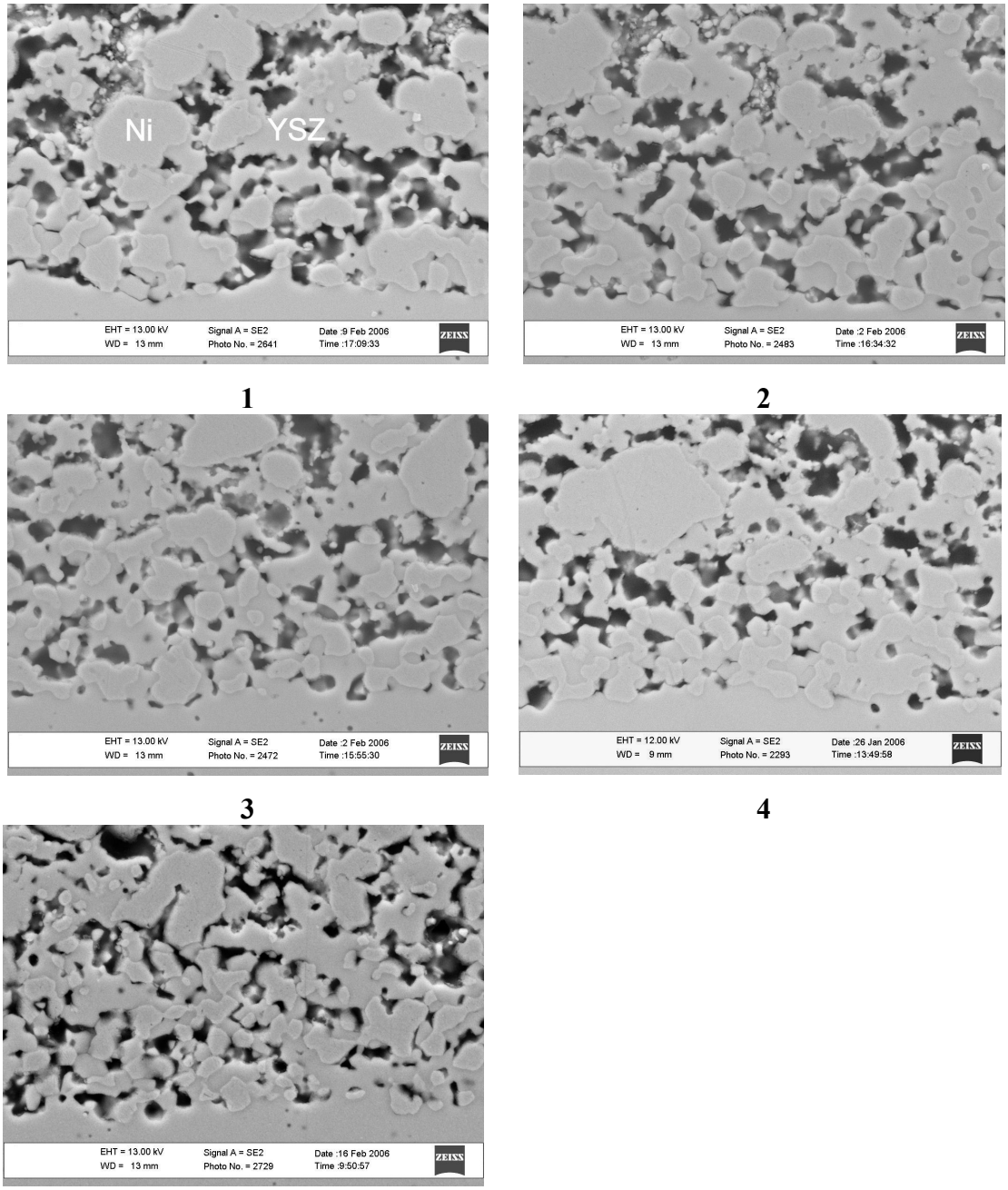

Figure 5-6. Selected secondary electron images from sample 1, 2, 3, 4 and reference. The cross sections show the interface between anode and electrolyte, where the dense structure below is the electrolyte. In the top left image Ni and YSZ are indicated.

Another significant detail is seen in the samples from position 1, 2 and 4, positioned farthest away from the fuel gas inlet. The images from these samples show crack formation between the anode YSZ and the electrolyte YSZ. Significantly less cracks are seen in the anode YSZ network close to the electrolyte interface (up to a few μm from the electrolyte), while no cracks are seen in the YSZ network further into the anode or anode support. At the cracks, YSZ in the anode and electrolyte is

seen to be separated by up to 300 nm. On the other hand, the Ni particles are most often still in contact both with the anode and the electrolyte YSZ, even close to where YSZ is seen to be separated. The fact that Ni particles are still in contact to the electrolyte, even where YSZ is separated, is taken as an indication that the crack formation is not due to sample preparation or the cooling of the cell to RT. Ni is a softer material than YSZ and, thus, it could be smeared out by the sample polishing and fill the cracks. However, based on the shape of the Ni particles close to the cracks this is not believed to be the case. In sample 3, from the position closest to the fuel gas inlet, and in the reference sample, no similar cracks are found in the inspected sample cross sections. Still, in sample 1, 2 and 4 more than 50% of the expected YSZ contact points are weakened or lost due to cracks. The crack formation is most severe in sample 1, where Ni particles at a few points are seen to be separated from the electrolyte.

The electrolyte was found to be intact and without any internal cracks throughout all the inspected sample cross sections.

In Figure 5-7, selected SEM-CC images from position 3, 4 and the reference sample are shown. The images show cross sections of the interface between the anode and the electrolyte (it should be noted that the sample cross sections in this figure are shown upside-down in comparison to Figure 5-6). In these images, percolating Ni appears bright whereas non-percolating Ni and the non-conducting phases appear dark.

The degree of percolating Ni is significantly reduced in the tested samples, when compared to the reference sample. Hence, a significant loss of Ni particle interconnectivity is seen. However, the Ni particles in the anode closest to the electrolyte have a higher degree of percolation when compared to Ni particles 4-10 μm into the anode and in the anode support. Furthermore, the percolated Ni close to the electrolyte in the tested cell is to a higher extent represented by large agglomerates in comparison to the reference cell.

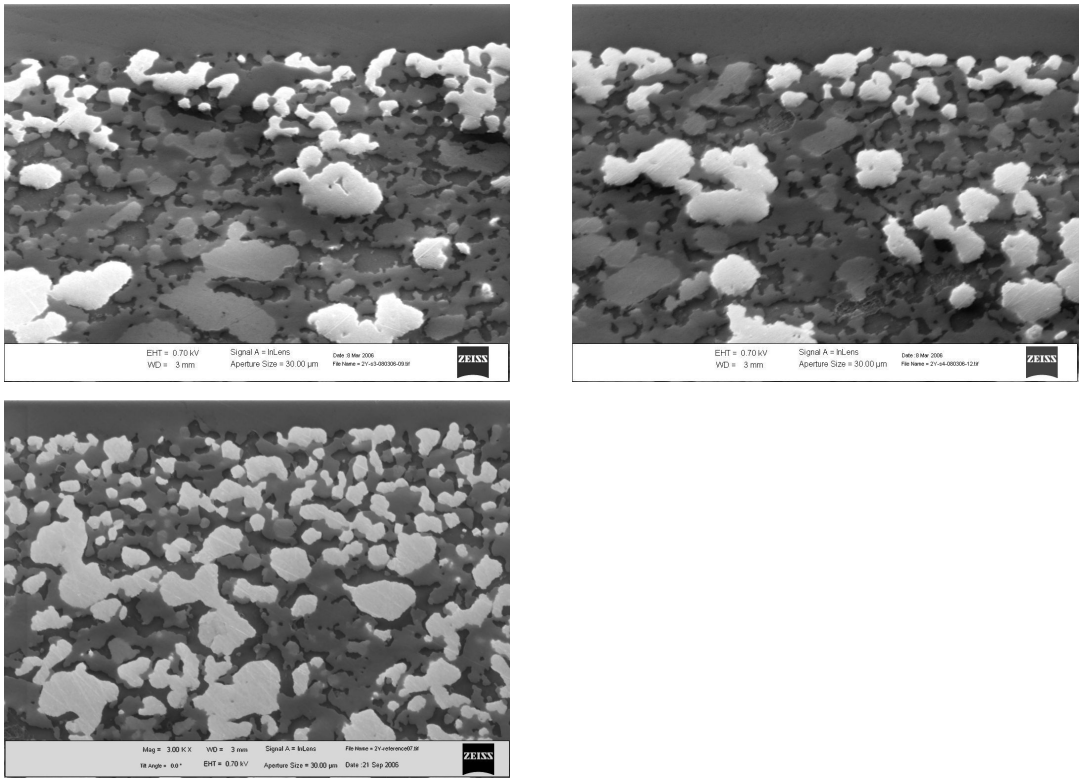

Figure 5-7. SEM-CC images of sample 3 (top left), 4 (top right) and reference (bottom). Only percolating Ni appears bright. N.B. In comparison to images in Figure 5-6 the sample cross sections are upside-down in these images.

From images similar to those above, the coverage of percolating Ni closest to the electrolyte was measured in sample 3, 4 and the reference. On a single line along the anode / electrolyte interface (390 µm in total) the length of each interface represented by contact between percolating Ni and electrolyte was measured and the number of contact lines was counted. Assuming that fuel gas only has access to the vicinity of each contact line, the triple phase points can be roughly quantified as twice the number of segments on the measured line. The results of these measurements are presented in Table 5-2.

Close to 50% of the interface line was covered by percolating Ni in contact to the electrolyte in all three samples. However, in the reference sample this coverage was distributed over 132 segments, while in sample 3 and 4 the coverage was divided over only 92 and 73 segments, respectively. Thus, the degree of interface length between percolating Ni and electrolyte is approximately the same in these samples. Only the vicinity of each contact, the so called triple phase points, can be assumed to facilitate electrochemically active sites. In sample 3 and 4, the number of triple phase points is estimated to be 70% and 55%, respectively, of what was found in the reference. This method of quantifying the number of triple phase points is, however,

believed to underestimate the effect of the Ni coarsening. Since the Ni particles are significantly larger in the tested anode, it can also be assumed that the passage for the fuel gas through the pores at the vicinity of the Ni particles is significantly narrowed. This would lead to an even lower amount of triple phase points in the tested samples.

Table 5-2. The coverage (column 2) and number of segments of percolating Ni along the interface line between anode and electrolyte (column 3). Column 4 is the assumed maximum number of triple phase points along the line.

Sample ID	Line coverage	No. of segments	Triple phase points
3	0.58	92	184
4	0.50	73	146
Reference	0.50	132	264

A higher probability of percolation in the anode, in comparison to the anode support, becomes evident when studying images collected in the middle of the anode support. The degree of Ni percolation in the anode support is shown in Figure 5-8. In the anode support, areas with the length of 30-40 μm parallel to the electrolyte are frequently found without percolated Ni.

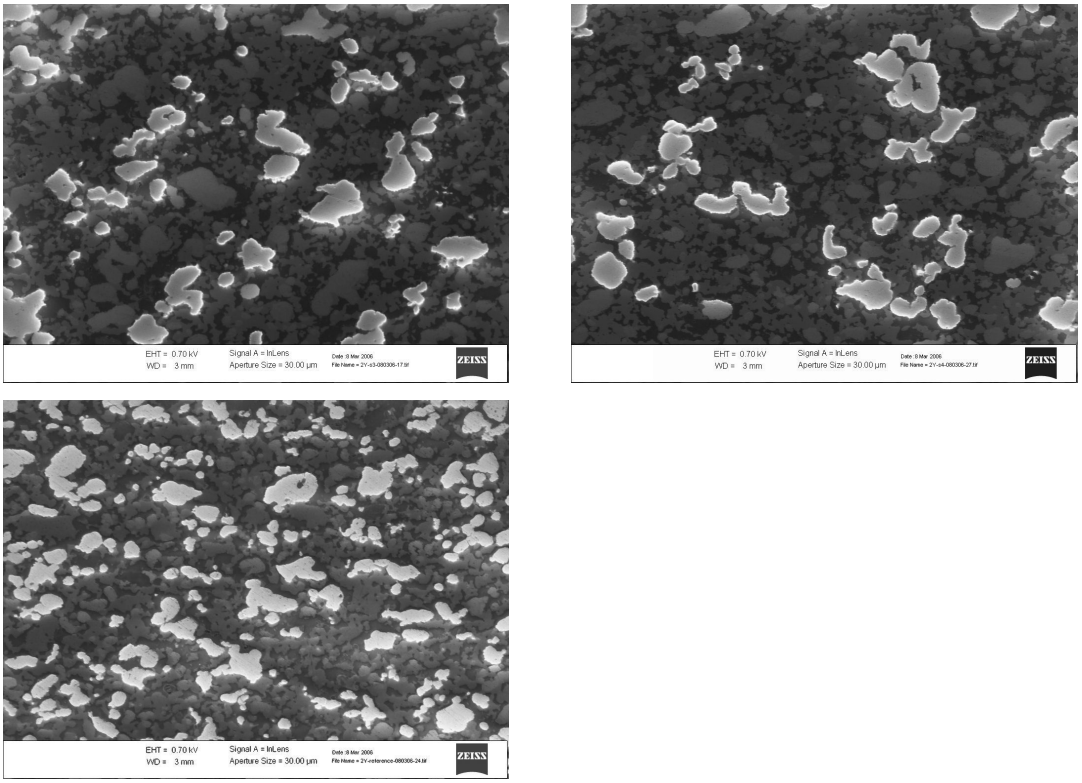

Figure 5-8. SEM-CC images from the middle of the anode support of sample 3 (top left), 4 (top right) and reference (bottom). Percolating Ni is visualized.

A more quantitative approach towards the microstructure is presented in the following section.

5.2.3 Ni particle coarsening

The Ni particle size in the anode close to the electrolyte and in the middle of the anode support was analyzed in samples 3, 4 and the reference. Measurements were performed in 20 optical images acquired at the anode / electrolyte interface and 11 images acquired from the middle of the anode support. The total area measured for the anode and the anode support is 0.007 mm^2 and 0.024 mm^2, respectively.

Data from measurements performed on the anode are presented in Table 5-3. The data from measured Ni particle sizes confirms the impression gathered from the SEM images presented above, i.e. that Ni particles are smallest in the reference sample. Further, the average Ni particle size is ~17% larger in sample 4 compared to sample 3. At the same time as the average particle size increases, the standard deviation also increases and the number of measured particles is significantly reduced. No difference in area fraction can be seen from the presented data.

Table 5-3. Particle size and area fraction measured in optical images from the anode of sample 3, 4 and the reference. Particle sizes and area fractions, as well as the given standard deviations, are normalized to the particle size and area fraction of the reference.

Sample ID	Normalized diameter	Standard deviation	Number of Ni particles	Normalized area fraction
3	1.24	0.96	898 (64%)	1.00 ±0.06
4	1.45	1.14	641 (46%)	1.00 ±0.06
Reference	1.00	0.73	1398 (100%)	1.00 ±0.07

Data from measurements performed on the anode support are presented in Table 5-4. Here it can be seen that the average Ni particle size do no differ significantly between the different samples. However, the number of measured particles is less in the tested samples compared to the reference.

Table 5-4. Particle size and area fraction measured in optical images from the anode support of sample 3, 4 and the reference. Particle sizes and area fractions, as well as the given standard deviations, are normalized to the particle size and area fraction of the reference.

Sample ID	Normalized diameter	Standard deviation	Number of Ni particles	Normalized area fraction
3	1.00	0.92	1693 (83%)	0.93 ±0.08
4	1.04	0.98	1560 (77%)	0.98 ±0.08
Reference	1.00	0.91	2035 (100%)	1.00 ±0.08

The measurements of the Ni area fraction in the anode support, as well as the anode, are afflicted with a wide confidence interval. This is due to the variance between the measured images, i.e. the variance of Ni area fraction over the sample cross sections. In order to acquire a higher confidence in these measurements, a larger area must be analyzed.

From the SEM-CC images in Figure 5-7 and Figure 5-8, a significant loss of percolating Ni can be seen in the samples from the tested cell. The particle size of the percolating Ni particles is also larger in the tested samples. This is confirmed by the data from image analysis presented in Table 5-5 below. The relative increase of the percolating Ni diameter is consistent to what was measured in optical images, where all Ni is taken into account. When the area fraction of percolating Ni was measured in the anode, an area loss was found relative to the reference sample. From the images in Figure 5-7 it is clear that the majority of this loss is found at a distance of a few micrometers from the electrolyte interface and not closest to the electrolyte.

Table 5-5. Particle size and area fraction of percolating Ni measured in the anode of samples 3, 4 and the reference. Particle sizes and area fractions, as well as the given standard deviations, are normalized to the particle size or area fraction of the reference.

Sample ID	Normalized diameter	Standard deviation	Number of Ni particles	Area fraction
3	1.29	0.95	278 (48%)	0.88 ±0.09
4	1.48	1.07	195 (34%)	0.81 ±0.09
Reference	1.00	0.62	577 (100%)	1.00 ±0.07

Due to a considerable intensity variation across the particles in SEM-CC images acquired from the anode support, it was difficult to perform image segmentation without getting significant noise in the resulting binary images. The

noise made it impossible to accurately measure the particle size of the percolating Ni. However, the area fraction is not expected to be as affected by this noise and the percolation in the samples 3 and 4 is found to be ~60% of what is measured in the reference sample. From the images it is also clear that the majority of the percolation occurs in the largest existing particles and agglomerates after testing.

5.2.4 Chemical analysis by X-EDS

As mentioned in Chapter 1, a segregation of impurities to the YSZ surface is reported to be a potential problem during cell operation. The effect of impurity segregation could be blockage of transport paths or reaction sites. Generally, the impurity phase is expected to be only a few nanometers thick. Since the diameter of the interaction volume for X-rays are generally up to a micrometer such thin layers are not possible to detect by using SEM and X-EDS. However, reports from microstructural analyses of solid oxide cells that have been operated in electrolysis mode demonstrate an agglomeration of impurity phases in the Ni-YSZ electrode close to the electrolyte interface, followed by a significant reversible passivation of the electrode performance [75]. These agglomerations consist mainly of SiO_2 and are large enough to be detected by SEM and X-EDS.

Even though numerous X-EDS point-analyzes and mappings were performed, no presence of SiO_2 containing phases could be detected in the DK-34 cell. The analysis was mainly concentrated to the anode close to the electrolyte, since this is were the most detrimental effect of such segregations should be expected. However, also the outer parts of the anode and the anode support were analyzed. The fact that no SiO_2-containing phases were found is taken as an indication that significant agglomeration of such impurity phases, as reported by A. Hauch et al. [75], is not present after the cell test. However, the presence of thin layers of impurities can not be excluded due to the low resolution of the utilized analysis technique.

From X-EDS analysis in the middle of the YSZ electrolyte, the presence of both Ni and Mn was detected and quantified to be ~2 wt-% and ~0.3 wt-%, respectively.

5.2.5 Discussion

The presented data from the electrochemical characterization show a significant degradation of the overall cell performance. The total effect of this degradation is seen as a decrease in the cell voltage and at the same time increasing

ohmic and polarization resistances. It seems reasonable to ascribe the step wise increase in R_s and ASR, observed in connection to "incident 3" to a loss of active cell area. The correction of the assumed cell area loss yields a remaining 84% of the cell area at the end of the cell test. The measured degradation is not possible to ascribe to any specific processes.

The reason for the cracks seen in the YSZ at the anode / electrolyte interface is difficult to allocate. However, it is reasonable to assume that the interface is subjected to some degree of thermally induced stress. Due to a disruption of the fuel gas supply, the coarsened Ni phase might have been partially oxidized. The coarsened Ni phase could be expected to have less space to expand and might therefore apply a pressure on the YSZ phase. The highest degree of Ni coarsening is seen close to the electrolyte interface, thus a possible volume expansion of Ni to NiO could be expected to be most severe at this interface.

Moreover, the parts of the cell that have been outside the sealing materials were green from oxidized Ni. At the sealing and further into the cell compartment the color changes from green to grey. This means that, close to the sealing, there is a boarder-line between NiO and Ni. It is reasonable to assume that if the pO_2 of the fuel gas is increased, this boarder-line will be slightly shifted towards the cell center, and vice versa. Thus, from fluctuations in the fuel gas composition, the boarder between NiO and Ni will move back and forth, creating a site in the anode where numerous "redox cycles" occur over time. These redox sites can especially be expected at positions in anode compartment where the fuel gas composition varies over time, from e.g. variations in fuel utilization. Repeated reductions and oxidations of Ni-YSZ anodes have been proven to be detrimental to the YSZ structure [30,31]. Assuming that crack formation occurs close to the sealing, preferentially close to the gas outlet where pO_2 varies the most, these cracks can later propagate towards the center of the cell area. The crack propagation could later on be driven by thermally induced stress.

The cracks seen between YSZ in the anode and the electrolyte will affect the transportation of oxygen ions from the electrolyte further into the anode. However, Ni particles are still seen to be in contact with the electrolyte and at the same time these particles have a relatively high probability for percolation. It is therefore not possible to conclude that the YSZ separation has in fact a significant effect on the available TPBs. On the other hand, it can be concluded that the cracks limit the possibility for finding active TPBs at any distance from the electrolyte since the conduction path for

oxygen ions are cut off by the cracks. Furthermore, the observed cracks will most certainly also weaken the interface mechanically and increase the risk for anode / electrolyte delamination.

A significant coarsening of Ni was observed for the samples taken both upstream and downstream along the fuel gas flow. However, the average Ni particle size measured at the gas outlet was 17% larger than at the inlet and at the same time there were fewer particles present in the studied area. At the fuel gas inlet, the H_2O concentration was set to ~20%. With a fuel utilization of 80%, the fuel gas composition will be gradually shifted towards higher concentrations of H_2O. The concentration of H_2O in the fuel gas outlet is at these conditions expected to be ~65%. To the author's knowledge, the effect of H_2O concentration on the Ni sintering behavior in Ni-YSZ cermets is not very well known. However, research on Ni steam reforming catalysts has established the fact that the Ni mobility increases in the presence of H_2O. This effect of water is also seen in the results presented in Chapter 4 of this work. It is therefore reasonable to assume that the concentration gradient of H_2O in the fuel gas results in different sintering conditions for Ni along the gas flow path. The higher concentration of H_2O close to the fuel gas outlet results in a higher mobility of Ni atoms and hence, in a more severe Ni coarsening. It is also reasonable to assume that the H_2O concentration is highest close to the anode / electrolyte interface, where H_2 is consumed and H_2O is produced. This might be a possible reason for the more severe coarsening of Ni seen at the electrolyte interface compared to the anode support. However, this interface is also polarized during operation which might affect the chemical properties of the material surfaces at the TPBs.

Due to the Ni particle coarsening at the anode / electrolyte interface, a significant loss of Ni surface area and TPBs must be expected. From SEM-CC images the number of active triple phase points was measured for sample 3, 4 and the reference sample. These values are presented in Table 5-2. Assuming that the measured length of each segment represents the diameter of the contact area that each Ni particle has to the electrolyte and that particles are evenly distributed in all directions over the electrolyte interface area, a TPB length per cell area can be estimated. The number of contact points along a line is known and can be converted into the number of contacts in the plane, as the square of the number of contact points along the line. The size of the plane is the square of the total line length. Thus, we

know the number and diameter of the contact points and the size of the plane, hence, the TPB length per area can be calculated as shown in **(5-1)**.

$$TPB_{length} = \frac{\text{Linelength} \cdot \text{linecoverage} \cdot \pi \cdot \text{Number of segr}}{\text{Number of segments} \cdot \text{Linelength}^2} \quad \textbf{(5-1)}$$

In Table 5-6, the resulting TPB lengths for sample 3, 4 and the reference sample are given. Based on the assumptions made for these calculations, the TPB length at the interface between the anode and electrolyte is found to be 78% and 55%, respectively, of the TPB length calculated for the reference sample. For cells similar to the one examined in this work the specific polarization resistance of the anode has been estimated to be in the range of 0.05 Ωcm^2 [40]. Assuming that this resistance corresponds to what the reference sample should have and that the anode resistance is solely dependent on the measured TPB lengths, the calculated area specific TPB lengths can be used to calculate an expected specific anode resistance for the tested samples. The calculated values are presented in the third column of Table 5-6.

Table 5-6. Calculated TPB length in the interface plane between anode and electrolyte, based on SEM-CC images and specific anode resistance (R_{anode}) [40].

Sample ID	TPB length (m/cm^2)	R_{anode} (Ωcm^2)
3	43 (78%)	0.06 (120%)
4	29 (55%)	0.09 (180%)
Reference	53 (100%)	0.05 (100%)

Assuming that the resistance is depending on the available TPB length, the calculated specific anode resistance of DK-34 should be between 0.06 and 0.09 Ωcm^2. The ASR for DK-34 measured before and after of testing was 0.17 and 0.53 Ωcm^2, when correcting for the area loss. This indicates that the anode resistance contributes to ~30% of the initial ASR, while only between 11 and 17% of the ASR after the test. Hence, Ni coarsening is not the dominating mechanism for the increase in ASR. However, it should be kept in mind that the assumption that the gas has access to the vicinity of all Ni particles is believed to underestimate the effect of the Ni particle coarsening.

It is interesting to note that even though a significant loss of percolating Ni is seen at most of the positions analyzed in the tested cell, the degree of percolation at the electrolyte interface is still as high as in non-tested reference samples. However, the percolation is mainly due to significantly larger particles and agglomerates compared to the reference samples. This might be an indication that Ni segregates towards the anode / electrolyte interface. Only a few micrometers from the interface, the percolation is significantly lower compared to the area closest to the interface.

The anode support of DK-34 had a percolating Ni area fraction of ~60%. In relation to the work presented in Chapter 4, a model anode support with 60% percolating Ni area fraction showed a conductivity of ~115 S/cm. The initial conductivity for the anode support in DK-34 is unknown, but it is reasonable to assume that the conductivity is similar to what was seen in the anode support materials studied in Chapter 4 (~450 S/cm). Based on this, the conductivity of the anode support of DK-34 can be expected to have decreased from ~450 to ~100 S/cm. In comparison, to the electrical conductivity of pure LSM in the cathode is 1 to 250 S/cm at temperatures from RT to 1000°C [76]. Thus, an LSM-YSZ composite cathode should not be expected to have an electrical conductivity over ~100 S/cm. This means that even after 2 years of testing, the Ni-YSZ anode support exhibit an electrical conductivity in the same range as what can be expected from a good LSM-YSZ composite cathode. Still, the conductivity of anode support is estimated to have decreased by 70-80%. In addition, the percolating Ni network in the anode support is seen to be coarser, which means that local sites within the anode support has lost electrical conductivity. If these local sites are big enough, the anode resistance can also be expected to increase due to a loss of active sites in the anode.

In order to study the impurity segregation and formation of any thin silica containing glass phases on surfaces at the interface between anode and electrolyte, a method providing higher resolution than SEM / X-EDS is required. The fact that no impurity phases were found in this study does only prove that no larger agglomerates are present. However, an impurity layer with the thickness of a few tens of nanometers would not be detected in the SEM, but could still affect the electrochemical performance of the anode.

5.3 PSC6953 and PSC7069A tested for 1,500 hours

5.3.1 Sample history

PSC6953 and PSC7069A have been tested for a period of 1500 hours, at 850°C and with current densities of 0.25 and 1.93 A/cm^2, respectively. The fuel gas and fuel utilization was similar as for the DK-34 cell. These two cells are not from the same production batch as DK-34 and therefore a reduced reference sample was included in the comparison as well. The electrical performance of these two cells has previously been reported by A. Hagen et al. [7], together with a collection of other cells tested at different temperatures and current loads. The two cells have been operated for a time corresponding to less than one tenth of that for the DK-34 cell. In this work, the aim is to qualitatively analyze the anode microstructure of these cells in order to get an idea of how severe the Ni rearrangements are after 1500 hours, compared to the 17500 hours of the DK-34 cell.

Over the first 1500 hours, the DK-34 cell showed a linear degradation of cell voltage. This was also the case for the PSC6953 cell, while PSC7069A showed an initial decrease / increase of the cell voltage. The mechanism behind the initial fluctuations of the cell voltage from PSC7069A is not fully understood.

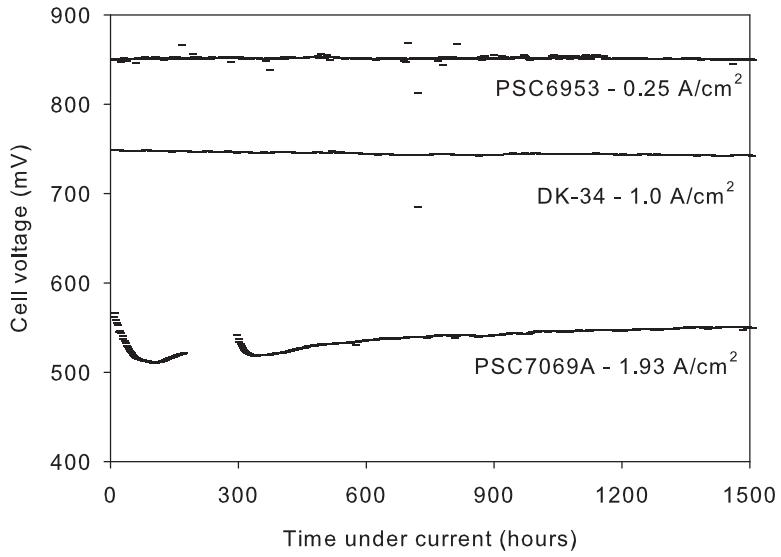

Figure 5-9. Cell voltage as a function of operation time for all three cells.

Sample pieces from the middle of the cell areas of the two cells were selected for microstructural studies and prepared in the same way as the DK-34 sample.

5.3.2 Microstructure

In Figure 5-10 SEM-CC images of the two tested cells and the reduced reference sample are shown. It can be seen that coarsening and loss of the percolating Ni has taken place in both of the tested cells. From the inspected sample cross sections, the coarsening is seen to be most severe in the PSC7069A cell, which was tested under the highest current density.

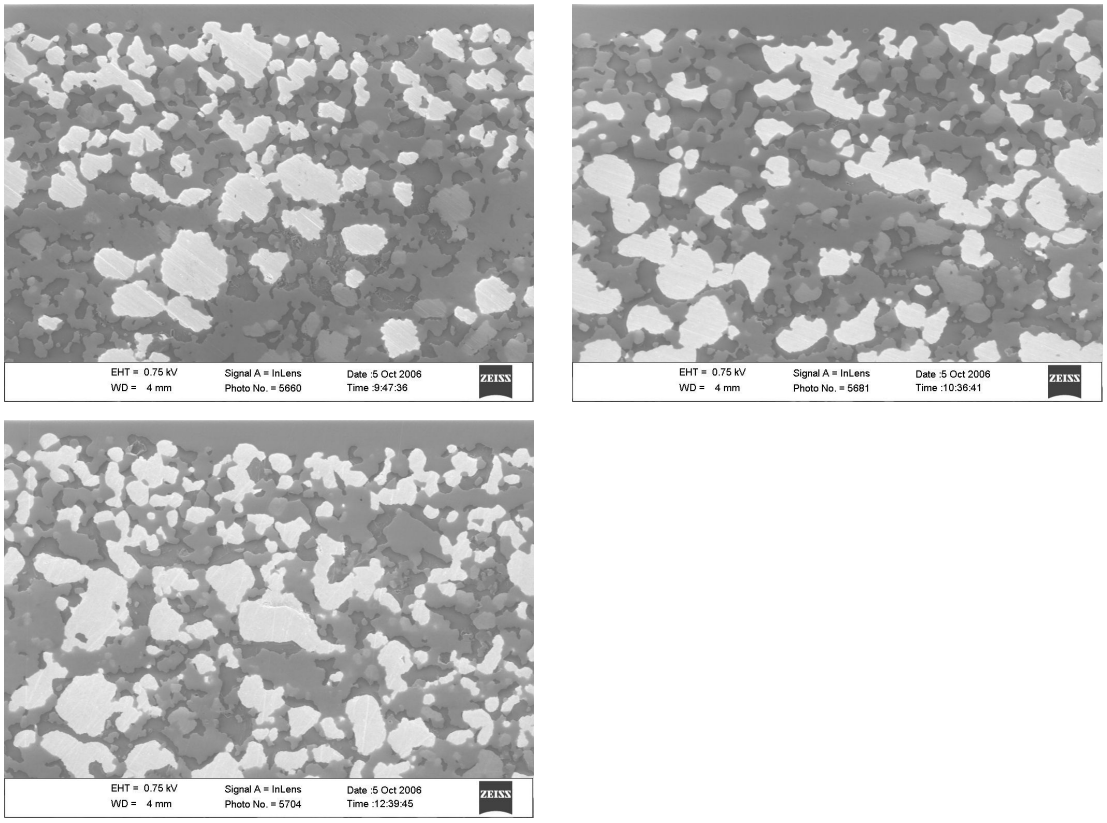

Figure 5-10. SEM-CC images from the anode of sample PSC6953 (top left), PSC7069A (top right) and the reduced reference (bottom). Percolating Ni is visualized.

A difference between the two samples is confirmed by quantitative image analysis (see Table 5-7) from which the average size of the percolating Ni was found to be 8 and 22% larger in PSC6953 (low current) and PSC7069A (high current) than the reduced reference. The average particle size of percolating Ni is smaller in these samples when compared to the two samples analyzed from the DK-34 cell. At the same time, the number of percolating particles is also higher in these samples compared to DK-34. However, the area fraction of percolating Ni is similar, or even lower, than for the DK-34 cell.

Since only one cross section for each of these cells is analyzed, no attempts to assign the difference in microstructure to the different current densities have been made. In order to do so, more than one sample piece along the fuel gas flow from

each cell should be analyzed. However, from the selected positions within the cell it can be concluded that PSC7069A have a percolating Ni particle size close to that of sample 3 from DK-34. PSC6953 shows a less severe increase in particle size.

Table 5-7. Particle size and area fraction of percolating Ni measured in the anode. Particle sizes and area fractions, as well as the given standard deviations, are normalized to the particle size or area fraction of the reference.

Sample ID	Normalized diameter	Standard deviation	Number of Ni particles	Area fraction
PSC6953	1.08	0.71	392 (74%)	0.83 ±0.07
PSC7069A	1.22	0.80	281 (53%)	0.75 ±0.07
Reference	1.00	0.71	528 (100%)	1.00 ±0.05

The coverage of percolating Ni closest to the electrolyte was measured and presented for DK-34 above. Similar measurements were performed on these samples and the results are presented in Table 5-8. It can be seen that the reference sample used for the DK-34 cell and the reference for the tested cells presented here have the same degree of percolating Ni / electrolyte contact, in approximately the same number of segments. At the same time, the results from measurements of the tested cells and the DK-34 cell are in the same range. Thus, based on the number of active triple phase points and TPB length, the degradation of short-term tested cells appears to be similar to the degradation of DK-34, despite the fact that the operation time differs with a factor of ten. However, it should be kept in mind that since the particle sizes for the DK-34 samples are smaller, it is reasonable to expect more open porosities around the Ni particles and thereby more room for the fuel gas to reach the triple phase points close to the electrolyte.

Table 5-8. The coverage (column 2) and number of segments of percolating Ni along the interface line between anode and electrolyte (column 3), the assumed maximum number of triple phase points along the line (column 4), and calculated triple phase boundary length (column 5).

Sample ID	Line coverage	No. of segments	Triple phase points	TPB length (m/cm^2)
PSC6953	0.44	84	168	30
PSC7069A	0.58	81	162	38
Reference	0.52	125	250	52

5.3.3 Discussion

After one tenth of the time that the DK-34 cell was operated, both PSC6953 and PSC7069A show signs of microstructural rearrangements of Ni. As for the DK-34 cell, the rearrangements are most prominent close to the anode / electrolyte interface. The area fraction of percolating Ni in the anode of sample PSC7069A is lower than in any of the other samples analyzed. However, from measurements only including the actual interface to the electrolyte, it can be seen that the same sample has a relatively high degree of percolation. A higher degree of percolating Ni close to the electrolyte was also seen in the samples from DK-34. When the whole anode area is included, PSC6953 shows a similar area fraction of percolating Ni as the samples from DK-34, while the average particle size is smaller. On the interface line along the electrolyte, this sample has a slightly lower coverage of percolating Ni, but still the same number of triple phase points.

Both PSC6953 and PSC7069A show similar values for the estimated TPB length when compared to DK-34.

5.4 Conclusions

DK-34 was tested under technologically relevant, although relatively severe conditions, and displayed a cell voltage degradation of <1% per 1,000 hours in the first 4,000 hours. After ~8,000 hours a gas leak is detected, whereupon the rate of degradation is increased. The leak is expected to have caused a loss of active cell area of about 16%. However, even after correcting for a cell area loss of 16%, ASR increases from 0.17 to 0.53 Ωcm^2.

A large amount of cracks in the YSZ interface between the anode and electrolyte was found. These cracks will act to weaken the interface mechanically and effectively limit the oxygen path into the anode YSZ structure. The effect on the anode performance is not clear, since Ni is still found to be in contact with the electrolyte.

The degree of Ni coarsening in the anode, closest to the electrolyte interface, depends on the position along the fuel gas flow. The coarsening is more severe close to the fuel gas outlet, which is ascribed to an increased concentration of H_2O in the fuel gas due to fuel utilization. Based on the available TPB length, the Ni coarsening can, depending on the position along the fuel gas flow, explain an increase of the anodic polarization resistance of up to 180%. Similar values are estimated in the two

cells operated for only 1,500 hours. It is possible that a local loss of percolation in relatively large areas of the anode support screens the anode from electrical connection. At the same time, the overall conductivity loss in the anode support is estimated to be 70-80%. On the other hand, the absolute conductivity is still estimated to be in the same range, or better, than a good LSM-YSZ composite cathode (~100 S/cm).

A relatively high degree of percolating Ni close to the anode / electrolyte interface, in contrast to the significantly lower degree of percolation only a few micrometers into the anode, is taken as an indication of Ni segregation towards the electrolyte interface.

Altogether, the microstructural degradation observed in the anode and the anode support is not sufficient to explain the degradation of the electrochemical performance of DK-34. Hence, significant degradation must be taking place also in the electrolyte and the cathode.

6 Microstructural aging of Ni-YSZ characterized by three-dimensional reconstruction

6.1 Introduction and background

In order to fully understand and realistically model the electrochemical performance of an SOFC composite electrode, a large number of parameters are required. Quite a few of these parameters are related to the microstructure, such as particle sizes, porosity and interconnectivity of all the phases. Until recently, the measured microstructural parameters used in modelling of SOFC electrodes have been based on 2D images of single sample cross-sections. In order to incorporate these parameters into a model describing the electrode, certain assumptions have to be made based on hypothetical 3D microstructures from stereological theory. The same problem is encountered when microstructural rearrangements and degradation of the electrodes are studied. In the case of Ni coarsening, assumptions have to be made with regard to the degree of agglomeration and phase interconnectivity.

For several reasons, access to detailed 3D microstructural data on the electrode would be an important contribution to the microstructural understanding and model work applied to porous SOFC electrodes. 3D information of tested fuel cells is expected to result in a better visualization and understanding of microstructural changes and degradation mechanisms during operation and aging.

Previously available techniques to acquire 3D information are e.g. X-ray tomography, mechanical polishing with sequential imaging and tomographic transmission electron microscopy (t-TEM). These techniques are, however, not suitable for studying SOFC electrodes. In these materials, the characteristic particle sizes are in the range of a few hundred nanometers to a few micrometers. X-ray tomography has a resolution limit around one micrometer and would hence not be able to resolve the microstructure. t-TEM yields a resolution in the nanometer range, but can only be applied on samples with a maximum thickness of ~100 nm. For representation of an SOFC electrode, a sufficiently large volume that can incorporate the largest particles is needed. At the same time, in order to represent the finest particles, the required technique should result in a resolution of <100 nanometers.

The specific surface area of a porous microstructure is a macro-homogenous parameter which can be correlated to the particle size and coarsening of a structure. Based on physisorption of an inert gas such as N_2 or Ar, the total surface area of a

porous structure can be determined by Brunauer-Emmett-Teller (BET) measurements. BET measurements would give the total free surface area of Ni and YSZ in an anode structure. Furthermore, by utilizing selective chemisorption of e.g. S or H_2, it is possible to determine the free Ni surface area. This combination of methods is used in supported Ni catalyst characterization, see e.g. [68] and references within. However, the surface area in a typical Ni-YSZ cermet is typically too small for accurate measurements. Another disadvantage of this method would be the lack of information concerning the interface area between the Ni and YSZ phases.

A dual beam FIB-SEM combines a nano-machining and a nano-imaging tool. By use of a FIB-SEM it is possible to perform advanced serial sectioning and imaging with an interlayer spacing of only tens of nanometers [77,78]. During the last few years the FIB-SEM technique has become available in many material research laboratories and the 3D applications have been successfully applied to a number of research areas, including SOFC Ni-YSZ anodes [47]. The method is under constant development with regard to equipment, sampling methods and subsequent image processing. By use of integrated drift correction, L. Holtzer et al. have achieved a reproducible section interspacing of 15 nm, which is on the same scale as the lateral resolution of SEM [79]. In this resolution range, the FIB-SEM serial sectioning technique builds a bridge between X-ray tomography and t-TEM. FIB-SEM can handle significantly larger sample volumes than t-TEM, with more than ten times higher resolution than X-ray tomography.

In this work, the aim has been to evaluate the FIB-SEM technique as a tool for acquiring useful 3D data from a tested Ni-YSZ anode. For this purpose, the FIB-SEM serial sectioning has been applied to a long-term tested anode and a reference sample for comparison. Both the 3D technique and the sample characteristics are evaluated. Three SOFC anode samples were chosen for three-dimensional reconstruction. The samples are; one upstream (sample 3) and one downstream (sample 4) from the long-term tested cell, DK-34, and a reference anode. These samples have also been studied by two-dimensional microscopy and the results from this study are presented in Chapter 5.

6.2 In-situ sample preparation and serial sectioning

Cross sections of epoxy impregnated samples were prepared in the same way as for ordinary SEM imaging, see section 2.3.1. The sample surface was coated with a

conducting carbon layer, mounted into the microscope and adjusted to the coincident point of the electron beam and ion beam (eucentric height).

The procedure during the three-dimensional reconstruction was as described in the following.

A representative cross sectional area of the sample was located by electron imaging and coated with a protective layer of Pt. This was done in order to protect the sample volume to be reconstructed from accidental ion milling and erosion during ion-beam imaging.

The FIB is used to mill a trench around the sample volume of interest, see Figure 6-1. At this point, the size of the sample volume to be reconstructed should already be decided, since the trenches define the sample cube. For the two samples presented in this work, the sample cubes were made approximately $26 \times 9 \times 9$ μm^3 and $18 \times 10 \times 9$ μm^3, respectively. The sample size needs to include a representative volume of the microstructure, where a number of typically sized particles are repeated throughout the volume. However, at the same time it is necessary to consider the machining time, which increases as the sample volume is increased. The above mentioned sample sizes were estimated to give a good compromise between sampling volume and time requirement. Of course, also the resolution of the collected data is closely related to the sampling volume and time requirement. As a general rule, ten sections per particle is necessary in order to reconstruct the granular texture of a particle [78]. In this initial work, the aim was set to reach this requirement for the average Ni particle size (~1 μm).

In addition to defining the size of the sample cube, the trenches create space around the sample cube, which is needed due to re-deposition of material during the sectional milling. The side trenches also reduce shadow effects from the side walls, which otherwise would induce an uneven brightness across the images and difficulties during image segmentation [78].

To assist in the later drift corrections and alignment of the image series, reference marks were created on top of the sample cube by use of Pt deposition. The reference marks were made as two crossing lines with known lengths and angles.

At this point, the sequential ion milling and SEM imaging could be started. During the sample preparation, sequential ion milling and electron beam imaging, the sample was tilted so that the polished sample surface was facing the ion gun

perpendicular and the electron gun at an angle of 52°. Thus, the SEM imaging was performed at a 38° angle from the normal of the image plane and no stage movements were necessary during the segmentation. A 50 nm thick layer of material was milled of the sample cube between each SEM image. The sample cubes were prepared so that the milling and image plane were in plane with the anode / electrolyte interface and the milling was performed through the anode towards the electrolyte interface. The sample cube before serial sectioning is illustrated in the images shown in Figure 6-1, where the milling direction and image plane are indicated.

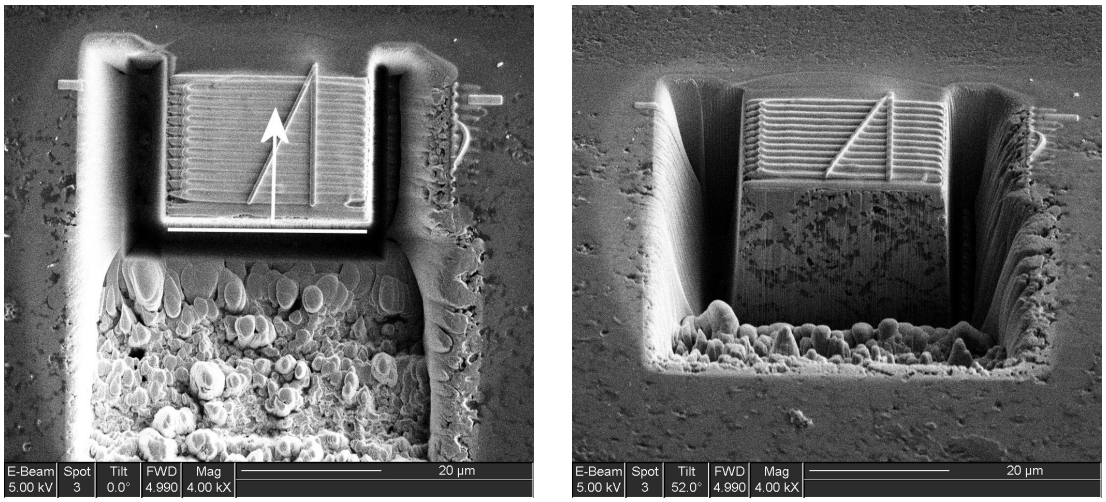

Figure 6-1. Sample cube after trenches and reference marks are made. (left) viewed perpendicular to the sample surface (as seen from ion-beam during milling) and (right) viewed at an angle of 52° (electron-beam view during milling). To the left, the white line indicates the image plane, and the arrow indicates the milling direction towards the electrolyte.

In addition to the reference marks, ion beam images were acquired after every tenth SEM image in order to track the progress of the FIB milled image-plane and make sure that the progress corresponded to the set slice thickness.

The operating conditions for the microscope during the sequential ion milling and electron imaging were as follows. Serial sectioning by the ion beam was performed at 30 kV accelerating voltage, a 300 pA beam aperture, and a magnification of 8 kX (reference) or 10 kX (tested sample). For electron imaging, a 5 kV accelerating voltage, spot size 3, and a magnification of 8 or 10 kX were used. The best settings for the SEM during electron imaging on the non-coated ion milled surface were evaluated. Electron images were recorded by use of the TLD detector operated in TLD-SE mode with a bias of +50 V. By use of these settings during SEM imaging, an image was acquired in which the Ni phase appears clearly darker than the

YSZ phase and the epoxy impregnation appears very dark. A typical image is shown in Figure 6-2, where the three phases are indicated. In this figure, the Ni-YSZ contrast is very clear; however, the contrast tends to decrease closer to the anode / electrolyte interface.

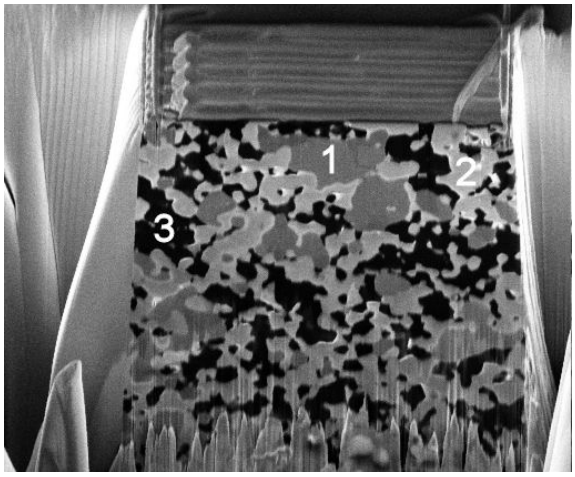

Figure 6-2. Raw SEM image of ion sectioned surface, acquired by the through-the-lens detector in SE mode at +50 V bias. The numbers indicate (1) Ni, (2) YSZ and (3) pore (epoxy).

The necessity of creating trenches surrounding the sample cube before serial sectioning can be seen in Figure 6-3. Without trenches, the indicated re-depositions would seriously have narrowed the image view before the cube was fully sectioned. Including in-situ sample preparation and sectioning, the total microscopy time for one sample was approximately 12 hours.

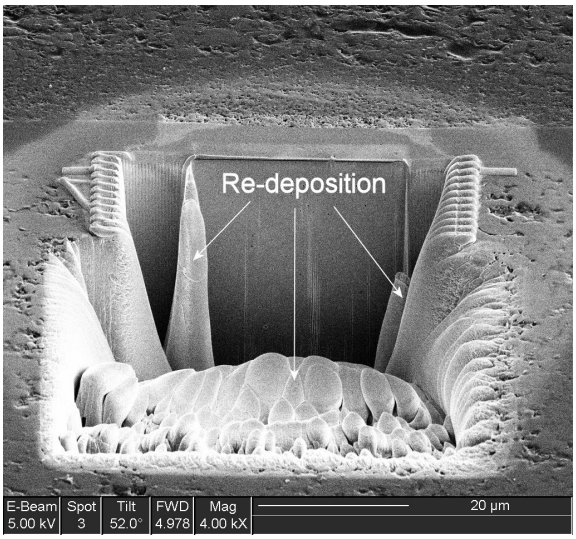

Figure 6-3. Image acquired at the sample site after serial sectioning. The arrows indicating re-deposited material surrounding the previous sample cube.

6.3 Image processing and reconstruction

After the serial sectioning and SEM imaging had been performed, the sample cube was represented by a series of SEM images. The resulting series of images were imported to the 3D software Amira in order to visualize the 3D characteristics. The images were stacked with an interspacing of 50 nm, in the same order as they had been captured. Both image series consisted of ~180 images each, representing the material from the electrolyte and 9 μm into the anode structure. Furthermore, the images were tilt corrected in order to compensate for the 38° tilting from the image normal and the image series aligned in order to correct for any beam or sample drift during acquisition. The resulting aligned stack of raw images could easily be three-dimensionally visualized in the Amira software. However, in order to visualize and extract information about each separate phase, the images need to be segmented. The optimal way of segmenting the images would be to develop a routine based on the grayscale or edge detection. Unfortunately, the contrast between Ni and YSZ is not stable enough to solely define the phases based on the grayscale. Instead the identification of Ni and YSZ had to be performed manually, while the pores (epoxy) easily could be segmented based on the grayscale thresholding. The images were segmented into nickel, YSZ and pore phase, but no attempts were made to separate individual particles or clusters.

6.4 Results

In Figure 6-4 selected image planes from the three dimensional visualization of the raw SEM images and the corresponding segmented reconstruction are shown for the reference sample. The process of segmentation was identified to be the most time consuming step in the full procedure of the reconstruction work. Due to a variance in the contrast throughout the sample, and sometimes even lack of contrast, the manual segmentation took a few weeks per sample. However, by improved image quality it should be possible to significantly reduce the amount of time required.

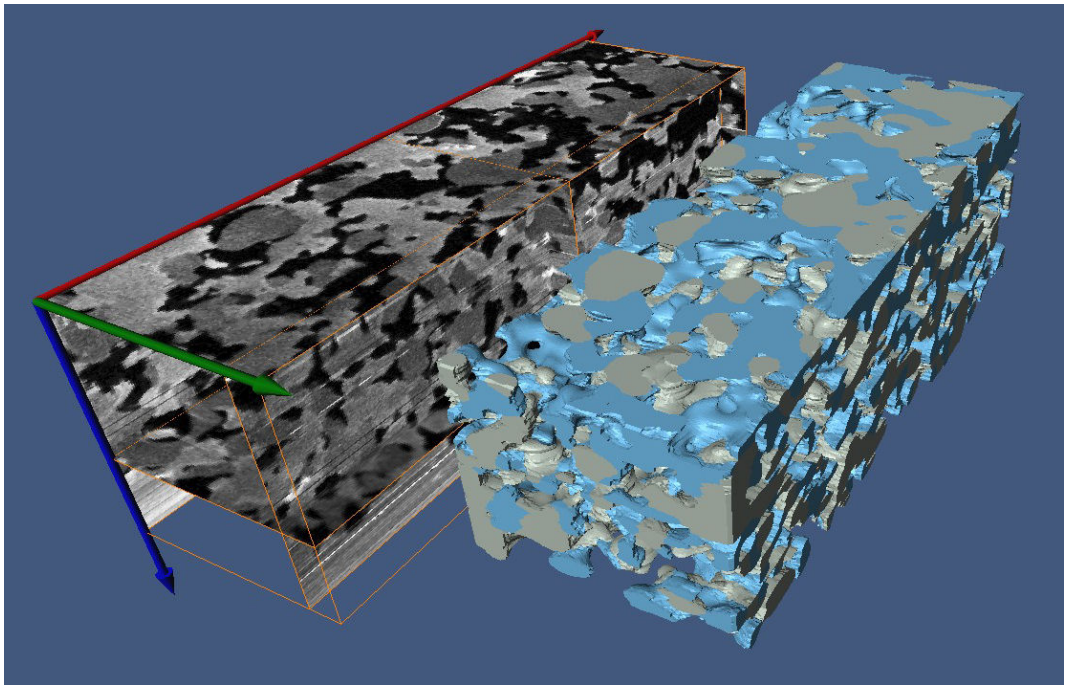

Figure 6-4. Image illustrating selected image planes in the raw-image reconstruction (left) and the corresponding surface reconstruction based on the segmented images (right). In the surface reconstruction, pores are shown as blue and Ni is shown as grey, while YSZ is transparent.

During the work on segmenting images in the sample sets it was realized that, due to insufficient contrast between Ni and YSZ, it was not possible to segment one of the samples (sample 3). In an ordinary, mechanically polished cross section Ni can still be distinguished form YSZ due to edge and surface features. However, in the cross sections milled by the FIB no such surface or edge features exist.

In the following, only the results from the reference sample and the downstream sample is therefore presented and discussed.

6.4.1 The resulting data sets

In Table 6-1, dimensional information about the two data sets are summarized. The difference in resolution in the image plane is due to the different magnifications used during imaging. The reference sample was too wide for using a magnification of 10 kX, while sample 4 was made somewhat narrower in order to fit the magnification of 10 kX. The corresponding surface reconstructions based on the data sets are shown in Figure 6-5 and Figure 6-6. In these figures, the grey phase is Ni, the blue phase is pores and the YSZ phase is transparent.

For the reference and sample 4 the sample cubes represent a cell area of 230 and 190 μm^2, respectively. These areas each represents only a very small fraction (less than 0.0015%) of the total cell area of 4×4 cm.

Table 6-1. Sample volume dimensions in absolute measures and the corresponding digital resolution of the reconstruction. The total data set is represented by 360×95×181 (=6.19×10^6) voxels for the reference and 304× 141× 178 (7.63×10^6) voxels for sample 4.

Reference sample	**X (µm)**	**Y (µm)**	**Z (µm)**	**V_{tot} (µm^3)**
Sample dimensions	26.280	8.835	9.050	2100
Voxel dimensions	0.073	0.093	0.050	0.34×10^{-3}
Number of pixels	360	95	181	-
Sample 4	**X (µm)**	**Y (µm)**	**Z (µm)**	**V_{tot} (µm^3)**
Sample dimensions	17.936	10.575	8.900	1688
Voxel dimensions	0.059	0.075	0.050	0.22×10^{-3}
Number of pixels	304	141	178	-

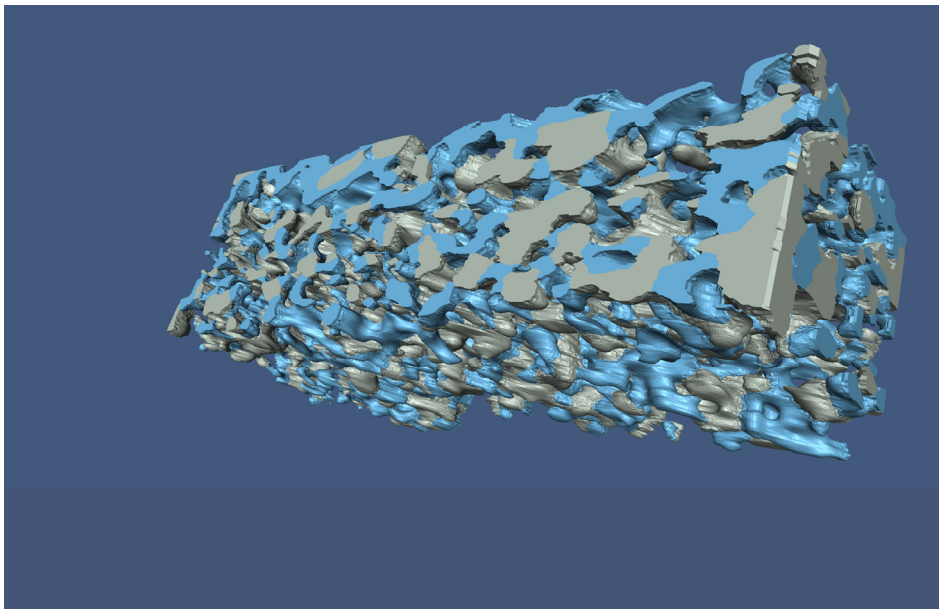

Figure 6-5. Illustration of surface reconstruction of the reference sample. Grey is Ni, blue is pores and YSZ is transparent.

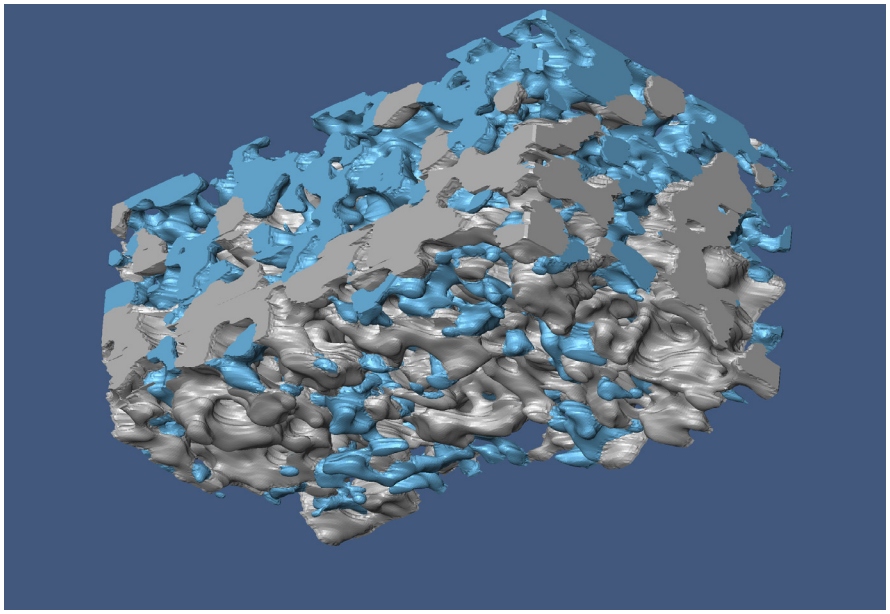

Figure 6-6. Illustration of surface reconstruction of the tested sample 4. Ni is grey, pores are blue and YSZ is transparent.

The most basic 3D data possible to extract from the data sets for the reference and sample 4 are illustrated in Figure 6-7 and Figure 6-8, respectively. In these figures the area / volume fraction of each phase is plotted vs. distance from the electrolyte. The gradual transition is due to a slightly uneven interface between anode and electrolyte. In general it can be seen that the plots are smooth and without any large shifts between images. However, from the smooth fluctuations in the YSZ area fraction it can be seen that data is locally affected by single YSZ grains or agglomerates.

In the reference sample (Figure 6-7), the fractions of Ni and pores present a similar development from the electrolyte through the anode. The pore fraction reaches a relatively stable value of 20%, while Ni varies between 20-30%. YSZ varies between 50-60%.

In sample 4 the YSZ fraction displays a trend similar to what is seen in the reference. However, Ni and pores show a different behavior in comparison to the reference. The Ni fraction increases to 50% at around 3 µm into the anode. Further into the anode the Ni fraction goes down to below 20%. At the same time, the fraction of pores displays the opposite trend. 3 µm into the anode, where the volume fraction of Ni is twice as high as in the reference, the pore fraction is only 50% of the corresponding pore fraction for the reference.

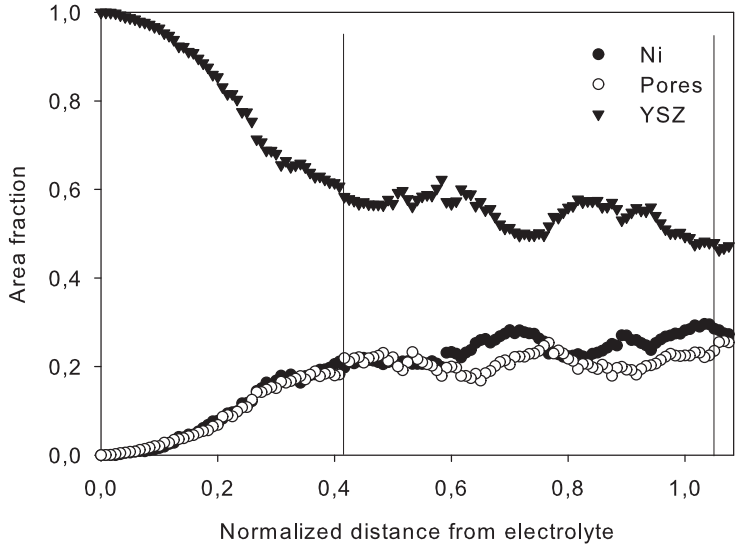

Figure 6-7. Area fraction of the Ni, pores and YSZ, as a function of distance from the electrolyte into the anode structure of the reference samples. Vertical lines indicate the position of the trimmed sample volumes described below.

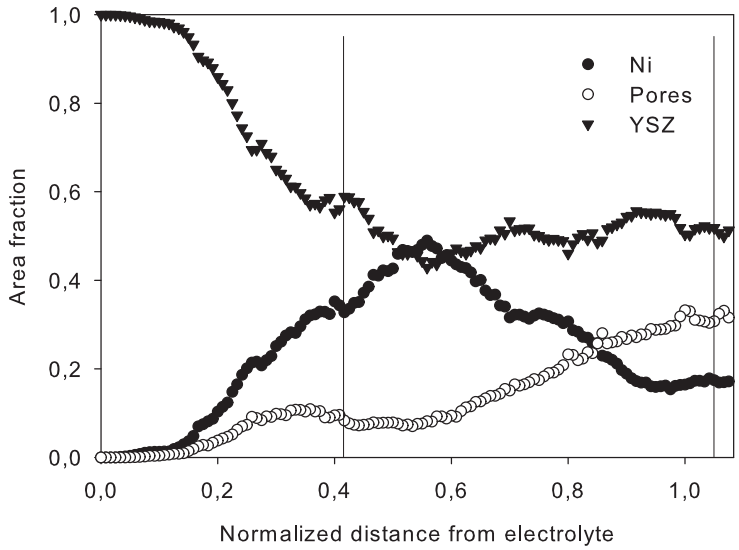

Figure 6-8. Area fraction of Ni, pores and YSZ, as a function of distance from the electrolyte into the anode structure of sample 4. Vertical lines indicate the position of the trimmed sample volumes described below.

A similar plot, representing area fraction of the three components, would also be possible to acquire from a single cross section with a few degrees inclination from the parallel of the anode / electrolyte interface. Different positions along the cross section would represent different distances to the interface from where area fractions are measured. From this type of sample preparation, a more statistical measurement should be expected since the measured area could be significantly increased.

However, it would not be possible to collect the 3D information about phase interconnectivity by this method. In addition, each image along the inclined cross section would represent different cell positions and information would be collected without knowledge of whether variations were due to distance from electrolyte or due to different positions across the cell area.

For further measurements and data evaluation, the two reconstructions were trimmed to the same anode thickness of 3.8 µm (corresponding to 76 images within the anode), as marked out by vertical lines in Figure 6-7 and Figure 6-8.

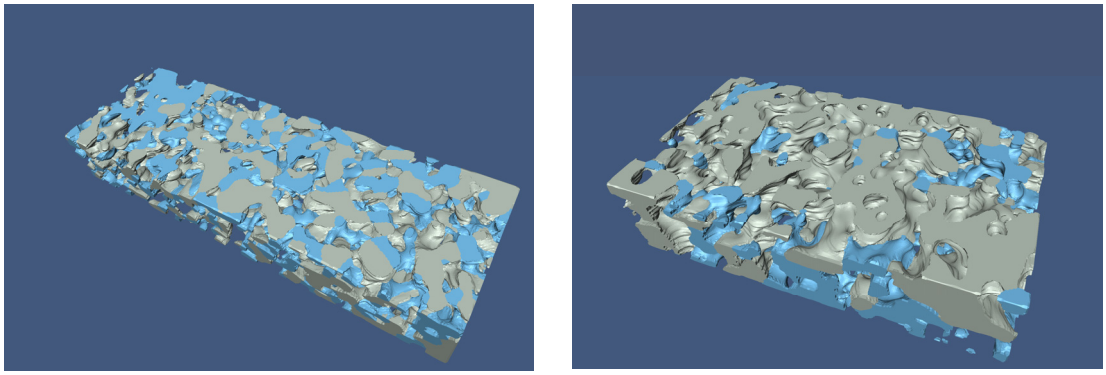

Figure 6-9. Illustration of the trimmed 3.8 µm thick sample volumes of the reference (left) and sample 4 (right). For both volumes the surface facing upwards is the surface closest to the electrolyte.

From the trimmed sample volumes, shown in Figure 6-9, the volume fractions and specific surface area of each phase was measured by use of standard functions available in the Amira software. The total volume fraction (V_f) of each phase (Ni, YSZ and pores) in the trimmed sample volumes was extracted. The changes in the volume fraction of the three phases in sample 4, relative to the reference sample, is presented in Table 6-2

Table 6-2. The change of volume fraction of Ni, Pores and YSZ of sample 4, normalized to what was measured in the reference sample.

	Ni	Pores	YSZ
ΔV_f (%)	+ 24	- 9.5	-7.4

Under the assumption that the YSZ structure is stable during reduction of NiO to Ni and assuming a 41% volume reduction of NiO transforming to metallic Ni, the volume fractions before reduction ($V_{f,\ pre\text{-}red.\ calc.}$) can be calculated. When $V_{f,\ pre\text{-}red.\ calc.}$ is calculated it is assumed that the volume reduction corresponds to part or all of the

available porosity. From the volume fractions calculated before the samples were reduced, a porosity of 4% can be calculated for the reference sample. The corresponding calculation for sample 4 yields the impossible pore fraction of -0.03% before reduction. From Figure 6-8 it is clear that the overrepresentation of Ni would be even more severe if the calculations had been done closer to the electrolyte interface. However, further into the anode the pore / Ni fraction increases and reaches the theoretically necessary ratio (~0.7) 4.8 μm into the anode. In the reference sample this ratio is fulfilled throughout the anode structure.

In Table 6-3, the interface area between solid phases (Ni or YSZ) and the pores, as measured from the selected sample volumes, is given for both samples. This type of measurement is equivalent to the specific surface area measured by the BET method. The values are extracted directly from the surface reconstructions. Only the internal areas are included, while the surface areas surrounding the cubes are excluded.

Table 6-3. Specific surface area between of the total sample weight and total sample volume, as measured in the reconstructions by the Amira software.

	Surface area (m^2/g)	Surface area (m^2/cm^3)
Reference	0.25	1.39
Sample 4	0.16	0.92

From these measurements it is evident that sample 4 has a significantly smaller specific surface area (-36%) in comparison to the reference. In order to distinguish the surface areas corresponding to the different phases (Ni and YSZ), the surface area of each phase was extracted from the reconstruction. In Table 6-4, the surface area for Ni and YSZ is given separately. The surface area of each phase per weight of that single phase is given in the second column. This measurement is equivalent to a BET measurement on Ni and YSZ networks alone. From these data it can be seen that the specific surface area of YSZ is similar in the two samples, while the area of the Ni phase in sample 4 is 35% less than in the reference sample. In the third column, the surface area of each phase in relation to the total sample volume is given for comparison to previously presented values. From the results presented in Table 6-4 it is evident that the difference in specific surface area of the total sample volume (presented in Table 6-3) are solely due to a difference in the Ni phase.

Table 6-4. Specific surface area per gram of the specific phase and per volume of the total sample as measured in the reconstruction by the Amira software.

Reference	**Surface area (m^2/g)**	**Surface area (m^2/cm^3)**
Ni network	0.63	1.39
YSZ network	0.58	1.92
Sample 4	**Surface area (m^2/g)**	**Surface area (m^2/cm^3)**
Ni network	0.41	1.12
YSZ network	0.59	1.80

6.5 Discussion and conclusions

6.5.1 The 3D reconstruction

An uneven brightness was often seen from top and down in the SEM images. By using a different ex-situ sample preparation, which could make it possible to perform the serial sectioning at the edge of the sample, would create more open space around the area of interest. The space would reduce shadow effects and also prevent re-deposition from building up around the sectioned area.

In the images of the FIB milled cross sections acquired by the TLD detector in SE-mode and with a bias of +50 V, a clear contrast is observed between Ni and YSZ. YSZ is clearly brighter than Ni. However, the contrast is not stable throughout the serial sectioning, but varies. The same effect is seen from top to bottom in the images, as the total intensity also decreases. This is believed to be due to shadow effects. Therefore, again, more open space around the sample cube would be beneficial to the image quality.

The use of epoxy impregnation of the pores has not been reported previously in relation to 3D reconstructions of SOFC electrodes. At this relatively low acceleration voltage, epoxy is not seen to charge, which would be seriously detrimental to the image quality. On the contrary, epoxy appears very dark which creates a good contrast for the pores.

The similar surface areas measured for the YSZ phases in the reference and the tested anode indicate that the slight difference in sampling resolution has not affected the measured quantities significantly. The differences measured between the samples are believed to be due to actual differences in sample characteristics. The measured differences in surface areas of Ni and pores are also qualitatively coherent to the

visual impression. However, in future work, care should be taken to make sure that similar sampling parameters are used in order to facilitate comparison.

In the work to reconstruct a Ni-YSZ anode, J. R. Wilson et al. [47] vary the image resolution in order to evaluate potential errors on the calculated interfacial areas. When they changed the resolution from 13.9 nm to 41.7 nm, the reduction of the interfacial area was found to be approximately 5%. This was taken as an indication for the fact that the resolution was sufficient with regard to avoiding significant errors in the anode they studied. In this work, the image resolution is lower due to the simultaneous consideration of sample size, image quality, acquisition time and risk of sample drift. However, it would be of interest to perform a similar test in order to evaluate the effect of the resolution on the measurements.

Relatively large sampling volumes were sectioned and reconstructed. Still, in the plots of area fraction vs. distance to the electrolyte interface, an influence of individual particles or agglomerates of YSZ can be seen. This can be taken as an indication that the sampling does not give a fully statistical representation. If this requirement should be fulfilled, a larger sample volume needs to be considered and thus, longer acquisition times.

6.5.2 The long-term tested anode

The anodes that have been reconstructed and analyzed in this chapter were subject for a 2D analysis in chapter 5. From this analysis it was concluded that in comparison to the reference anode, the Ni particle size was significantly larger in the tested anode, especially close to the electrolyte interface. At the same time as the Ni particles were seen to become larger, the degree of percolation was seen to decrease. However, close to the anode / electrolyte interface, the percolation was still found to be high despite the fact that particles are larger. The particle growth, in combination with a remaining high degree of percolation, was taken as an indication of Ni segregation towards the electrolyte interface.

In the particular sample volume acquired and three-dimensionally reconstructed from this same long-term tested anode, it is not relevant to use the term Ni particles in order to describe the Ni phase close to the electrolyte interface. Rather, the Ni phase can be seen as a continuous phase filling the space given by the YSZ network. In this particular sample volume, the Ni volume fraction is high enough to conclude that Ni segregation on the length scale of several micrometers has occurred.

A significant amount of Ni must have segregated from the surrounding anode structure in order to yield the measured Ni content. The sample volume is too small to unambiguously determine from what direction the extra Ni has segregated. However, the Ni volume fraction significantly decreases further out from the electrolyte interface, which can be seen in the illustrated surface reconstructions. This indicates that the excess of Ni found close to the electrolyte has segregated from the outer parts of the anode. It should be remembered that the reconstructed cell areas each represents less than 0.0015% of the total active cell area. In order to supplement these very locally probed studies, measurements on a single cross section with a few degrees inclination from the parallel of the anode / electrolyte interface would give valuable statistical information. Segregation of Ni from the outer parts, further from the electrolyte, is indicated on a more general basis by the results from the two-dimensional analysis. Thus, the 2D analysis from chapter 5 indicates that the Ni agglomeration close to the electrolyte interface measured in the three-dimensional reconstruction is a representative characteristic for a larger part of the anode.

The results indicate that Ni segregates towards the electrolyte interface, where the H_2O concentration is assumed to be higher than what it is further in to the anode structure. This observation must be considered to be unexpected if the Ni segregation is only due to a concentration gradient of H_2O and Ni-OH species. If this would be the case, it can be expected that a higher concentration of Ni-OH species close to the electrolyte interface should lead to diffusion in the direction away from this interface, where the concentration of such species can be assumed to be lower.

The measured loss of Ni surface area is qualitatively in agreement to what was seen in the two-dimensional analysis. The measured larger particle size should result in a lower surface area.

7 Overall discussion

In this work, optical microscopy, SEM, FIB, image analysis and in-situ electrical conductivity measurements have been utilized in order to evaluate the microstructural rearrangements and degradation within Ni-YSZ cermets. Despite the fact that the resolution of OM is low and that it is only possible to study the Ni-phase, valuable information concerning coarsening of Ni particles has been extracted. By applying OM to aged model Ni-YSZ cermets and tested Ni-YSZ anodes, it has been possible to observe changes with regard to particle size and spatial density in the Ni phase.

SEM-CC has proven to be a useful tool in order to study percolating Ni as this technique makes it possible to obtain semi-three-dimensional information concerning the Ni particle interconnectivity from a two-dimensional sample cross section. This information cannot be acquired by any other two-dimensional imaging techniques.

The combination of microstructural analyses and in-situ electrical conductivity measurements has made it possible to determine the effect of H_2O concentration, not only on Ni particle size, but also on the kinetics for the Ni sintering process (chapter 4).

It proved to be difficult to come to any firm conclusions regarding the correlation between the microstructural degradation in the anode and the measured cell degradation by utilizing electrochemical measurements from the long-term tested cell (DK-34). One of the reasons to this might be that the most significant microstructural changes take place at the cathode. However, the purpose of this study was not to correlate the microstructural degradation in the anode to the overall cell degradation but to study the effect of severe long-term testing of the Ni-YSZ anode. The coarsening and the rearrangement in the Ni phase are most significant close to the electrolyte interface. From microstructural analyses of the anode in 4 different positions, the degree of Ni coarsening is also shown to be more severe in the positions close to the fuel gas outlet. This effect is attributed to an increasing concentration of H_2O, both close to the electrolyte interface and along the fuel gas flow. Furthermore, from SEM-CC images it is evident that the Ni percolation is higher close to the electrolyte interface, when compared to the outer parts of the anode. A better percolation, despite a significant particle coarsening, can be explained by a segregation of Ni towards the electrolyte interface (chapter 5).

Three-dimensional reconstruction by use of FIB-SEM is a time consuming technique. However, both quantitative and qualitative results yield additional insights to the Ni-YSZ microstructure when compared to two-dimensional techniques. One major advantage is the possibility to visualization the phase interconnectivity. In addition, local effects such as the segregation of Ni mentioned above can only be qualitatively observed or statistically quantified from two-dimensional imaging. However, from the three-dimensional reconstruction an actual volume of the sample is quantified.

An anode sample, taken from the anode close to the fuel gas outlet of a long-term tested cell, was chosen for a three dimensional reconstruction. In the selected and reconstructed sample cube the volume fraction of Ni is high enough to conclude that a significant amount of Ni must have segregated on the length scale of several micrometers to fill most of the space given by the YSZ network (chapter 6). As mentioned above, results from two-dimensional image analysis indicates that the Ni excess is due to a segregation of Ni from the outer part of the anode towards the interface.

Even if an effect of H_2O concentration on Ni atom mobility and Ni particle coarsening is accepted, the higher degree of coarsening of Ni particles at the anode / electrolyte interface might not be fully explained by this fact. It is reasonable to assume that the higher concentration of H_2O here, than compared to rest of the anode and anode support, has a dominating effect on the Ni mobility. However, an additional effect from polarization over the anode / electrolyte interface cannot be excluded. The polarization of the Ni / YSZ interface might affect the surface properties of Ni, which in turn can be expected to alter the surface diffusion of Ni atoms.

8 Final conclusions

Application of low-voltage SEM on non-coated Ni-YSZ cross sections was demonstrated to yield two useful types of contrasts between the phases in Ni-YSZ composites. At the same time, the importance of using various sample preparation methods, microscope settings and detectors to pick up relevant signals, carrying the phase information of interest, was illustrated.

An increased H_2O / H_2 ratio was seen to promote surface diffusion of Ni on the Ni particles, particle coarsening and conductivity loss within the Ni-YSZ cermet. At high concentrations of H_2O, Ni particle coarsening without any significant effect on the conductivity was observed. In connection to this it was proposed that diffusion of Ni across the YSZ surface or via vapor phase is involved in Ni sintering by formation of OH-bonded Ni complexes. The weak correlation between electrical conductivity and particle coarsening observed at high H_2O concentrations points to the fact that electrical conductivity measurements alone cannot describe Ni coarsening.

In a long-term electrochemically tested cell, the degree of Ni coarsening was demonstrated to be more severe closest to the electrolyte interface and close to the fuel gas outlet. In correspondence to what was mentioned above, this effect is to a great extent attributed to an increased Ni atom mobility at high concentrations of H_2O.

Even though the operating conditions of this long-term tested cell was carefully controlled, in order to minimize the risk for mechanical failure due to e.g. thermal shock or oxidation of the anode, a significant amount of cracks between the YSZ phases of the electrolyte and the anode was observed.

The possibility to perform high resolution three-dimensional reconstructions of SOFC electrodes makes it feasible to acquire three-dimensional microstructural information without the need to rely on statistical assumptions. 3D reconstructed sample volumes have been proven to be a valuable supplement to the much less time consuming 2D analyses.

9 Future outlook

The use of low-voltage SEM in order to achieve contrast between Ni, YSZ and pores would a give better resolution and detection of even the smallest Ni particles. Such a study can be expected to give valuable information with regard to the presence of Ostwald ripening within Ni-YSZ anodes. In contrast to optical microscopy, this imaging technique also facilitates high resolution detection and measurements of all three phases which is valuable for comparison of different types of Ni-YSZ cermets.

A segregation of Ni towards the anode / electrolyte interface was observed in the cell tested for 17,500 hours. Since an effect from polarization over the interface on this Ni segregation cannot be excluded, a study of the effect from polarization over the anode interface would be of interest. This study would preferably be performed on symmetric anode cells, with anode on both sides of the electrolyte, in order for interference of the cathode polarization and degradation to be excluded.

In order to fully extract the available information from a three-dimensional reconstruction, development of a procedure to extract additional quantitative information, such as TPB lengths and tortuosity of all three phases, is needed. Furthermore, the three-dimensional reconstruction can be used to develop a detailed electrochemical model in order to connect the microstructural information quantitatively to the electrode performance.

In order to study the impurity segregation and formation of thin silica containing glass phases at the interface between anode and electrolyte, a method providing higher resolution than SEM / X-EDS is demanded. For this purpose a TEM / X-EDS study of the long-term tested cell analyzed in this work and anodes from varying operation conditions would be valuable. Such study is believed to be greatly facilitated from samples preparation by FIB.

References

1. N. Q. Minh and T. Takahashi, *Science and Technology of Ceramic Fuel Cells* (Elsevier Science B.V., Amsterdam, 1995).

2. S. P. Jiang, Journal of Materials Science, 38 (2003) 3775.

3. S. Primdahl, M. Mogensen, Journal of the Electrochemical Society, 144 (1997) 3409.

4. F. Tietz, H. P. Buchkremer, D. Stöver, Journal of Electroceramics, 17 (2006) 701.

5. Mogensen, M., Larsen, P. H., Hendriksen, P. V., Kindl, B., Bagger, C., Linderoth, S., In Solid Oxide Fuel Cells (SOFC-VI), ed. S. C. Singhal and M.Dokiya. Pennington, New Jersey, 1999, pp. 904-915.

6. Liu, Y. L., Thydén, K., Xing, Q., Johnson, E., In Proceedings of the 26th Risø Symposium on Materials Science: Solid State Electrochemistry, ed. S. Linderoth *et al.* Roskilde, Denmark, 2005, pp. 273-278.

7. A. Hagen, R. Barfod, P. V. Hendriksen, Y. L. Liu, S. Ramousse, Journal of the Electrochemical Society, 153 (2006) A1165.

8. Barfod, R., Hagen, A., Ramousse, S., Hendriksen, P. V., In Proceedings of the 26th Risø Symposium on Materials Science: Solid State Electrochemistry, ed. S. Linderoth *et al.* Roskilde, Denmark, 2005, pp. 121-126.

9. S. P. Jiang, S. P. S. Badwal, Solid State Ionics, 123 (1999) 209.

10. S. Primdahl, M. Mogensen, Journal of the Electrochemical Society, 146 (1999) 2827.

11. S. Primdahl, M. Mogensen, Journal of the Electrochemical Society, 145 (1998) 2431.

12. M. Hattori, Y. Takeda, Y. Sakaki, A. Nakanishi, S. Ohara, K. Mukai, J. H. Lee, T. Fukui, Journal of Power Sources, 126 (2004) 23.

13. B. Butz, P. Kruse, H. Stormer, D. Gerthsen, A. Muller, A. Weber, E. Ivers-Tiffee, Solid State Ionics, 177 (2006) 3275.

14. S. Linderoth, N. Bonanos, K. V. Jensen, J. B. Bilde-Sorensen, Journal of the American Ceramic Society, 84 (2001) 2652.

15. M. Hattori, Y. Takeda, J. H. Lee, S. Ohara, K. Mukai, T. Fukui, S. Takahashi, Y. Sakaki, A. Nakanishi, Journal of Power Sources, 131 (2004) 247.

16. C. C. Appel, N. Bonanos, A. Horsewell, S. Linderoth, Journal of Materials Science, 36 (2001) 4493.

17. A. E. Hughes, S. P. S. Badwal, Solid State Ionics, 46 (1991) 265.

18. A. E. Hughes, Journal of the American Ceramic Society, 78 (1995) 369.

19. J. Nowotny, C. C. Sorrell, T. Bak, Surface and Interface Analysis, 37 (2005) 316.

20. M. de Ridder, A. G. J. Vervoort, R. G. van Welzenis, H. H. Brongersma, Solid State Ionics, 156 (2003) 255.

21. Mogensen, M., In Proceedings of the 26th Risø Symposium on Materials Science: Solid State Electrochemistry, ed. S. Linderoth *et al.* Roskilde, Denmark, 2005, pp. 51-66.

22. T. Iwata, Journal of the Electrochemical Society, 143 (1996) 1521.

23. H. Y. Tu, U. Stimming, Journal of Power Sources, 127 (2004) 284.

24. P. Metzger, K. A. Friedrich, H. Muller-Steinhagen, G. Schiller, Solid State Ionics, 177 (2006) 2045.

25. Gubner, A., Landes, H., Metzger, J., Seeg, H., Stubner, R., In Solid Oxide Fuel Cells (SOFC-V), ed. U. Stimming *et al.* Pennington, New Jersey, USA, 1997, pp. 844-850.

26. K. V. Jensen, Ph.D.Risoe National Laboratory (2002).

27. Y. L. Liu, S. Primdahl, M. Mogensen, Solid State Ionics, 161 (2003) 1.

28. Y. L. Liu, C. G. Jiao, Solid State Ionics, 176 (2005) 435.

29. J. V. T. Høgh, Ph.D.Risø National Laboratory (2005).

30. T. Klemensø, C. Chung, P. H. Larsen, M. Mogensen, Journal of the Electrochemical Society, 152 (2005) A2186.

31. T. Klemensø, M. Mogensen, Journal of the American Ceramic Society, 90 (2007) 3582.

32. Y. D. Zhen, A. I. Y. Tok, S. P. Jiang, F. Y. C. Boey, Journal of Power Sources, 170 (2007) 61.

33. M. C. Tucker, H. Kurokawa, C. P. Jacobson, L. C. De Jonghe, S. J. Visco, Journal of Power Sources, 160 (2006) 130.

34. Heneka, M. J., Ivers-Tiffée, E., In Proceedings of the 26th Risø Symposium on Materials Science: Solid State Electrochemistry, ed. S. Linderoth *et al.* Roskilde, Denmark, 2005, pp. 215-222.

35. A. Mitterdorfer, L. J. Gauckler, Solid State Ionics, 111 (1998) 185.

36. R. Hartung, H.-H. Möbius, Chemie-Ina. -Techn., 40 (1968) 592.

37. M. Mogensen and P. V. Hendriksen, in High Temperature Solid Oxide Fuel Cells. Fundamentals, Design and Applications, Elsevier, New York, 2003, Ch. 10.

38. A. Hagen, M. Menon, R. Barfod, P. V. Hendriksen, S. Ramousse, P. H. Larsen, Fuel Cells, 6 (2006) 146.

39. J. R. Macdonald and W. B. Johnson, John Wiley & Sons, Inc., Hoboken, New Jersey, 2005.

40. R. Barfod, A. Hagen, S. Ramousse, P. V. Hendriksen, M. Mogensen, Fuel Cells, 6 (2006) 141.

41. R. Barfod, M. Mogensen, T. Klemenso, A. Hagen, Y. L. Liu, P. V. Hendriksen, Journal of the Electrochemical Society, 154 (2007) B371.

42. S. Primdahl, M. Mogensen, Journal of Applied Electrochemistry, 30 (2000) 247.

43. D. Simwonis, F. Tietz, D. Stöver, Solid State Ionics, 132 (2000) 241.

44. K. R. Lee, S. H. Choi, J. Kim, H. W. Lee, J. H. Lee, Journal of Power Sources, 140 (2005) 226.

45. Ackermann, J.. Manual for the SUPRA (VP) and ULTRA Scanning Electron Microscopes. SmartSEM V. 05.00. 2005. Carl Zeiss SMT Ltd.
Ref Type: Catalog

46. E. E. Underwood, *Quantitative Stereology* (Addiston-Wesley Publishing Company, 1970).

47. J. R. Wilson, W. Kobsiriphat, R. Mendoza, H. Y. Chen, J. M. Hiller, D. J. Miller, K. Thornton, P. W. Voorhees, S. B. Adler, S. A. Barnett, Nature Materials, 5 (2006) 541.

48. G. R. Watt, B. J. Griffin, P. D. Kinny, American Mineralogist, 85 (2000) 1784.

49. K. T. Chung, J. H. Reisner, E. R. Campbell, Journal of Applied Physics, 54 (1983) 6099.

50. Z. Barkay, B. Dwir, G. Deutscher, E. Grunbaum, Applied Physics Letters, 55 (1989) 2787.

51. A. M. Borchert, K. S. Vecchio, R. D. Stein, Scanning, 13 (1991) 344.

52. H. Johansen, S. Gogoll, E. Stenzel, M. Reichling, E. Matthias, Journal of Applied Physics, 80 (1996) 4928.

53. D.C. Joy, Compiled experimental electron scattering data http://www.mc-set.com. (2006)

54. J. Cazaux, Microscopy and Microanalysis, 10 (2004) 670.

55. J. Cazaux, Journal of Microscopy, 214 (2004) 341.

56. J. I. Goldstein, D. E. Newbury, P. Echlin, D. C. Joy, A. D. Romig, C. E. Lyman, C. Fiori, and E. Lifshin, *Scanning Electron Microscopy and X-ray Microscopy.* (Plenum Press, New York, 1992), p. 115.

57. J. J. Donovan, N. E. Pingitore, A. Westphal, Microscopy and Microanalysis, 9 (2003) 202.

58. D. Drouin, A.R. Couture, R. Gauvin, P. Hovington, P. Horny, and H. Demers, monte CArlo SImulation of electroN trajectory in sOlids, CASINO 2.42, (2002)

59. D. E. Newbury, D. C. Joy, P. Echlin, C. E. Fiori, and J. I. Goldstein, *Advanced Scanning Electron Microscopy and X-ray Microanalysis* (Plenum Press, New York and London, 1986), p. 47.

60. X. Mantzouris, N. Zouvelou, D. Skarmoutsos, P. Nikolopoulos, F. Tietz, Journal of Materials Science, 40 (2005) 2471.

61. D. W. Dees, T. D. Claar, T. E. Easler, D. C. Fee, F. C. Mrazek, Journal of the Electrochemical Society, 134 (1987) 2141.

62. D. Skarmoutsos, A. Tsoga, A. Naoumidis, P. Nikolopoulos, Solid State Ionics, 135 (2000) 439.

63. J. H. Lee, H. Moon, H. W. Lee, J. Kim, J. D. Kim, K. H. Yoon, Solid State Ionics, 148 (2002) 15.

64. T. Kawashima, M. Hishinuma, Materials Transactions Jim, 37 (1996) 1397.

65. R. Vassen, D. Simwonis, D. Stöver, Journal of Materials Science, 36 (2001) 147.

66. A. Tsoga, A. Naoumidis, P. Nikolopoulos, Acta Materialia, 44 (1996) 3679.

67. J. Sehested, Catalysis Today, 111 (2006) 103.

68. J. Sehested, J. A. P. Gelten, I. N. Remediakis, H. Bengaard, J. K. Norskov, Journal of Catalysis, 223 (2004) 432.

69. S.-U. L. Kang, *Sintering - Densification, grain growth and microstructure* (Elsevier Butterworth-Heinemann, Oxford, 2005).

70. W. D. Kingery, H. K. Bowen, and D. R. Uhlmann, *Introduction to Ceramics* (John Wiley & Sons, Inc, New York, 1976).

71. C. H. Bartholomew, Applied Catalysis A-General, 212 (2001) 17.

72. C. H. Bartholomew, Applied Catalysis A-General, 107 (1993) 1.

73. R. W. Powell, R. P. Tye, M. J. Hickman, International Journal of Heat Mass Tranfer, 8 (1965) 679.

74. N. M. Tikekar, T. J. Armstrong, A. V. Virkar, Journal of the Electrochemical Society, 153 (2006) A654.

75. A. Hauch, S. H. Jensen, J. B. Bilde-Sorensen, M. Mogensen, Journal of the Electrochemical Society, 154 (2007) A619.

76. F. W. Poulsen, Solid State Ionics, 129 (2000) 145.

77. B. J. Inkson, M. Mulvihill, G. Mobus, Scripta Materialia, 45 (2001) 753.

78. L. Holzer, F. Indutnyi, P. H. Gasser, B. Munch, M. Wegmann, Journal of Microscopy-Oxford, 216 (2004) 84.

79. L. Holzer, B. Muench, M. Wegmann, P. Gasser, R. J. Flatt, Journal of the American Ceramic Society, 89 (2006) 2577.